Gravitational Waves Data Analysis Overview for Core Collapse Supernovae

Michele Zanolin

First IGWN workshop on Core Collapse Supernovae Gravitational Wave theory and detection, July 22nd 2025

Warsaw

Outline

- Multi-messengers: Disclaimer while multi-messenger observation of a (hopefully galactic) CCSN will enable a vast range of studies, in this presentation I focus on the aspects that are currently directly used in the search and characterization of the GW signatures.
- Detector Response: Geometry, antenna patterns, noise statistical characterization.
- Detection Overview: maximum likelihood, network formulation, gaussian vs non-Gaussian noise. Frequentist vs. Bayesian. Single event vs population….
- Parameter Estimation: Deterministic features. Astrophysical interpretations
- Model Selection: slowly vs rapidly rotating progenitors.

Multimessengers: Neutrinos

- Capability to provide the best timing information (timing accuracy shorter than expected GW duration)
- Poor angular resolution (could still be used)
- Unambiguous Core Collapse Supernova neutrino triggers have not been available since SN1987a
- SuperNova Early Warning System (SNEWs) in place globally
- In a joint GW neutrino search the False alarm rate of a candidate event is the product of the FAR in GW and Neutrinos separately (See Marco Drago, and Matteo Bolleli presentations)
- See Zidu Lin talk for GW plus neutrino SASI meter.

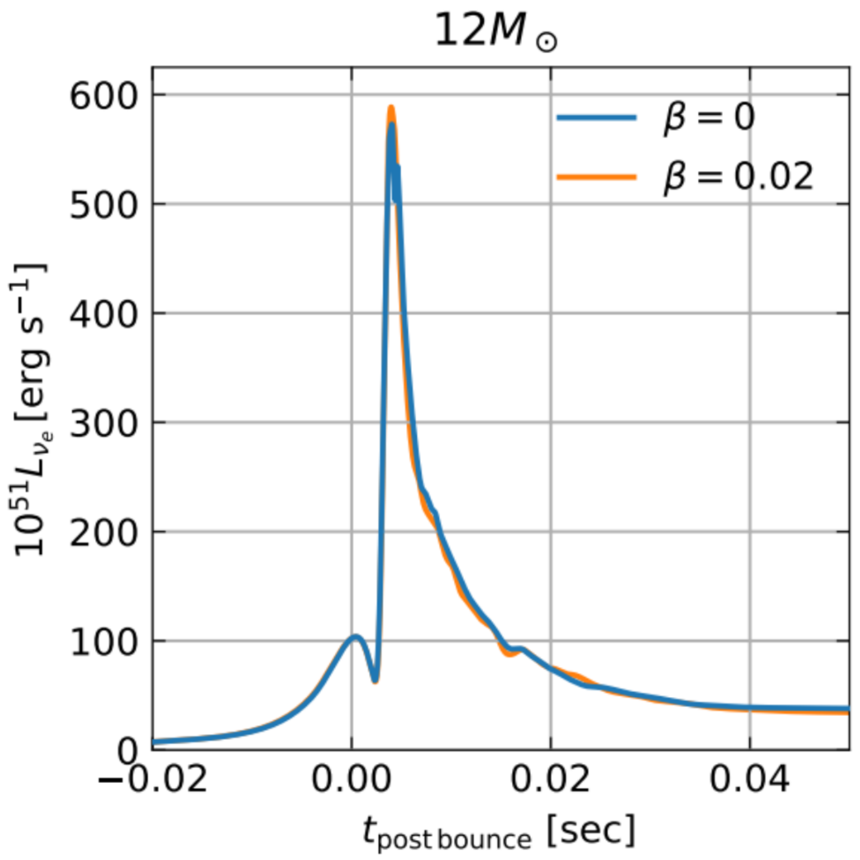

[Villegas, L. O., C. Moreno, M. A. Pajkos, M. Zanolin, and J. M. Antelis (2025), Class. Quant. Grav. 42 (11), 115001, arXiv:2304.01267 [gr-qc]]

Multimessengers: EM Observations

- Electromagnetic Observatories
  - Provide the best constraints on the source direction (angular resolution, sub-square degree, much better than the expected GW angular resolution)
  - Timing information for GW emission order of days.
  - Progenitor mass and distance estimation very useful. (see Rosa Poggiani and Chris Freyer presentations).

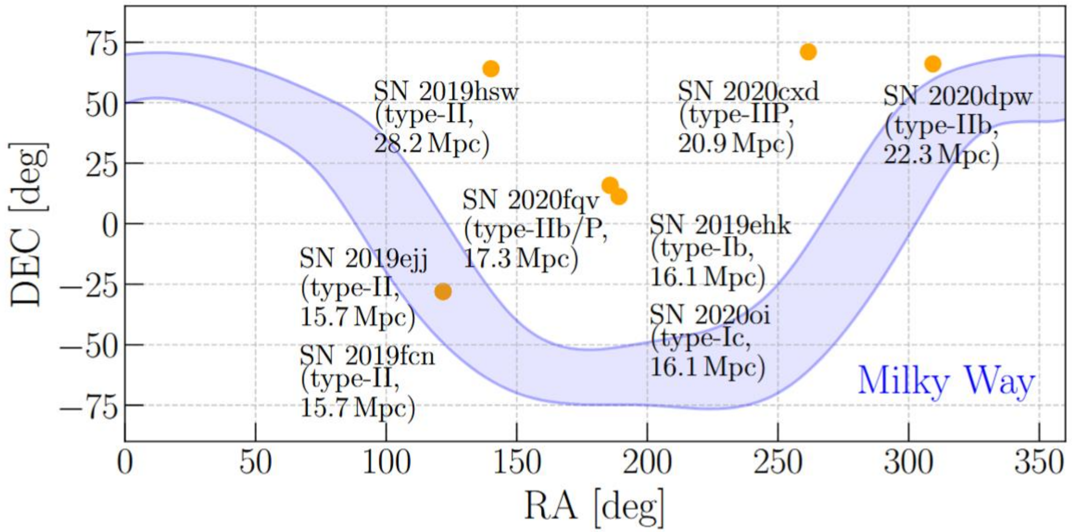

[Phys. Rev. D **110**, 042007]

SN2023ixf

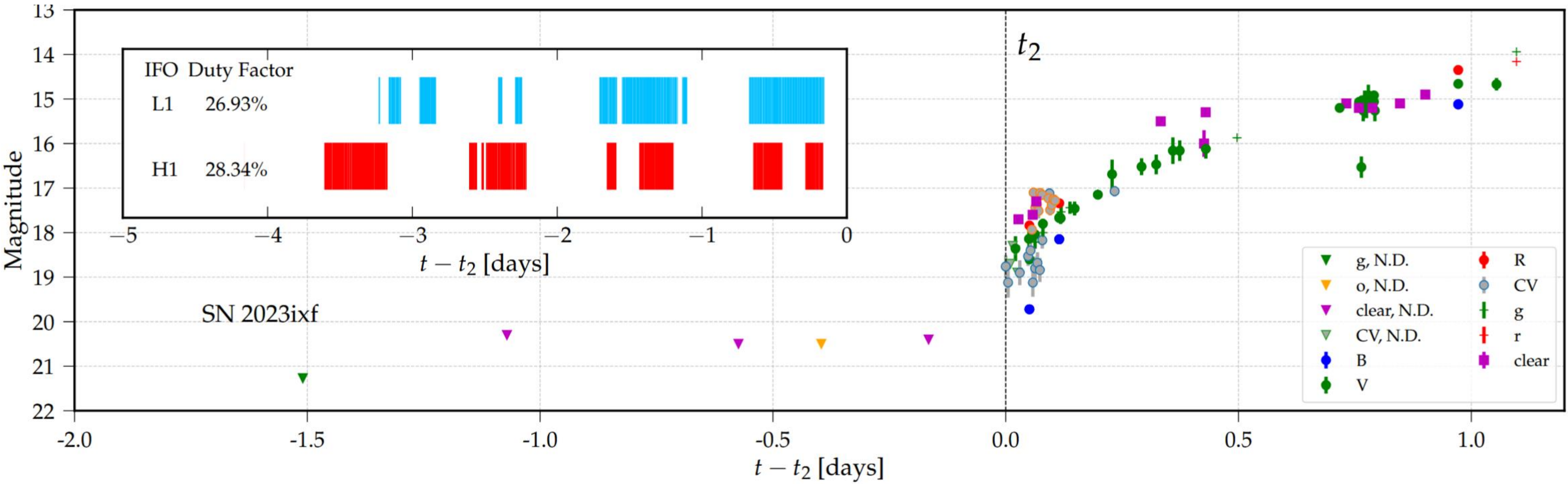

A. G. Abac et al 2025 ApJ 985 183

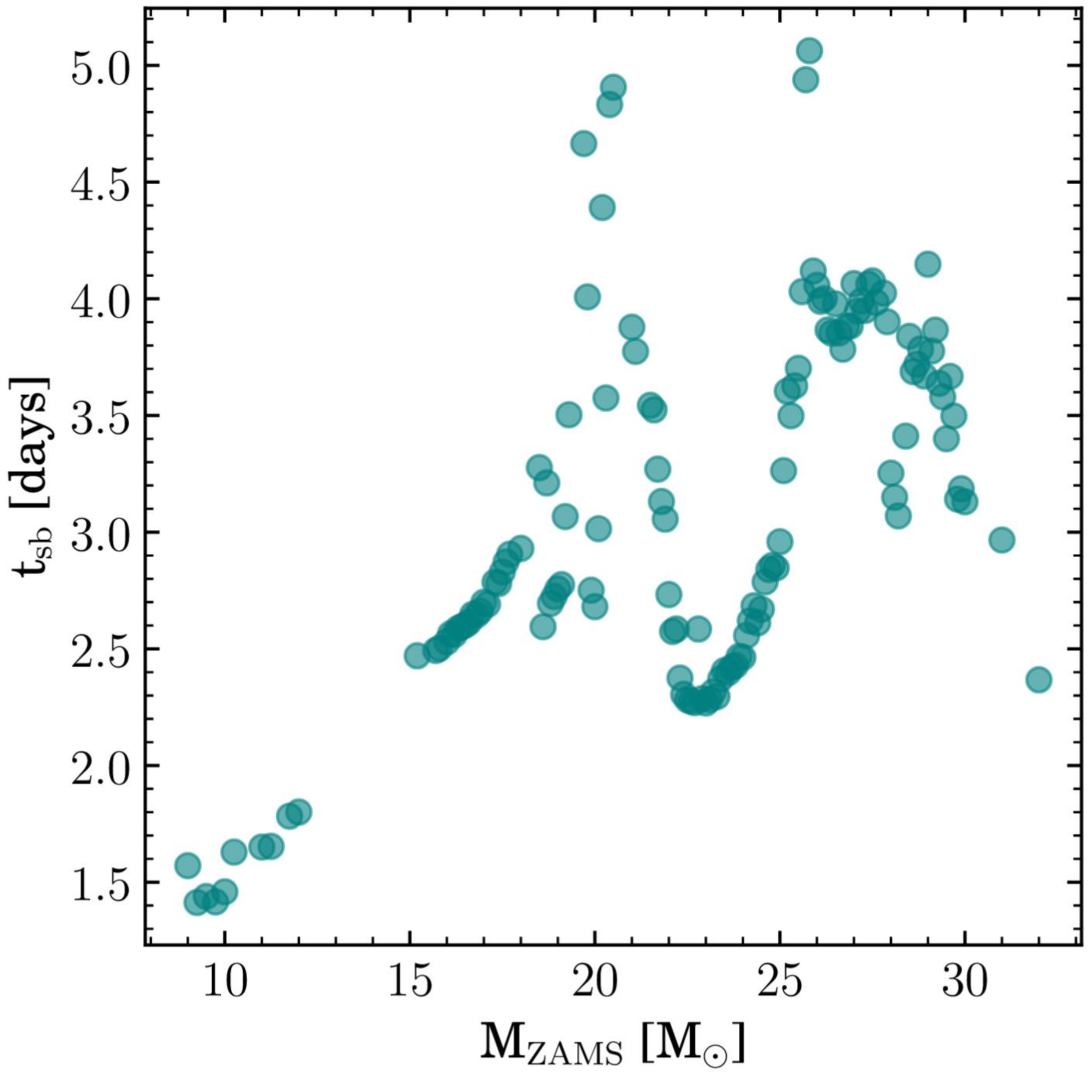

Time for shock breakout for the STIR + SNEC models.

Brandon L. Barker et al 2022 ApJ 934 67

Current Difficulties in the Progenitor Mass Estimation

- To illustrate the current difficulties in the progenitor mass estimation, we use the case of SN2023ixf: Pledger and Shara (2023) suggested that the progenitor mass was $8 - 10\ M_\odot$, Kilpatrick et al. (2023) predicted the mass to be $11\ M_\odot$, and Soraisam et al. (2023) instead predicted the mass to be $20 \pm 4\ M_\odot$

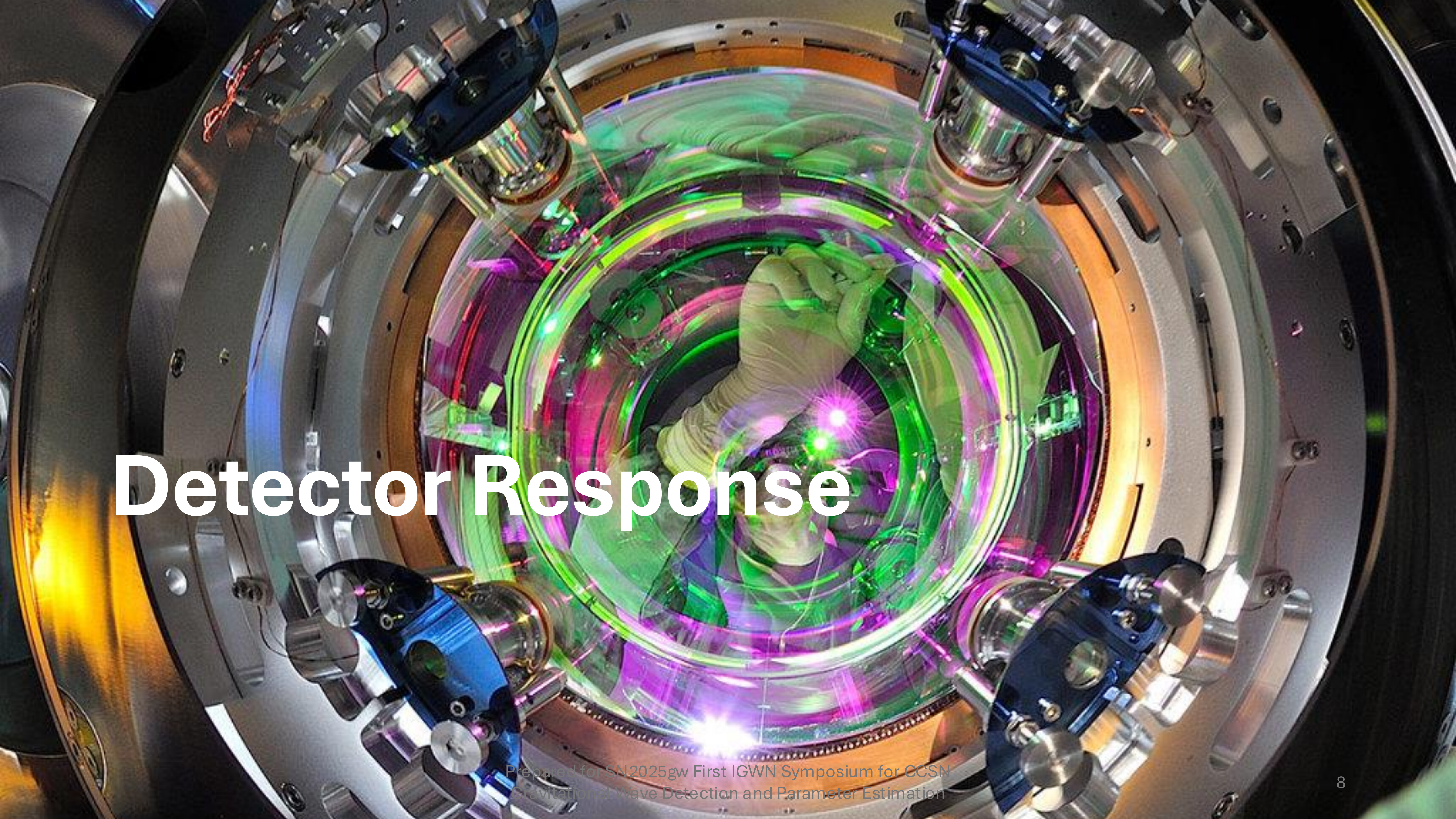

Detector Response

Detector Response

$$x_i(t) = h_i(t) + n_i(t), \quad (3)$$

$$\begin{aligned} h_i(t) &= H_{i+}(\theta,\phi,\psi)h_+(t-\tau_i) \\ &+ H_{i\times}(\theta,\phi,\psi)h_\times(t-\tau_i), \end{aligned} \quad (4)$$

$$\begin{aligned} H_{i\times}(\theta,\phi,\psi) &= -\frac{1}{2}(1+\cos^2(\theta))\cos 2\phi \cos 2\psi \\ &+ \cos\theta \sin 2\phi \cos 2\psi, \end{aligned} \quad (6)$$

$$\begin{aligned} H_{i+}(\theta,\phi,\psi) &= \frac{1}{2}(1+\cos^2(\theta))\cos 2\phi \cos 2\psi \\ &+ \cos\theta \sin 2\phi \sin 2\psi, \end{aligned} \quad (5)$$

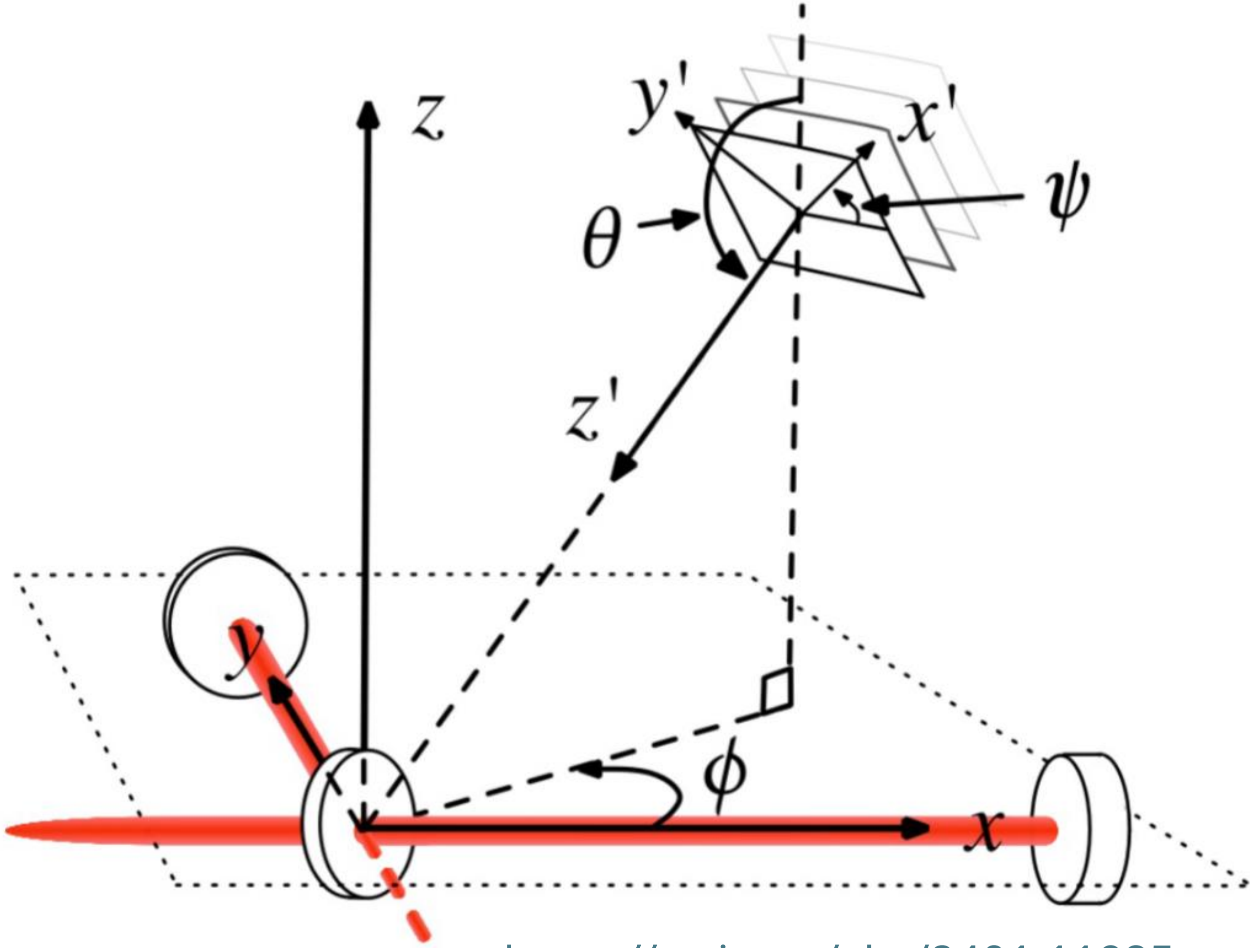

https://arxiv.org/abs/2401.11635

https://arxiv.org/abs/2401.11635

Polarization state.

- The two polarizations transform for a different ϕ with rotational metrices (with a period equal to π).
- If there is a psi where $h_x = 0$ it is said linearly polarized GW signal. (good approximation for the memory component).
- If the two polarizations are phase shifted by π/2 (possibly relevant for SASI) they are called elliptically polarized.
- Need to reconstruct both polarizations to establish if a specific polarization state is present (the capability to do so depends on both network properties and noise properties – hard for the L-H network, better for ET).

Noise Spectral Density

See Marie Anne Bizouard talk for future hardware

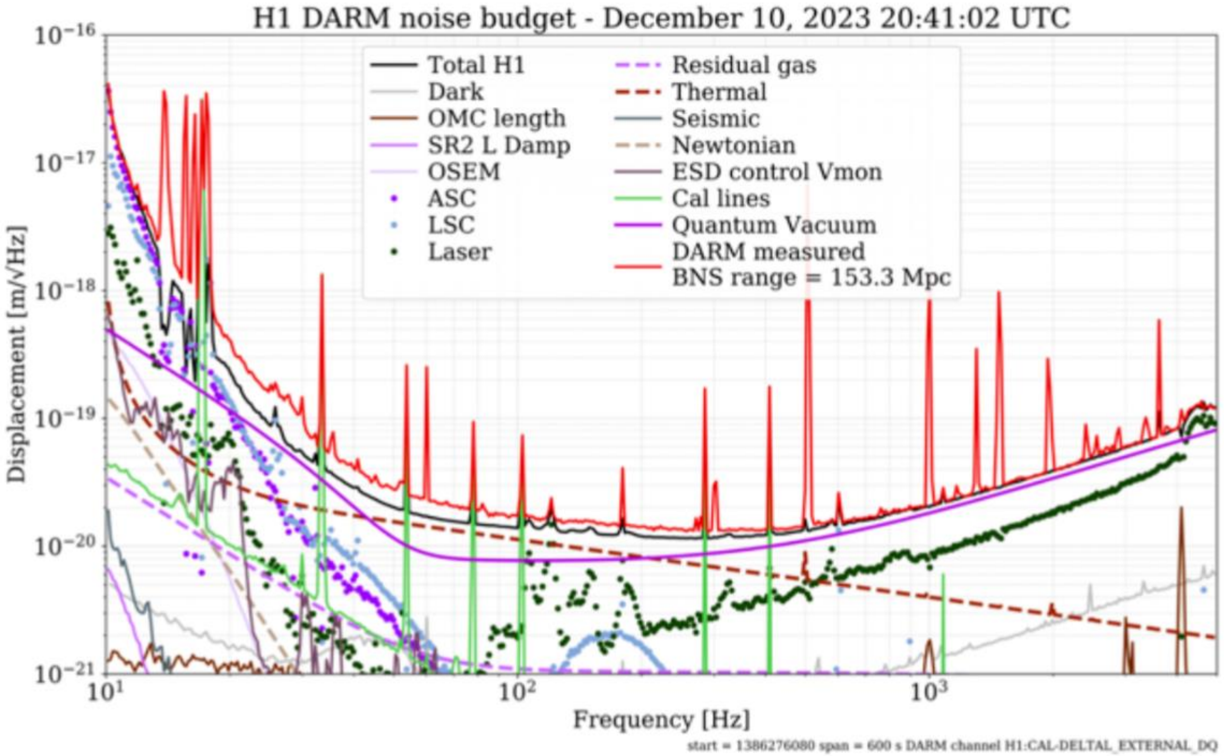

https://cosmicexplorer.org/sensitivity.html

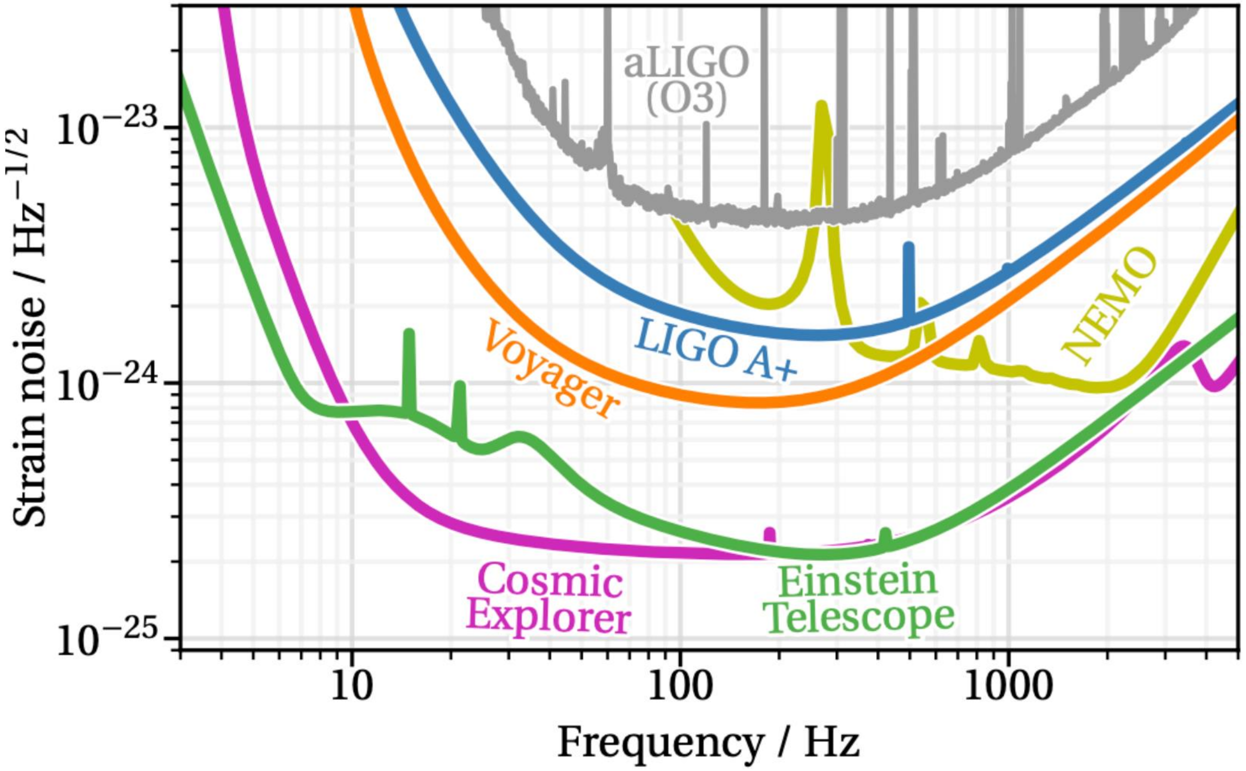

arXiv:2401.11635

$$R(t_1 - t_2) = \langle n_i(t_1) n_i(t_2) \rangle, \qquad (13)$$

$$\langle \tilde{n}^*_\alpha[k] \tilde{n}_\beta[k'] \rangle = \frac{N}{2} \delta_{\alpha\beta} \delta_{kk'} S_\alpha[k] \,, \qquad (2.4)$$

Patrick J Sutton *et al* 2010 *New J. Phys.* **12** 053034

Tilt-to-Length Coupling

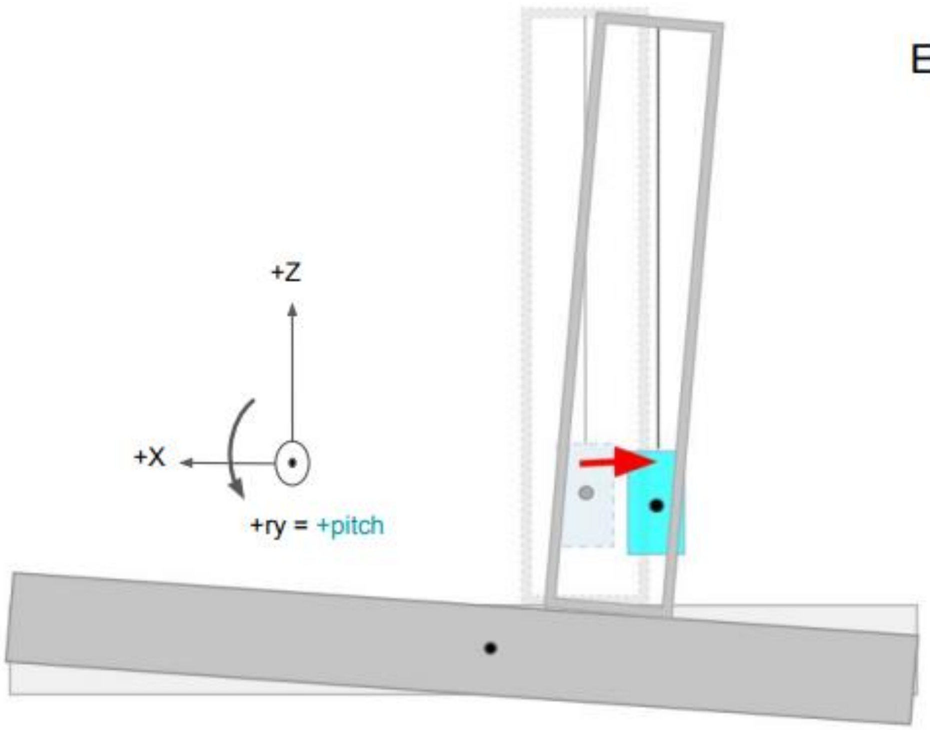

Example PR2 on HAM3

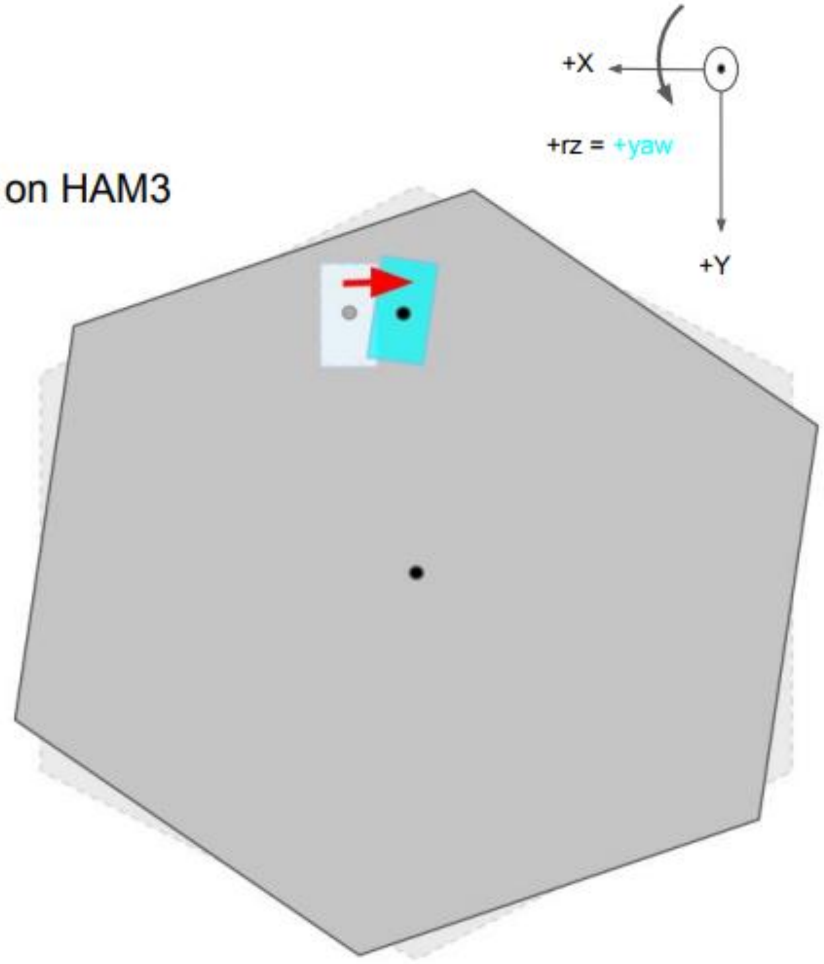

HAM: Horizontal Access Module (Vacuum Chamber)

Seismic Platform Interferometer (SPI) Pathfinder Update (LVK March 2025)

Joshua Freed, Jeff Kissel, Sina Koehlenbeck, Brian Lantz, Bram Slagmolen, Arnaud Pele, Eddie Sanchez, Jason Oberling, Matthew Heintze, Calum Torrie, Gabriele Vajente, Peter Fritschel, Michele Zanolin, …

The First Step: SPI Pathfinder (Install Target Oct 2025)

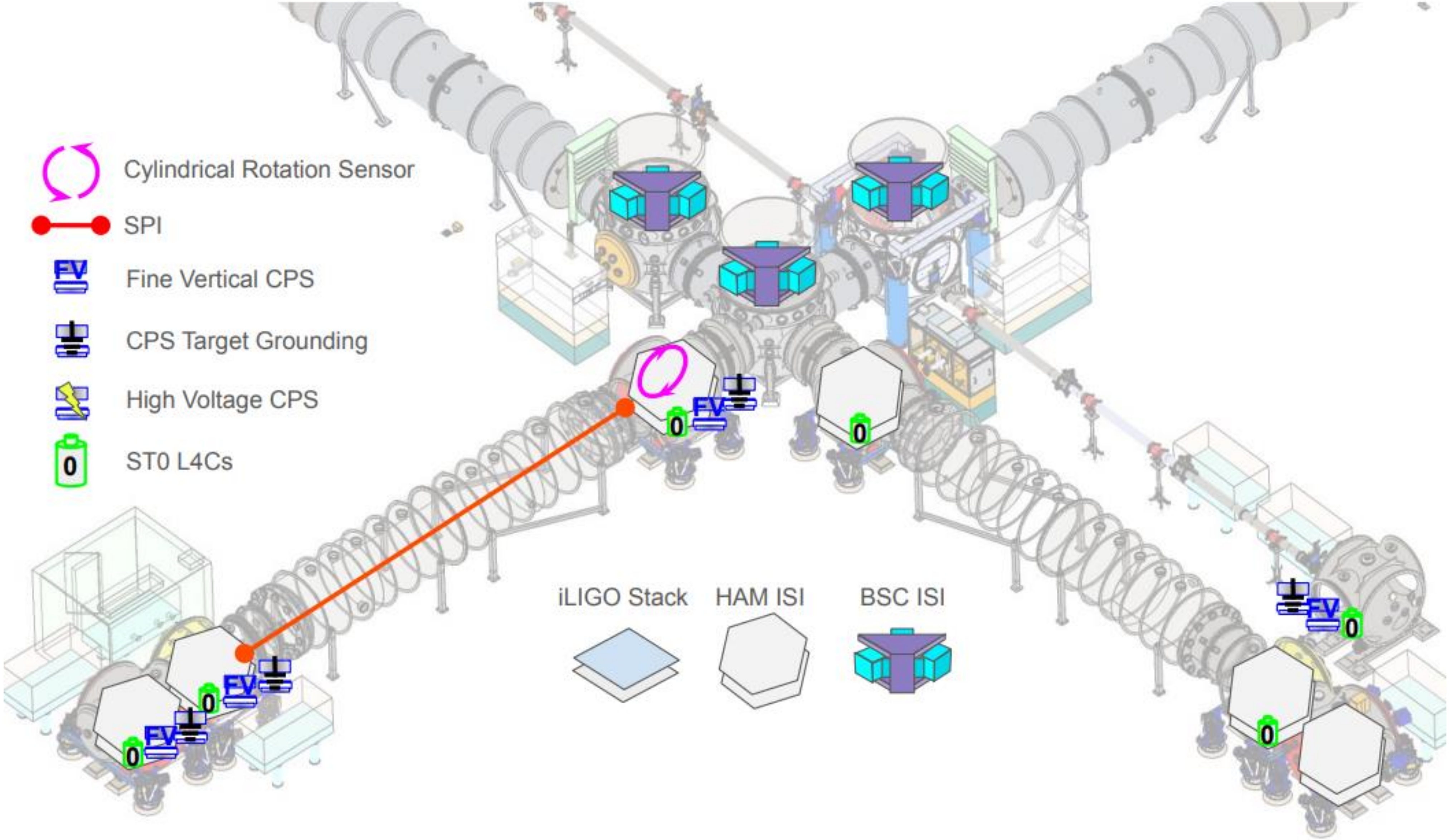

FINAL Optical Layout (Conceptually)

We have a final design doc! [T2400145]

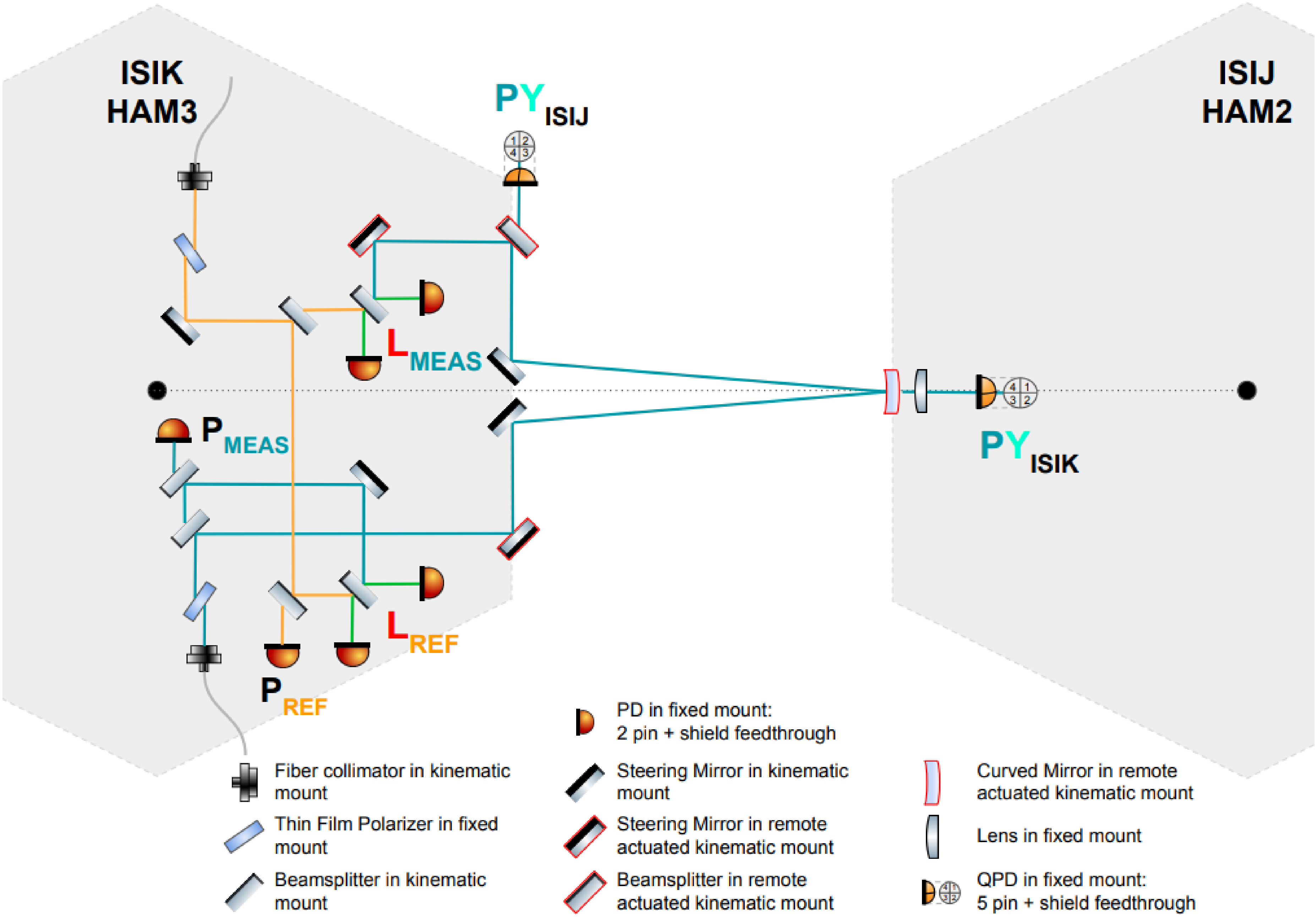

Low frequency: controls noise (correlated)
Middle frequency: coating thermal noise (uncorrelated)
High frequency: Poisson shot noise (uncorrelated)

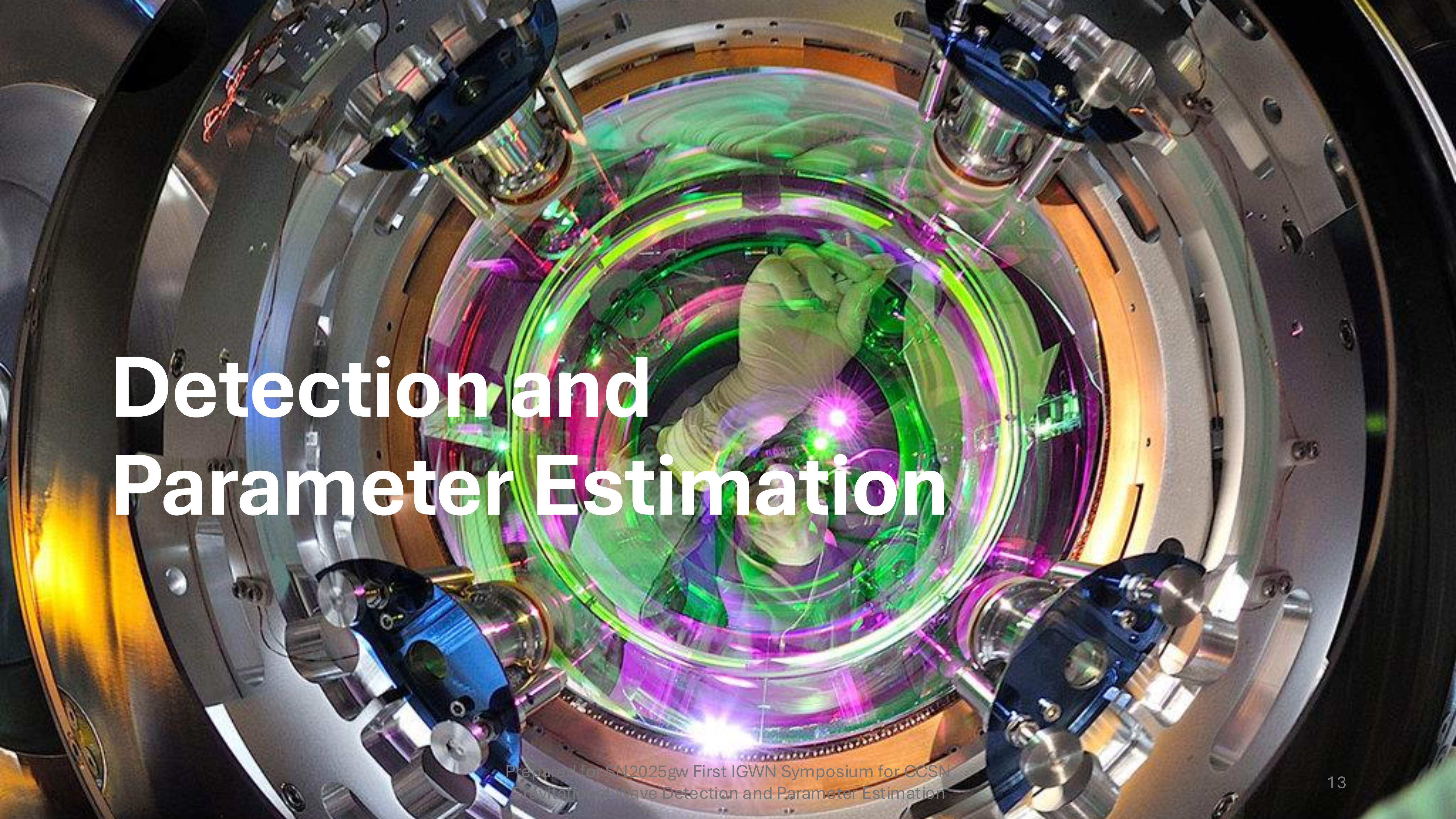

Detection and Parameter Estimation

We have two types of searches aiming to detecting CCSNe

- Targeted Search: Search for GWs from CCSNe in the presence of an EM and/or neutrino signature.
- All Sky Search: Part of the general LVK all-sky short-burst GW, where it is of the highest priority. Aimed at GWs from CCSNe or failed CCSNe that do not have neutrino triggers or an electromagnetic counterpart (because of extinction along the line of sight or because of the failure to generate an electromagnetic counterpart) or poorly sampled EM light curve.

Is there a scenario where we know what is the best detection approach, the best parameter estimation approach and the relationship between the two?:

Likelihood Ratio formulation in single detector white gaussian noise with known wave form

$$\Lambda = \frac{p(x(t); h(t, \xi))}{p(x(t))}\,, \qquad (7)$$

$$p(x) = N e^{-\frac{1}{2\sigma^2}\int_{-\infty}^{\infty}(x(t)-h(t-\tau;\theta))^2 dt}. \qquad (8)$$

https://arxiv.org/abs/2401.11635

$$L = -\frac{1}{2\sigma^2}\int_{-\infty}^{\infty}(h(t-\tau;\theta)^2 + x(t)h(t-\tau;\theta))dt, \quad (9)$$

If we focus only on the data dependent term of L the log likelihood of P

$$L(\tau,\theta) = -\frac{1}{2\sigma^2}\int_{-\infty}^{\infty} x(t)h(t-\tau;\theta))dt. \quad (10)$$

Neymann-Pearson lemma implies that the maximum value of L over **T** and **Θ** provides the best detection statistics and the best estimate of the parameters.

Limited applicability to CCSNe beside the core bounce of RR progenitors and the memory component (talks by Claudia Moreno, Emmanuel Avila and Colter Richardson).

https://arxiv.org/abs/2401.11635

Real data contains non-Gaussian components, we have networks of interferometers, and CCSNe signals are weakly modelled, the pool of signals might not cover completely the possible range of signals.

No theorem for optimality but the likelihood method is still the starting point for many pipelines used for CCSNe. We also started recently a more systematic effort to combine different pipelines.

Examples of Pipelines using likelihood ratios

- cWB
  - Klimenko, S., S. Mohanty, M. Rakhmanov, and G. Mit- selmakher (2005), Phys. Rev. D 72 (12), 10.1103/phys- revd.72.122002.
  - Mukherjee, S., G. Nurbek, and O. Valdez (2021), Phys. Rev.D 103, 103008.
- BayesWave
  - Cornish, N. J., T. B. Littenberg, B. Bécsy, K. Chatziioannou, J. A. Clark, S. Ghonge, and M. Millhouse (2021), Phys. Rev. D 103 (4), 044006, arXiv:2011.09494 [gr-qc].
- Spectrogram-based TFClusters
  - Sylvestre, J. (2003), Phys. Rev. D 68, 102005, arXiv:gr-qc/0308062.
- Q-Pipeline
  - Chatterji, S., L. Blackburn, G. Martin, and E. Katsavounidis (2004), Class.Quant.Grav. 21, S1809, arXiv:0412119 [gr-qc].
- X-Pipeline
  - Sutton, P. J., et al. (2010), New J. Phys. 12, 053034, arXiv:0908.3665 [gr-qc].

Likelihood Ratio: Network of Interferometers

$$\Lambda = \frac{\Pi_{i=1}^{K} p_i(x_i(t); h_i(t,\xi))}{\Pi_{i=1}^{K} p_i(x_i(t))} \tag{11}$$

$$p(x;h) = Me^{-\int_{-\infty}^{+\infty}(x(t_1)-h(t_1))R(t_1-t_2)(x(t_2)-h(t_2))dt_1 dt_2}, \tag{12}$$

$$\tilde{x}(m) = \sum_{l=0}^{N-1} e^{-\frac{2\pi l m}{N}} x(t_l) \equiv \sum_{l=0}^{N-1} F_{ml} x(t_l), \tag{14}$$

$$p(\tilde{x};h) = \tilde{M} e^{-(\tilde{x}-\tilde{h})^{\dagger} C (\tilde{x}-\tilde{h})}, \tag{15}$$

$$L = \frac{1}{2} \sum_{i=1}^{K} -(\tilde{x}_i - \tilde{h}_i)^{\dagger} C^i (\tilde{x}_i - \tilde{h}_i), \tag{16}$$

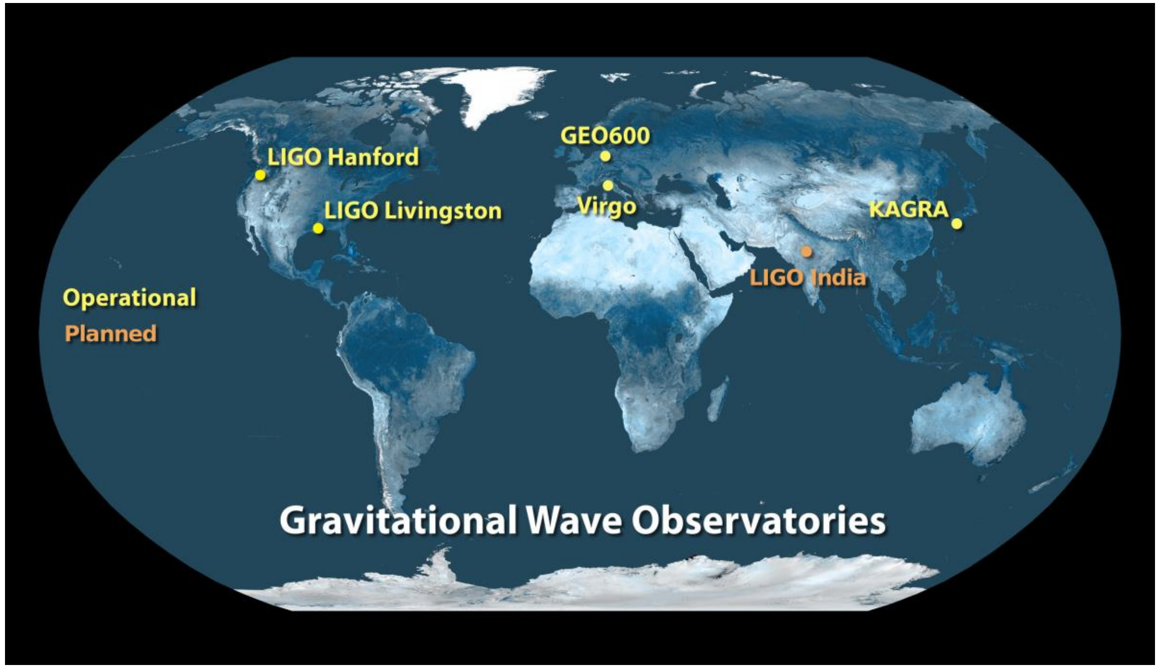

Caltech/MIT/LIGO Lab

https://arxiv.org/abs/2401.11635

Maximum Likelihood Detection and Waveform Reconstruction (see the ref below for a list of all revevant references of the implementation)

See Sergey Klimenko talk
25/07 12:00

$$0 = \frac{\delta L}{\delta h}|_{h=h_{\text{stationary}}}. \tag{17}$$

$$(\tilde{d}(l))^T = (\frac{\tilde{x}_1(l)}{\sqrt{C^1_{ll}}}, \ldots, \frac{\tilde{x}_K(l)}{\sqrt{C^K_{ll}}}). \tag{18}$$

$$\tilde{h}_{\text{stationary}} = (\tilde{H}\tilde{H}^T)^{-1}\tilde{H}\tilde{d}, \tag{19}$$

$$\tilde{H}_+ = (\frac{H_{1+}}{\sqrt{C^1_{ll}}}, .., \frac{H_{K+}}{\sqrt{C^K_{ll}}}), \tag{20}$$

$$\tilde{H}_\times = (\frac{H_{1\times}}{\sqrt{C^1_{ll}}}, .., \frac{H_{K\times}}{\sqrt{C^K_{ll}}}), \tag{21}$$

https://arxiv.org/abs/2401.11635

Maximum Likelihood Detection and Waveform Reconstruction. For large SNR equation (25) approximate the sum of (26) at different interferometers

See Sergey Klimenko talk
25/07 12:00

$$\tilde{H} = \begin{bmatrix} \tilde{H}_+ \\ \tilde{H}_\times \end{bmatrix}, \tag{22}$$

$$\tilde{H}'_+ = \cos\gamma \tilde{H}_+ + \sin\gamma \tilde{H}_\times \tag{23}$$

$$\tilde{H}'_\times = -\sin\gamma \tilde{H}_+ + \cos\gamma \tilde{H}_\times \tag{24}$$

For the value of gamma in the dominant polarization frame where the two projectors below operate on perpendicular directions

$$L = \sum_l \left[\frac{(H'_+ \tilde{d})_l^2}{|H'_+|_l^2} + \frac{(H'_\times \tilde{d})_l^2}{|H'_\times|_l^2} \right] \tag{25}$$

$$\mathrm{SNR_{MF}} = \sqrt{\int_{-\infty}^{+\infty} \frac{\tilde{h}(f)^2}{\tilde{n}(f)^2} df}, \tag{26}$$

https://arxiv.org/abs/2401.11635

Customizations

Whitening / Linear Prediction Filter

[Patrick J Sutton et al 2010 New J. Phys. 12 053034]

- In frequency domain the covariance matrix become diagonal Eigen values are the inverse of the noise spectral amplitude
- Makes noise covariance matrix proportional to identity in frequency domain.

- Linear prediction can be used to remove predictable components of the noise like frequency lines (see Colter Richardson presentation for the application to memory)

$$x_{i,\text{predicted}}(t_n) = \sum_{l=1}^{P} a_l x_i(t_{n-l}),$$

$$d(t_n) = x_i(t_n) - x_{i,\text{predicted}}(t_n). \qquad (28)$$

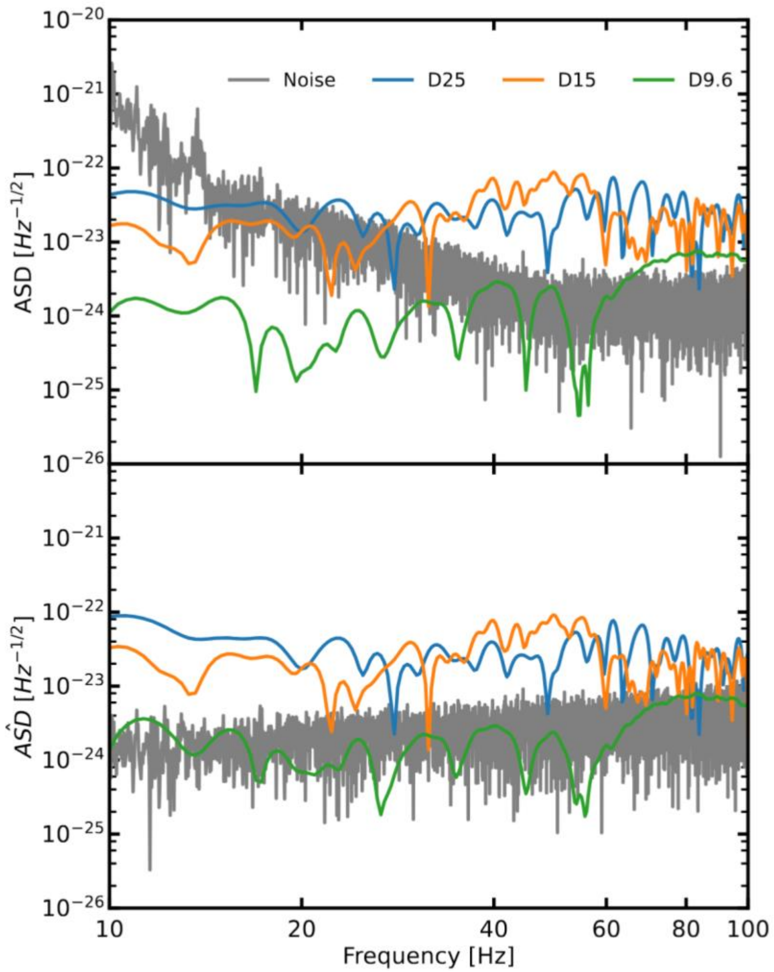

Wavelet Decomposition and Clustering to produce events and remove non gaussian components of the noise.

See Sergey Klimenko talk 25/07 12:00

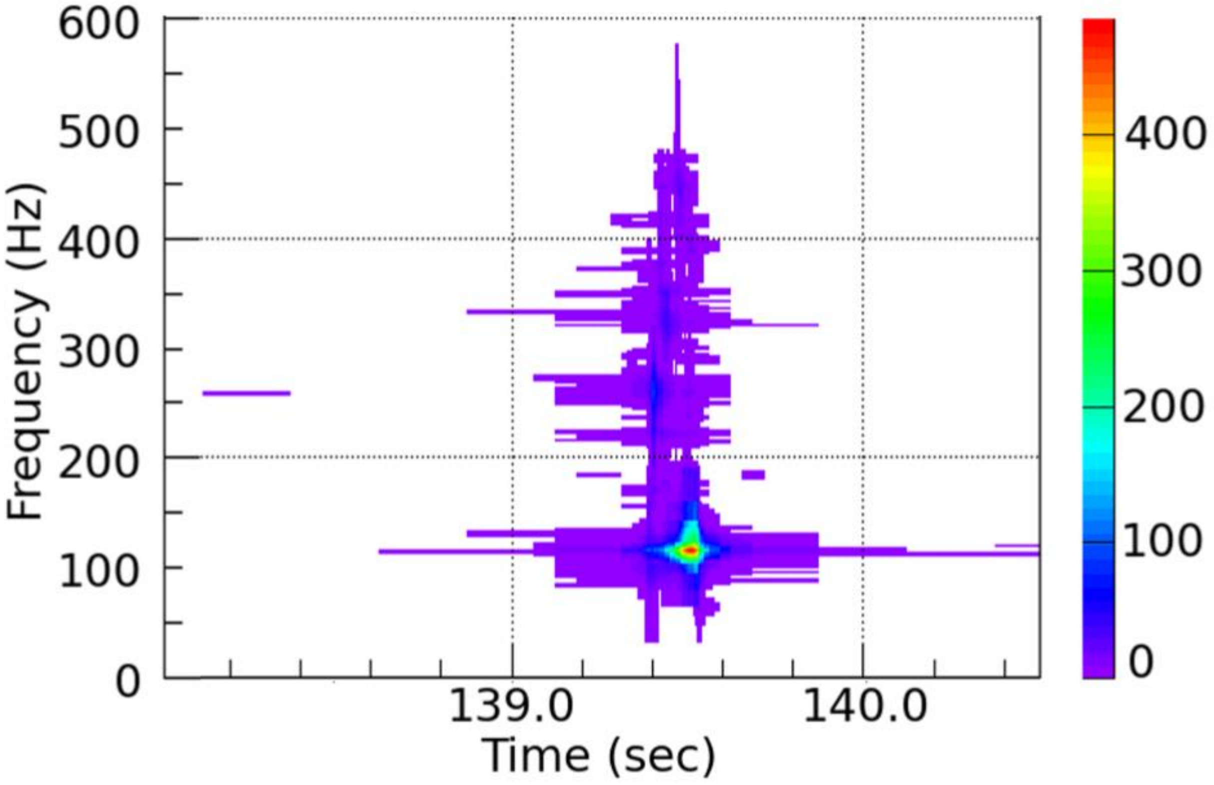

Network Constraints

- Having the reconstructed arrival time at different interferometers differ by less than or equal to the maximum possible travel time between the detectors. Likelihood ratio may be automatically applied in the pipeline.
- If an interferometer's network is mostly sensitive to a single polarization, we do not try to reconstruct the other polarization because it would produce mostly noise-induced event
- A network may have sky locations where it is particularly insensitive, and events reconstructed in these directions might also be mostly noise-induced events
- This consideration is also relevant if the source direction is used in the search algorithm itself by considering only GW candidates consistent with the CCSN sky location. Optical CCSN observations are expected to locate the SN direction within a few tenths of a degree, and the worst-case pointing accuracy with Superkamiokande (Tomas et al., 2003) is expected to be 8 square degrees with 95 percent confidence level.

Construction on Signal Time-Frequency Structure

- We assume that the frequency content is limited between ~20 Hz and ~2000 Hz, because the detectors are much less sensitive outside this frequency band.
    - With exception to the search for CCSN-generated memory.
- We also do not include events that are longer than a few seconds.
- In recent years it has proven useful to use different versions of ML algorithms to distinguish noise-induced events from events of astrophysical origin. (Antelis et al., 2022; Cavaglia et al., 2020; Lopez et al., 2022; Morales et al., 2021)
- It is possible that neutrino constraints could be used in addition to the GW's detection process to enhance detectability.

Veto and Data Quality

- For all algorithms devoted to detection and parameter estimation, it is critical to identify stretches of data with coupling to non-astrophysical disturbances at a level that would affect scientific conclusions. Currently there is no CCSN specialized approach to this.
- The noise can be divided into an ever-present Gaussian component, which emerges as a product of many small disturbances blending, as described by the central limit theorem, and glitches.
- Glitches are studied and classified on a continuous basis by different laser interferometer collaborations

Detection Procedure.

1. Add to the data of one or more interferometers a nonphysical time shift.

2. Calculate the total duration of the coincident data—i.e., the data from periods of time when all the interferometers were collecting data simultaneously.

3. Using the coincident data itself, identify events (e.g., via wavelet decomposition and clustering).

4. Compute L for each event.

5. Compute the cumulative number of events above a certain value of L.

6. Divide the result of (5) by the result of (2) to produce the FAR as a function of L.

Detection Procedure Continued

7. Multiply the result from (6) by the duration of the on source window to obtain the FAP.

8. Step (7) allows us to identify the needed threshold on L to obtain a desired value of the FAP (e.g., 5 sigma requires that the false alarm probability is smaller than 3.0 × 10−7).

9. To determine if an event is a detection, we consider whether the L of the event corresponds to a FAP that is small enough to satisfy the criteria for detection (e.g., 5 sigma).

10. To have sufficient statistics, we repeat step (1) many times (for many different time shifts) and merge the results.

Given the threshold of L for a desired FAP, we can then inject a GW into the data many times and determine the fraction of times we recover the GW. This is the detection efficiency. This allows us to find the following pairs of numbers: (false alarm probability, detection efficiency). The receiver operating curve is obtained by plotting these pairs, for a fixed waveform at a fixed distance. It is used in choosing which algorithms to use for detection purposes.

Events distributions

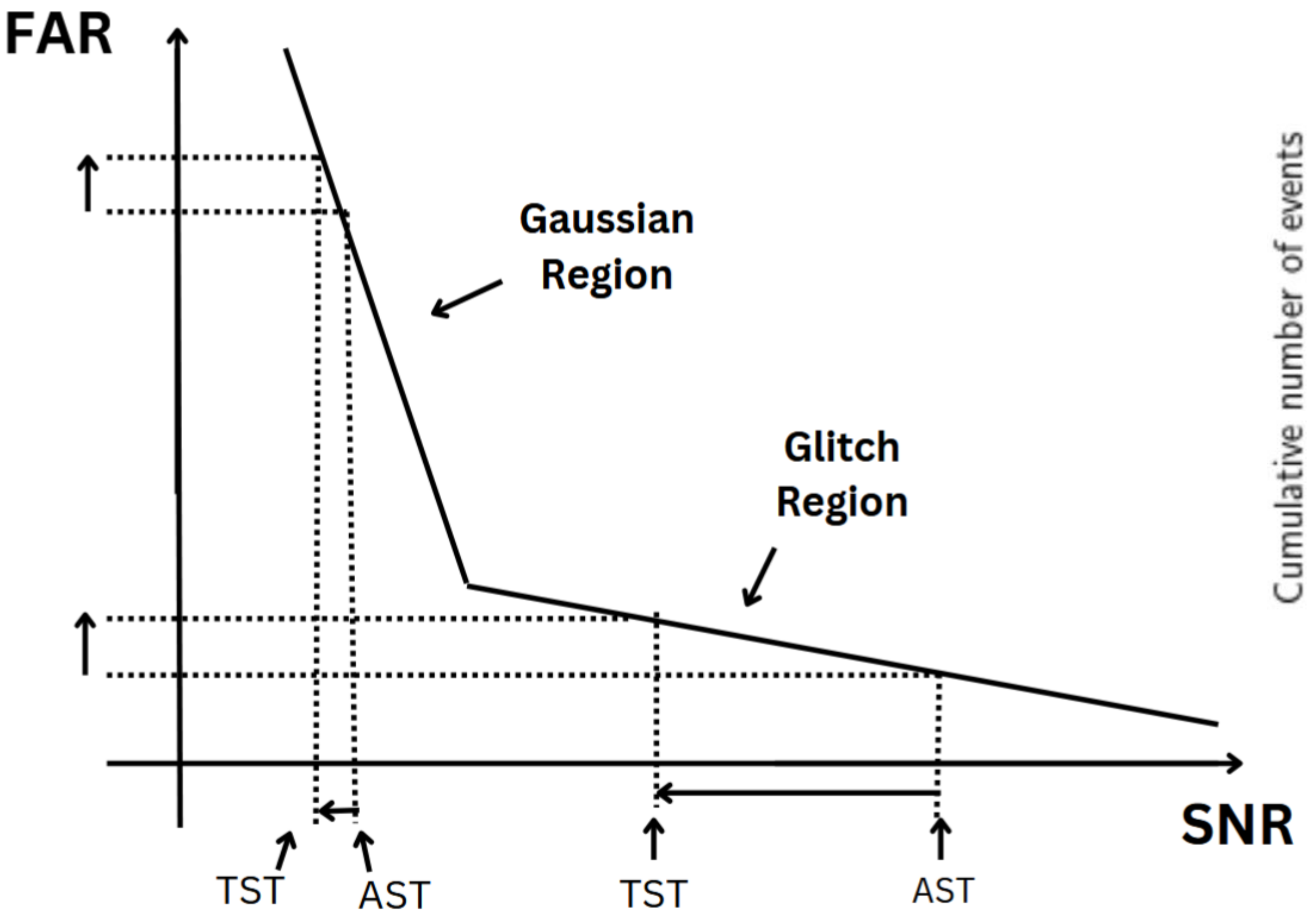

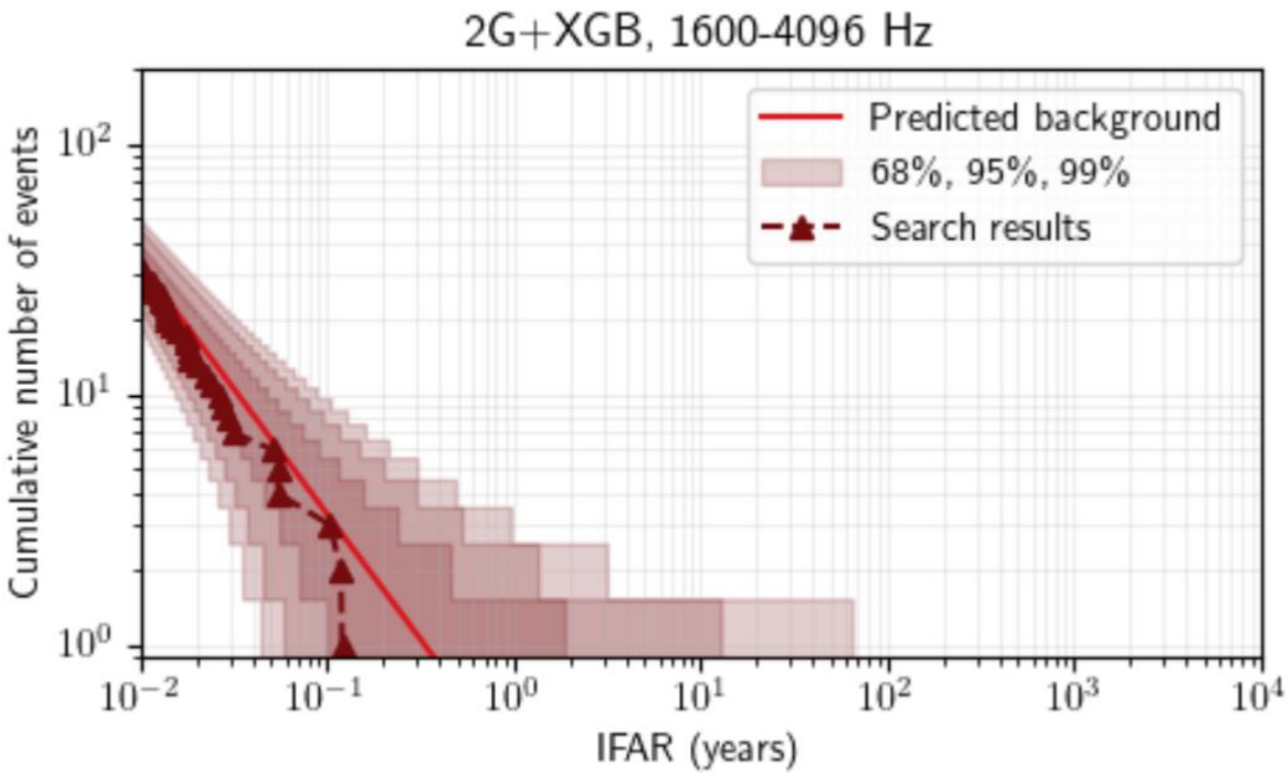

arXiv:2507.12374

arXiv:2401.11635

Requirement for detection

- For example, similar to the standards for early detections in particle physics (Lyons, 2013), in the first binary-black-hole detection a 5.1 sigma FAP was achieved (Abbott et al., 2016b).
- In the first binary neutron-star detection, the FAR was less than one false event in 8×10^8 years (if we have an observational window of approximately one week, as in the case of EM candidates, this would correspond to approximately a 5 sigma FAP, as well).
- The same FAP was not always attained in subsequent CBC detections, and the debate about what are the needed values for the first detection of GWs from CCSNe is still ongoing at the time of this writing, in part because of the expected rarity of such events and the likely presence of neutrino detection as well.

Bayesian Methods

$$p(x, h) = p(x; \theta)p(\theta), \qquad (29)$$

- The use of a frequentist versus a Bayesian approach has both practical and conceptual ramifications.
- In the frequentist approach, the probability distribution of the data depends on the physical values of the parameters, the latter of which are treated as deterministic quantities.
- In the Bayesian approach, the parameters are random variables, as well, and the priors incorporate informed opinions of those performing inference on the data, regarding the values of these parameters
- Bayesian methods can be used with a specific focus on CCSNe or for unmodeled detection and waveform reconstruction.
- We do not have experimental data to constrain the CCSNe priors. Sometimes it is argued that uniform priors (i.e., with a PDF that is constant over a certain range of values) can be used in the absence of prior knowledge.

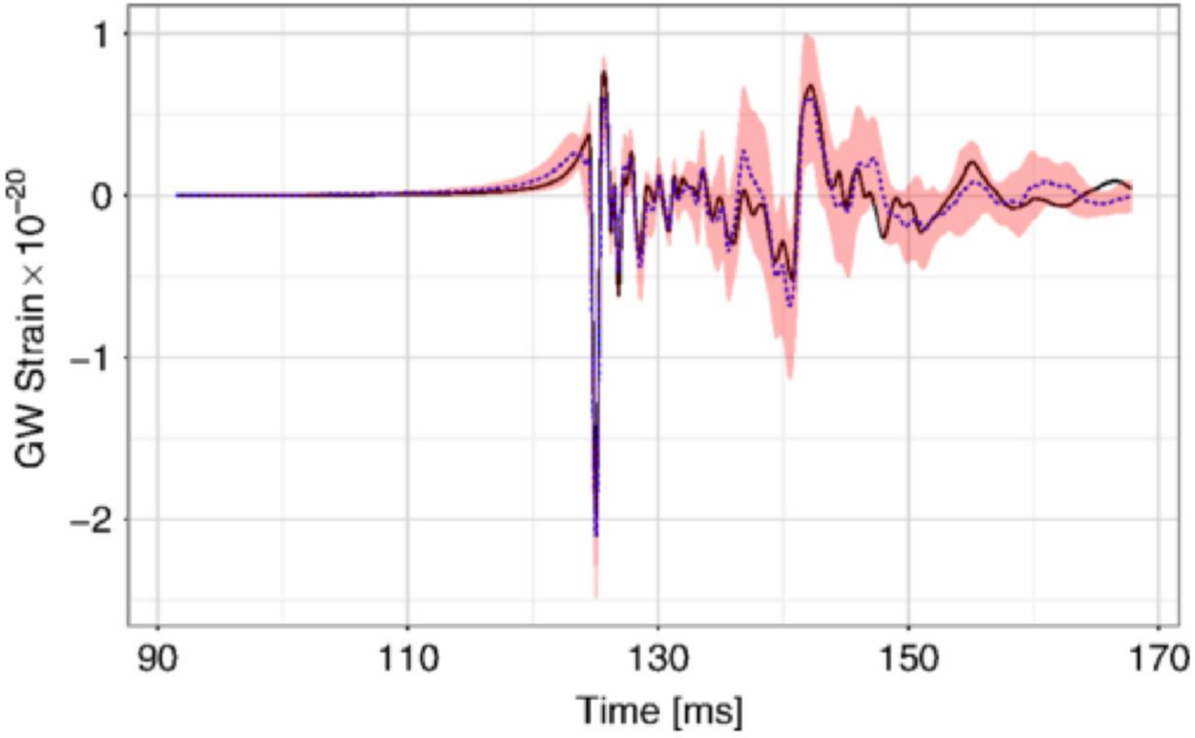

Cornish et al. (2021)

Bayesian vs. Frequentist Methods

- This approach can create problems. For example, a constant PDF in amplitude is not uniform in energy, which is proportional to the square of the amplitude, and vice versa [e.g., see Powell and Müller (2022), where amplitude and energy estimates are performed for CCSNe].
- It is also important to check the impact of priors on parameter estimates, as already noted in Chattopadhyay and Fairhust (2024). In some cases, priors also produced variances smaller than the error theoretical minimum, the Cramer–Rao lower bound [see the discussion in Tso and Zanolin (2016)].
- For unmodeled detection and waveform reconstruction, which is also of interest for CCSNe, Bayesian methods can be used in a modality where the priors are used to define the properties of the noise (Gupta and Cornish, 2024).
- In this case priors can be determined by experimental measurements. In this approach GWs are reconstructed as portions of the signal incompatible with the noise properties.
- This approach is currently employed by BayesWave. While we do not describe in detail the Bayesian implementation, Pannarale et al. (2019), Sutton et al. (2010), and Cornish et al. (2021), and references cited therein, provide a good overview of current efforts

Calibration Errors (Milan Wils talk)

$$C(f) = A(f)(1+\alpha(f)) * e^{\phi(f)(1+\beta(f))}, \qquad (30)$$

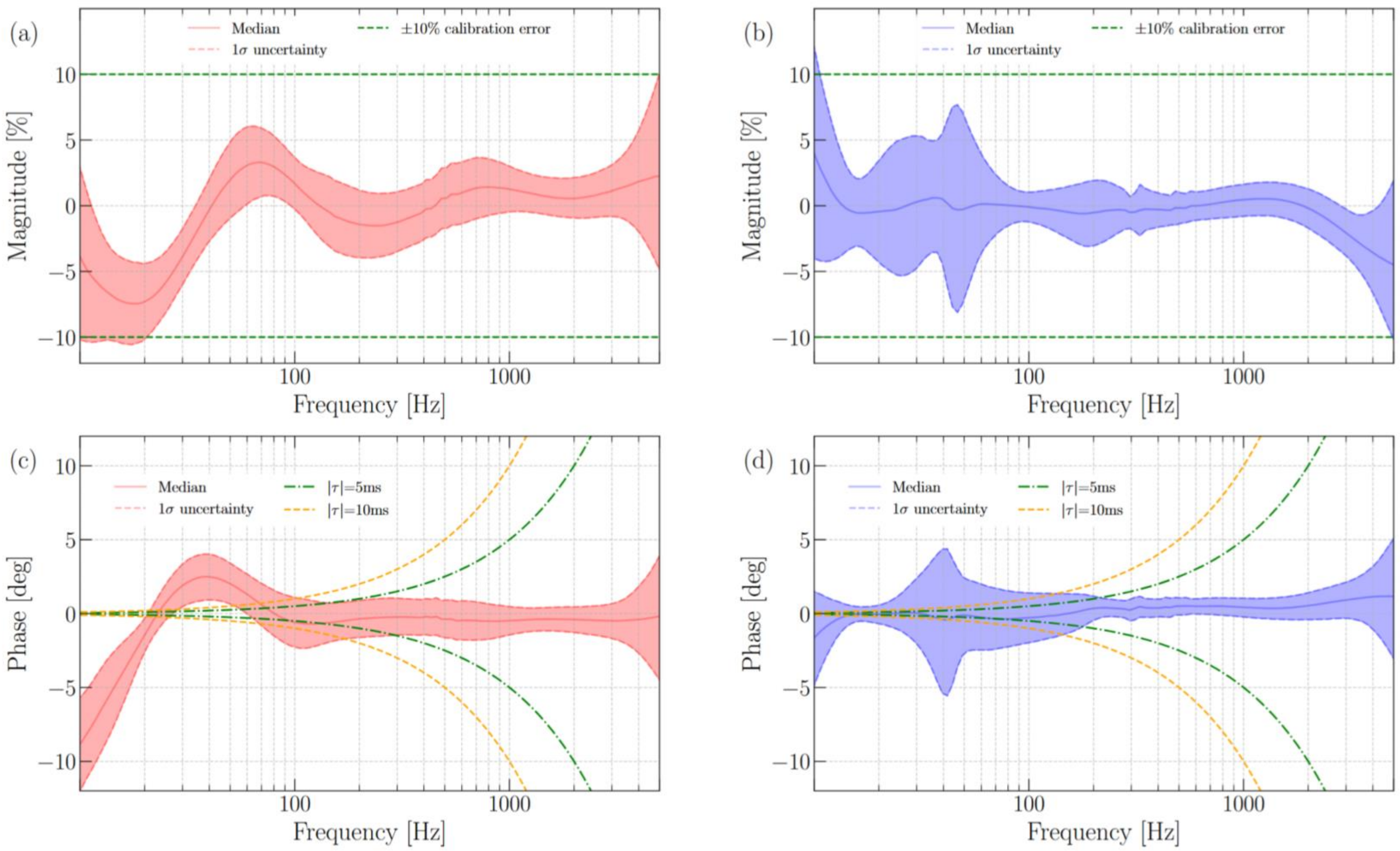

The physical frequency-dependent calibration errors for magnitude, panels (a) and (b), and phase, panels (c) and (d), for H1 and L1, respectively. These examples correspond to GPS times of the worst calibration errors during O3. The dashed lines in panels (a) and (b) show the amplitude calibration errors used in the previous all-sky search [143]. The dashed lines in panels (c) and (d) show the induced phase calibration errors when using a time jittering of 5 ms and 10 ms as indicated by the green and orange curves, respectively. When compared to the realistic calibration curves, these two methods yield estimates for the calibration errors that are non-representative of the magnitude or frequency evolution of possible physical calibration errors. The realistic calibration errors are found to be negligible with respect to the previously used ones.

https://journals.aps.org/prd/abstract/10.1103/PhysRevD.110.042007

PHYSICAL REVIEW D **110**, 042007 (2024)

Optically targeted search for gravitational waves emitted by core-collapse supernovae during the third observing run of Advanced LIGO and Advanced Virgo

Marek J. Szczepańczyk,[1,2,*] Yanyan Zheng,[3] Javier M. Antelis,[4,5] Michael Benjamin,[6] Marie-Anne Bizouard,[7] Alejandro Casallas-Lagos,[4,8] Pablo Cerdá-Durán,[9,10] Derek Davis,[11] Dorota Gondek-Rosińska,[12] Sergey Klimenko,[1] Claudia Moreno,[4,8] Martin Obergaulinger,[9] Jade Powell,[13,14] Dymetris Ramirez,[4] Brad Ratto,[4] Colter Richardson,[15] Abhinav Rijal,[4,16] Amber L. Stuver,[17] Paweł Szewczyk,[12] Gabriele Vedovato,[18,19] Michele Zanolin,[4] Imre Bartos,[1] Shubhagata Bhaumik,[1] Tomasz Bulik,[12] Marco Drago,[20] José A. Font,[9,10] Fabio De Colle,[21] Juan García-Bellido,[22] V. Gayathri,[23,1] Brennan Hughey,[24] Guenakh Mitselmakher,[1] Tanmaya Mishra,[1] Soma Mukherjee,[25] Quynh Lan Nguyen,[26] Man Leong Chan,[27] Irene Di Palma,[28,29] Brandon J. Piotrzkowski,[30] and Neha Singh[12]

We present the results from a search for gravitational-wave transients associated with core-collapse supernovae observed optically within 30 Mpc during the third observing run of Advanced LIGO and Advanced Virgo. No gravitational wave associated with a core-collapse supernova has been identified. We then report the detection efficiency for a variety of possible gravitational-wave emissions. For neutrino-driven explosions, the distance at which we reach 50% detection efficiency is up to 8.9 kpc, while more energetic magnetorotationally driven explosions are detectable at larger distances. The distance reaches for selected models of the black hole formation, and quantum chromodynamics phase transition are also provided. We then constrain the core-collapse supernova engine across a wide frequency range from 50 Hz to 2 kHz. The upper limits on gravitational-wave energy and luminosity emission are at low frequencies down to $10^{-4} M_{\odot} c^2$ and $6 \times 10^{-4} M_{\odot} c^2/\mathrm{s}$, respectively. The upper limits on the proto-neutron star ellipticity are down to 3 at high frequencies. Finally, by combining the results obtained with the data from the first and second observing runs of LIGO and Virgo, we improve the constraints of the parameter spaces of the extreme emission models. Specifically, the proto-neutron star ellipticities for the long-lasting bar mode model are down to 1 for long emission (1 s) at high frequency.

DOI: 10.1103/PhysRevD.110.042007

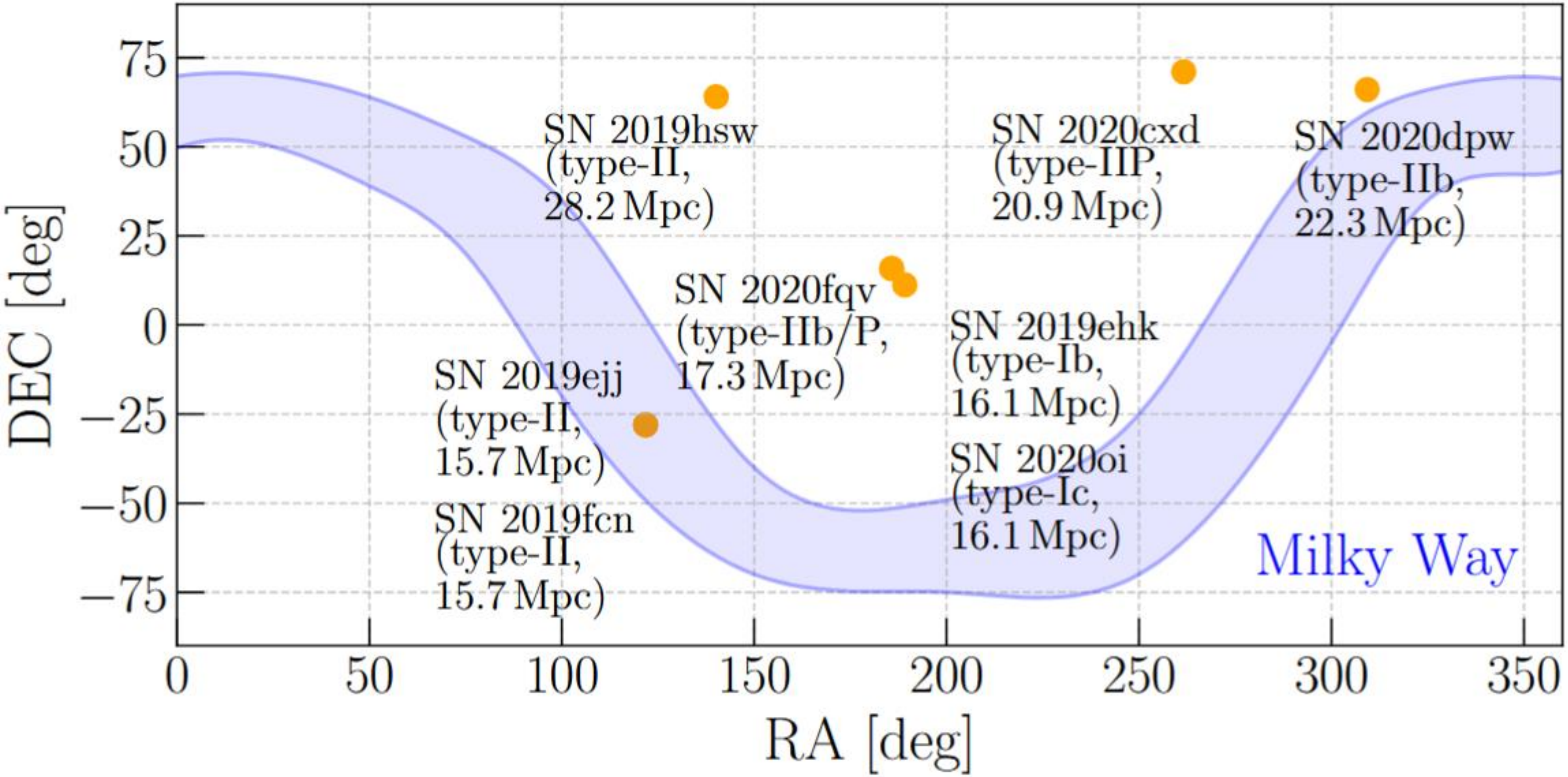

https://journals.aps.org/prd/abstract/10.1103/PhysRevD.110.042007

Light curve interpolations

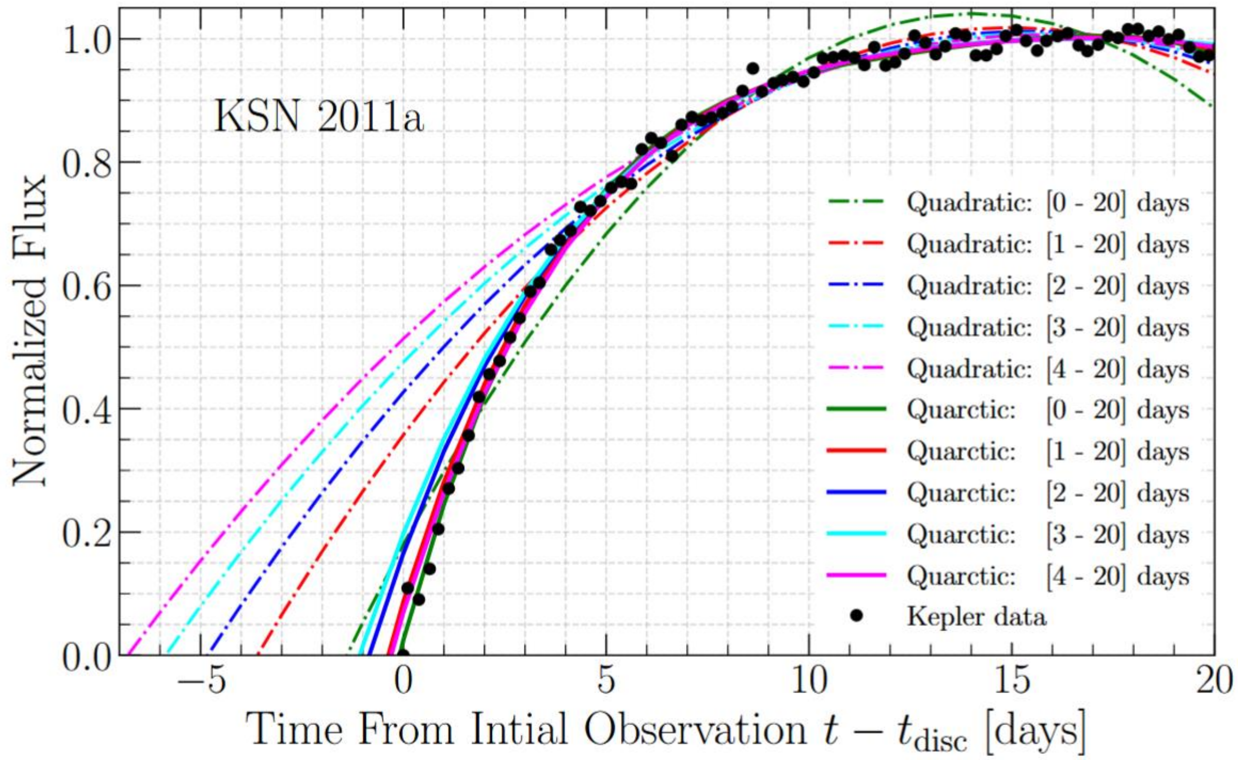

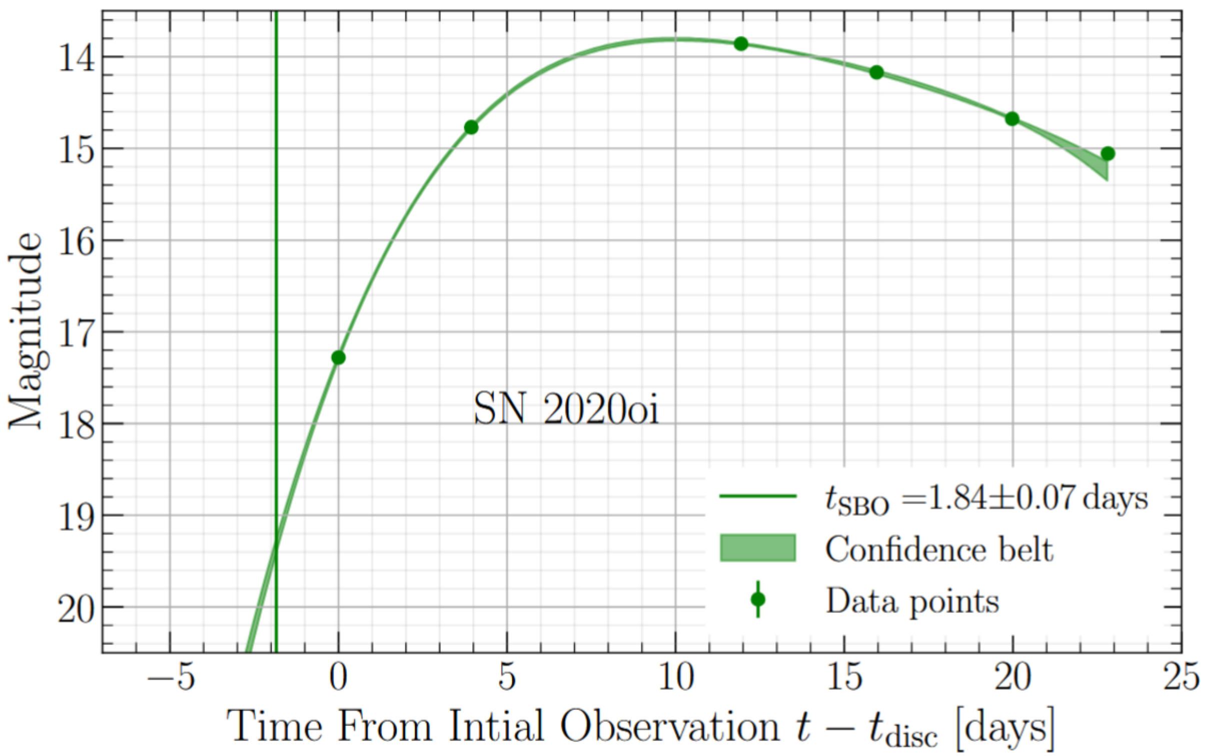

https://journals.aps.org/prd/abstract/10.1103/PhysRevD.110.042007

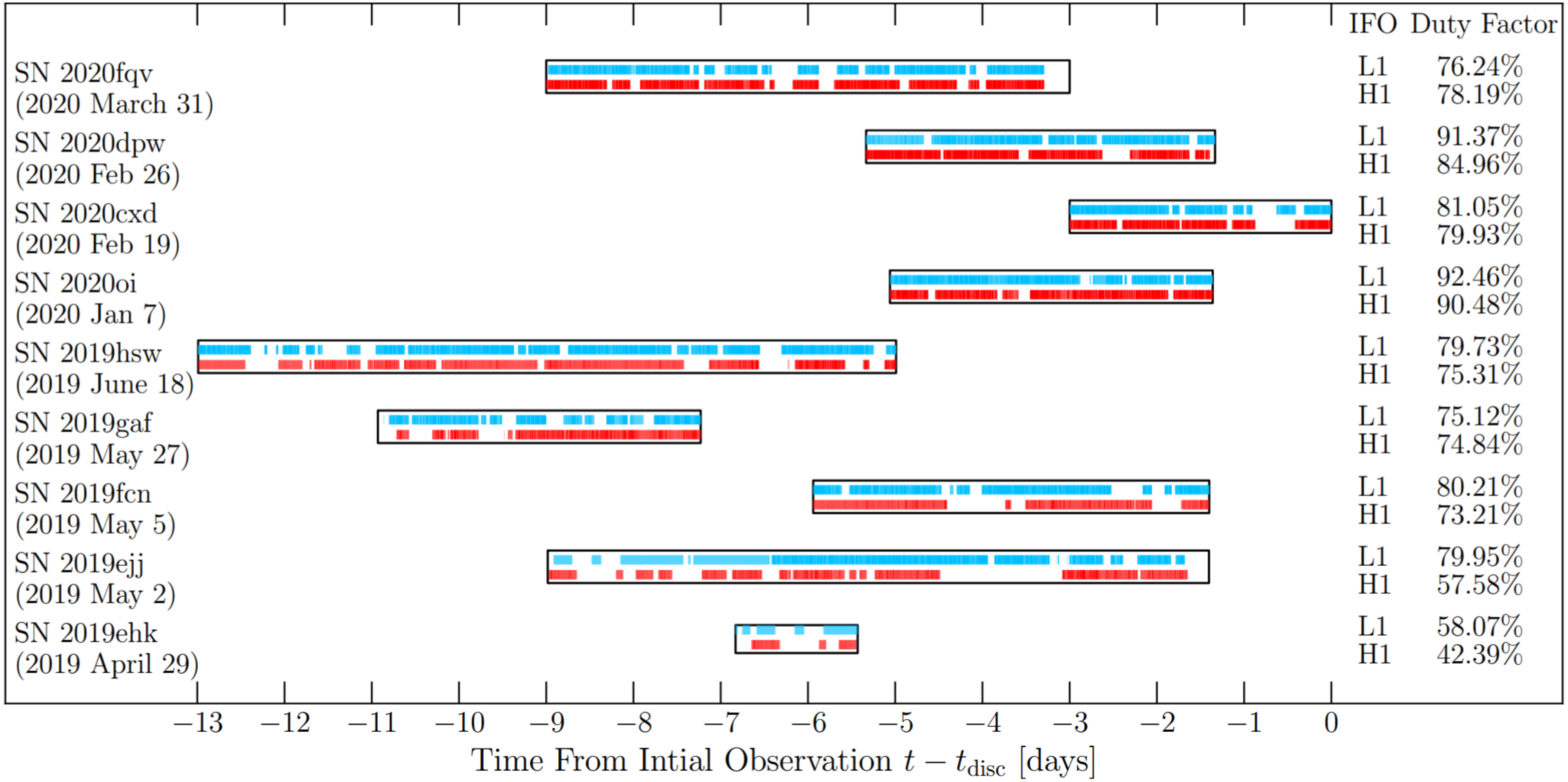

https://journals.aps.org/prd/abstract/10.1103/PhysRevD.110.042007

$$\mathrm{FAP} = 1 - e^{-(t_2 - t_1)\mathrm{FAR}} \simeq (t_2 - t_1)\mathrm{FAR}, \qquad (31)$$

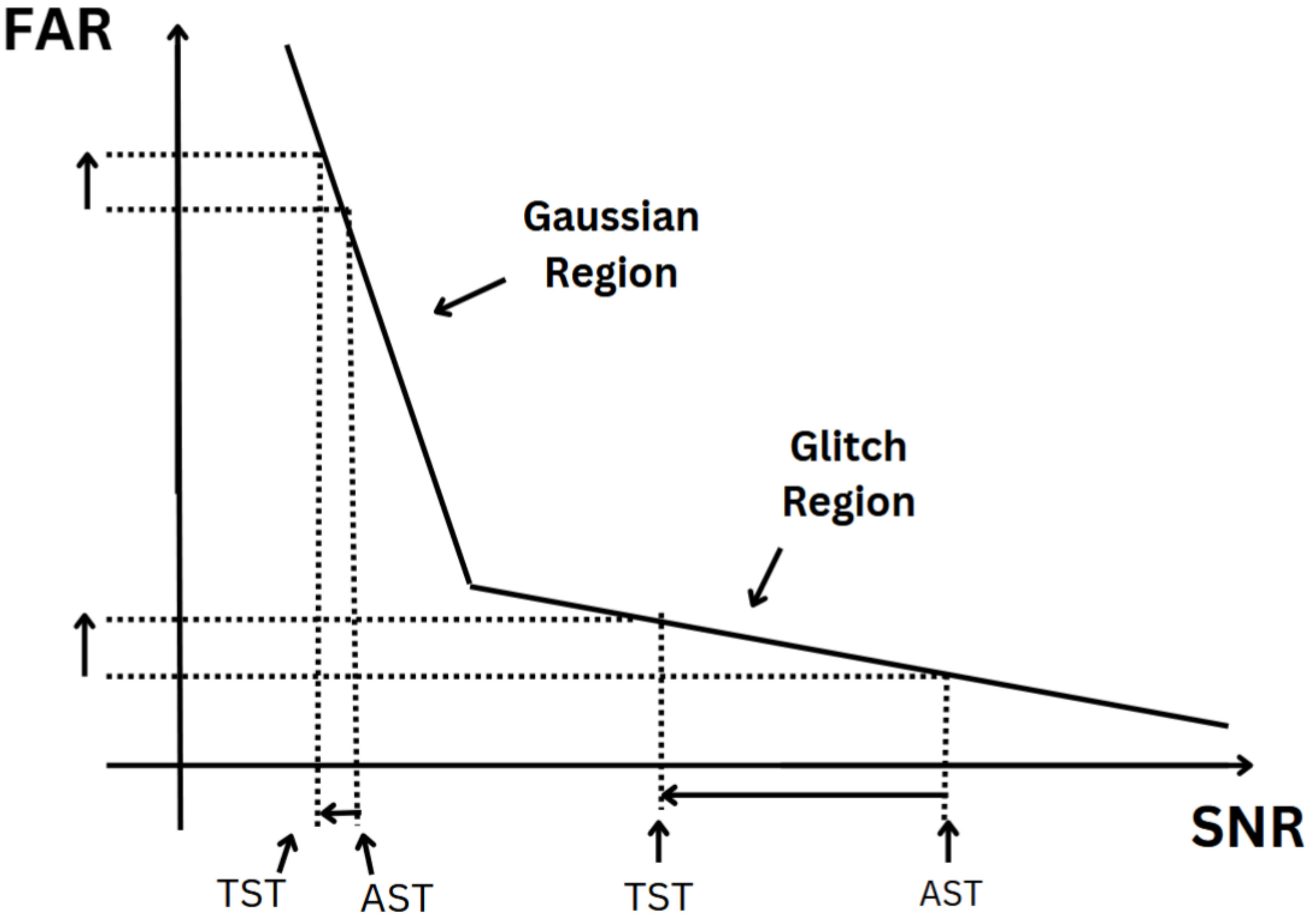

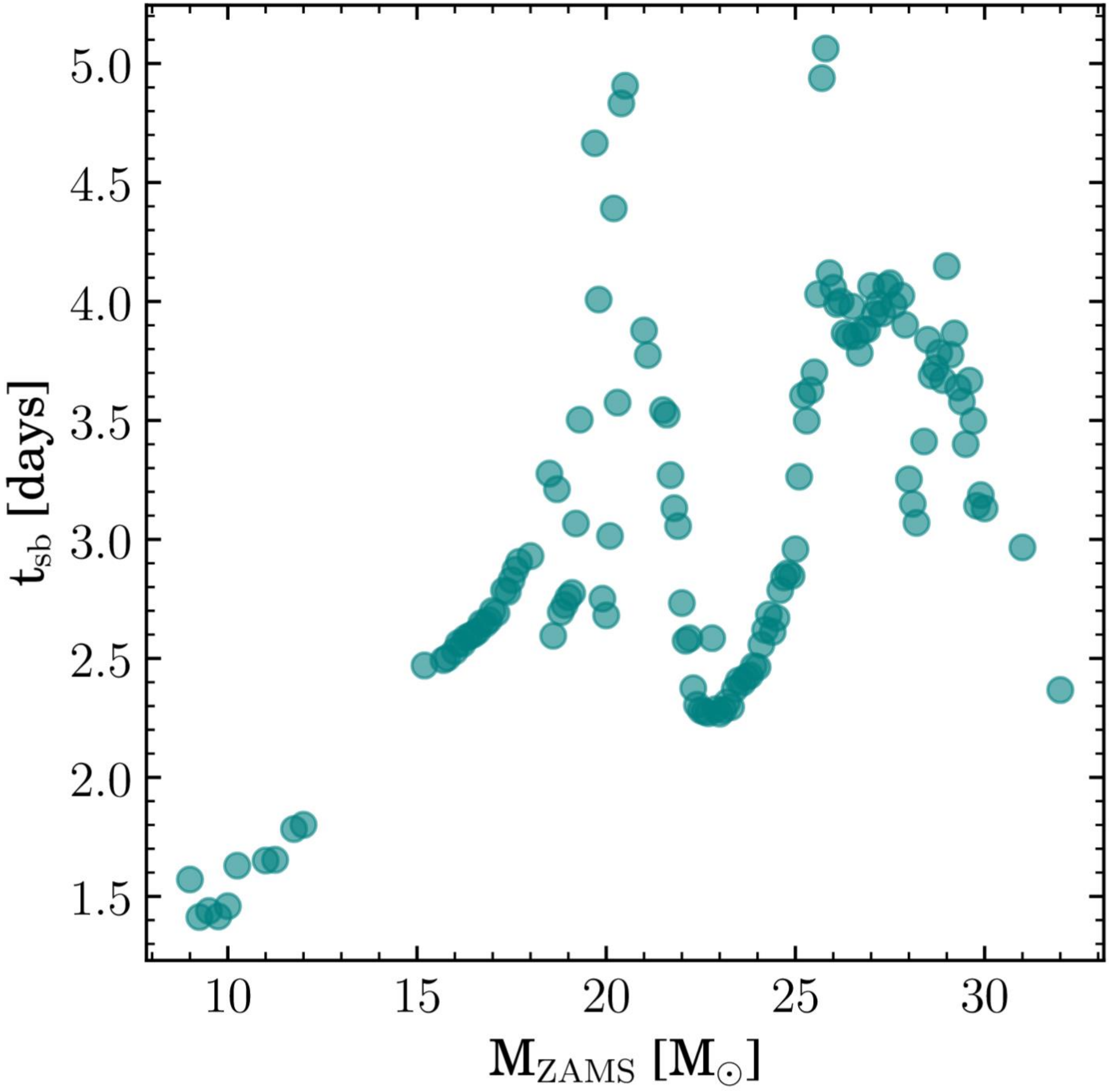

Time for shock breakout for the STIR + SNEC models.

https://arxiv.org/abs/2401.11635

https://iopscience.iop.org/article/10.3847/1538-4357/ac77f3

03 Data CCSN search

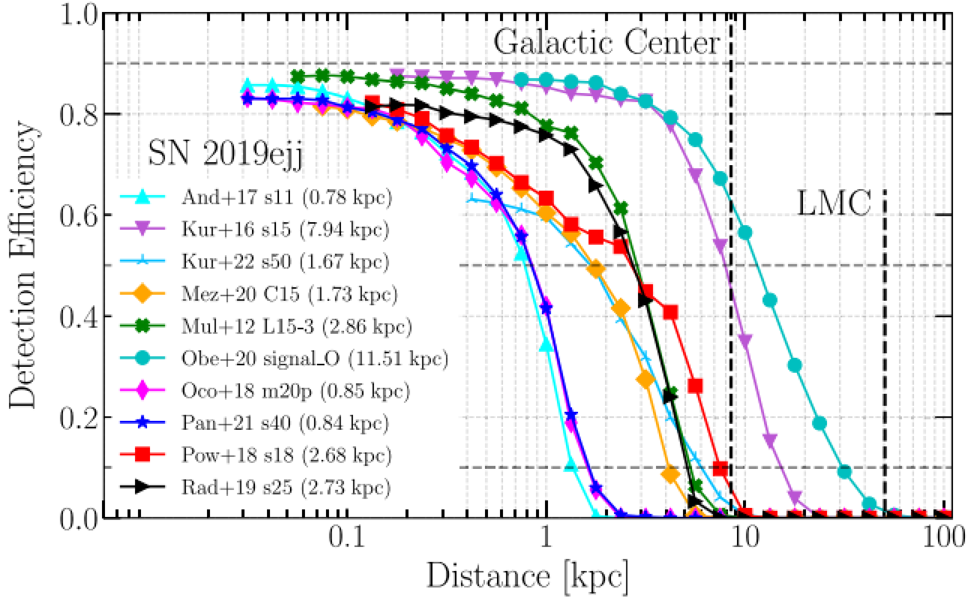

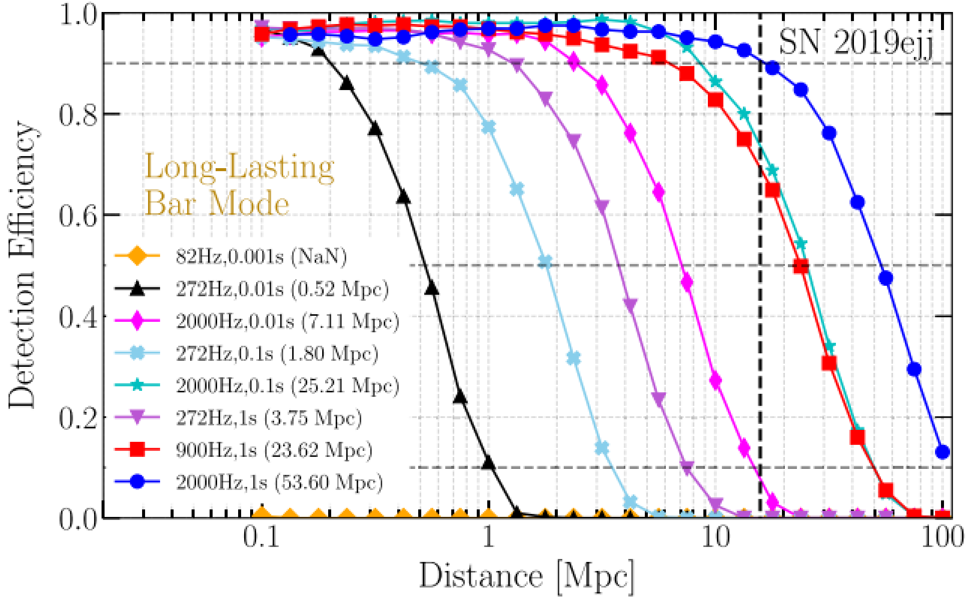

FAR = 1/100 years

Phys. Rev. D **110**, 042007

Supernova	And+17	Kur+16	Kur+22	Mez+20	Mul+12	Obe+20	Oco+18		Pan+21	Pow+18		Rad+19		
	s11	s15	s50	C15	L15-3	signal_O	m20	m20p	s40	s18	s3.5	s9	s13	s25
SN 2019ehk	-	6.57	-	0.52	2.47	4.22	0.18	0.77	0.38	3.05	1.54	0.16	0.33	3.11
SN 2019ejj	0.78	7.94	1.67	1.73	2.86	11.51	0.64	0.85	0.84	2.68	1.79	0.26	0.61	2.73
SN 2019fcn	0.58	7.40	0.80	0.84	2.46	8.81	0.50	0.64	0.58	0.83	0.87	0.22	0.49	1.86
SN 2019hsw	0.70	5.60	1.82	2.24	2.33	13.40	0.60	0.76	0.77	3.85	2.04	0.17	0.49	2.82
SN 2020oi	0.63	6.53	-	1.15	2.36	9.52	0.56	0.70	0.61	1.71	0.94	0.21	0.52	1.96
SN 2020cxd	**0.88**	**8.90**	**2.13**	**2.74**	**3.17**	**14.65**	**0.74**	**0.95**	**0.94**	**4.74**	**2.38**	**0.27**	**0.67**	**3.15**
SN 2020dpw	0.79	8.66	1.70	2.46	2.96	13.43	0.68	0.85	0.90	4.30	2.24	0.27	0.61	2.86
SN 2020fqv	0.73	6.86	1.56	2.38	2.53	13.42	0.65	0.82	0.81	4.17	2.17	0.21	0.55	2.90

Phys. Rev. D **110**, 042007

All-sky search for short gravitational-wave bursts in the third Advanced LIGO and Advanced Virgo run

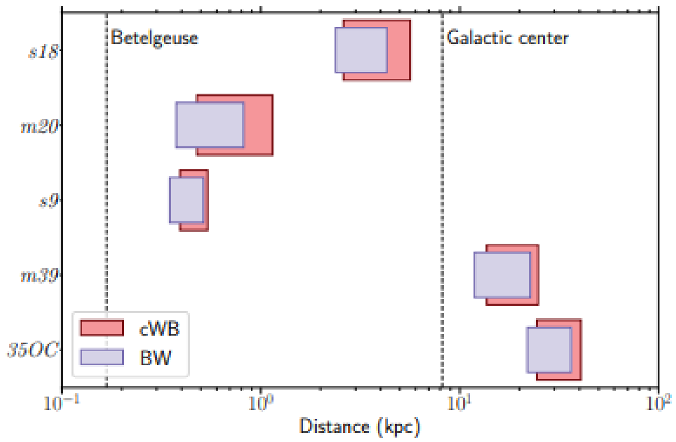

FIG. 7. Distances at which 50% and 10% detection efficiencies are reached for different CCSN waveforms indicated by the left sides and right sides of rectangles, respectively. Different colors represent results from the two detection algorithms used.

Phys. Rev. D **104**, 122004

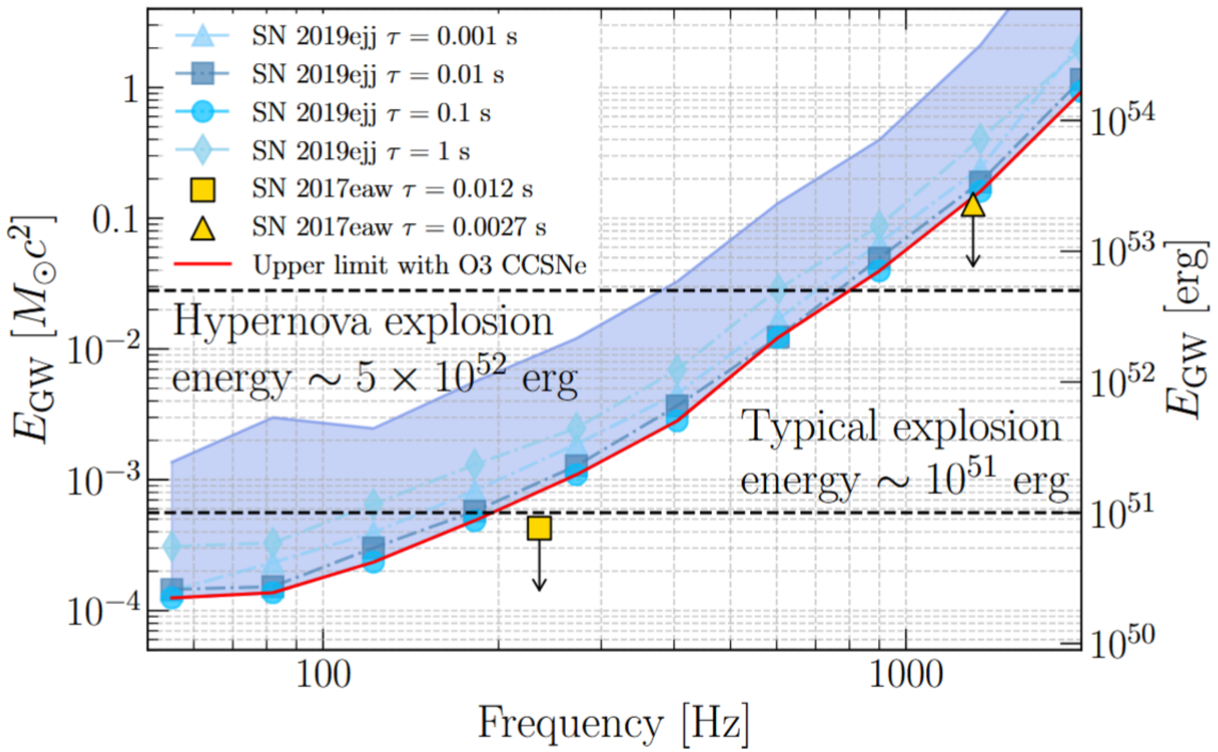

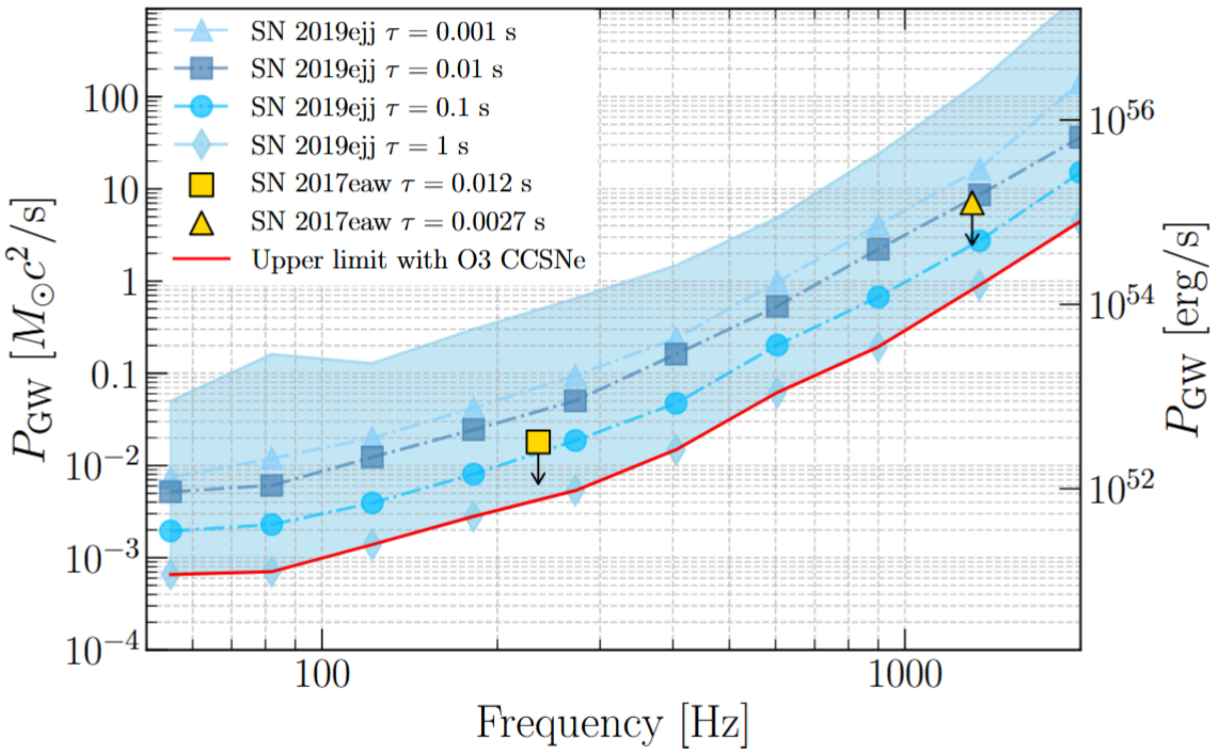

$$E_{\rm GW} = \frac{2}{5}\frac{\pi^2 c^3}{G} D^2 f_0^2 h_{\rm rss50}^2$$

Phys. Rev. D **110**, 042007

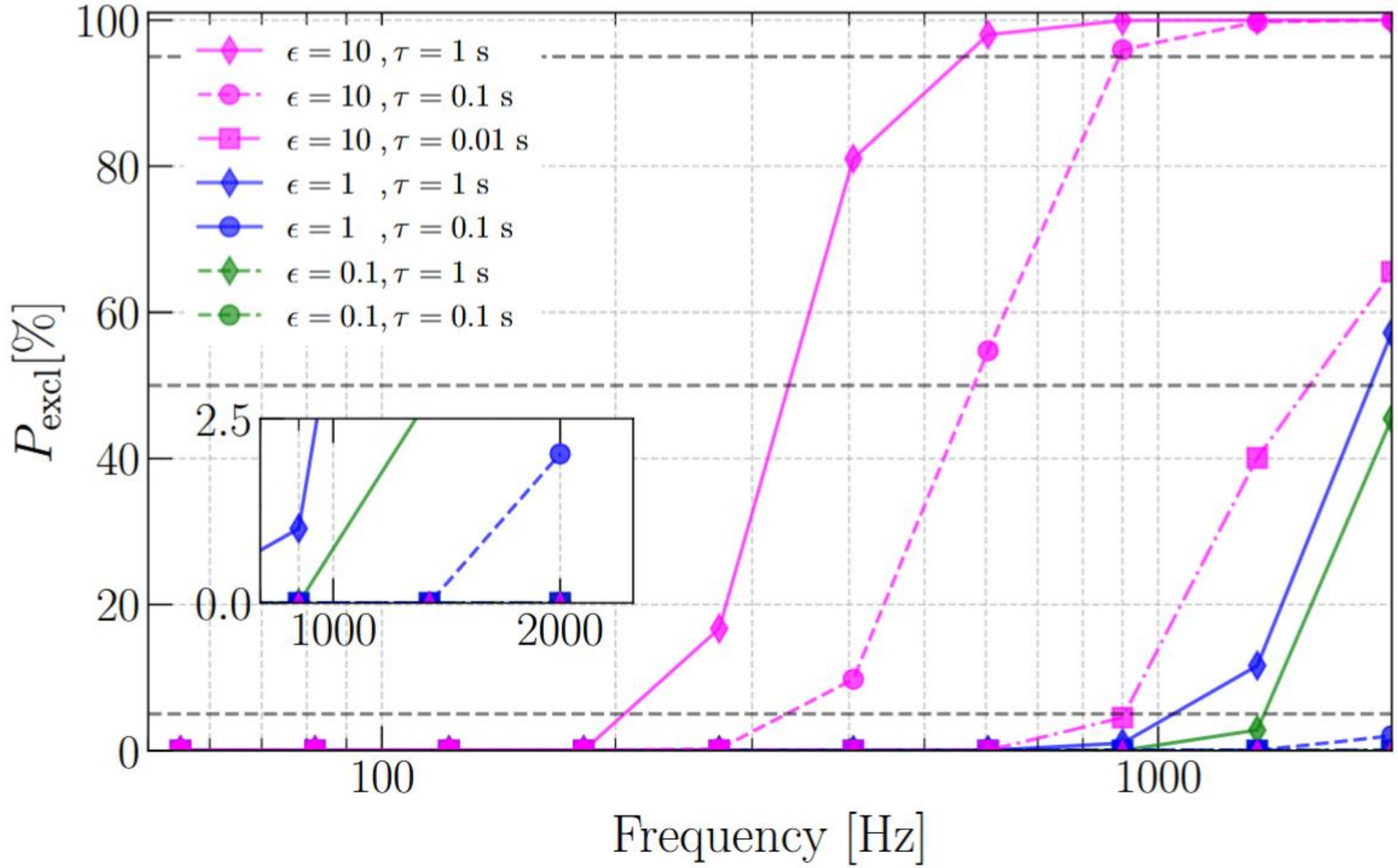

$$P_{\mathrm{excl}} = 1 - \prod_{i=1}^{N} (1 - \varepsilon_i(D_i))$$

https://journals.aps.org/prd/abstract/10.1103/PhysRevD.110.042007

GW and ν emission

Strong SASI modulations

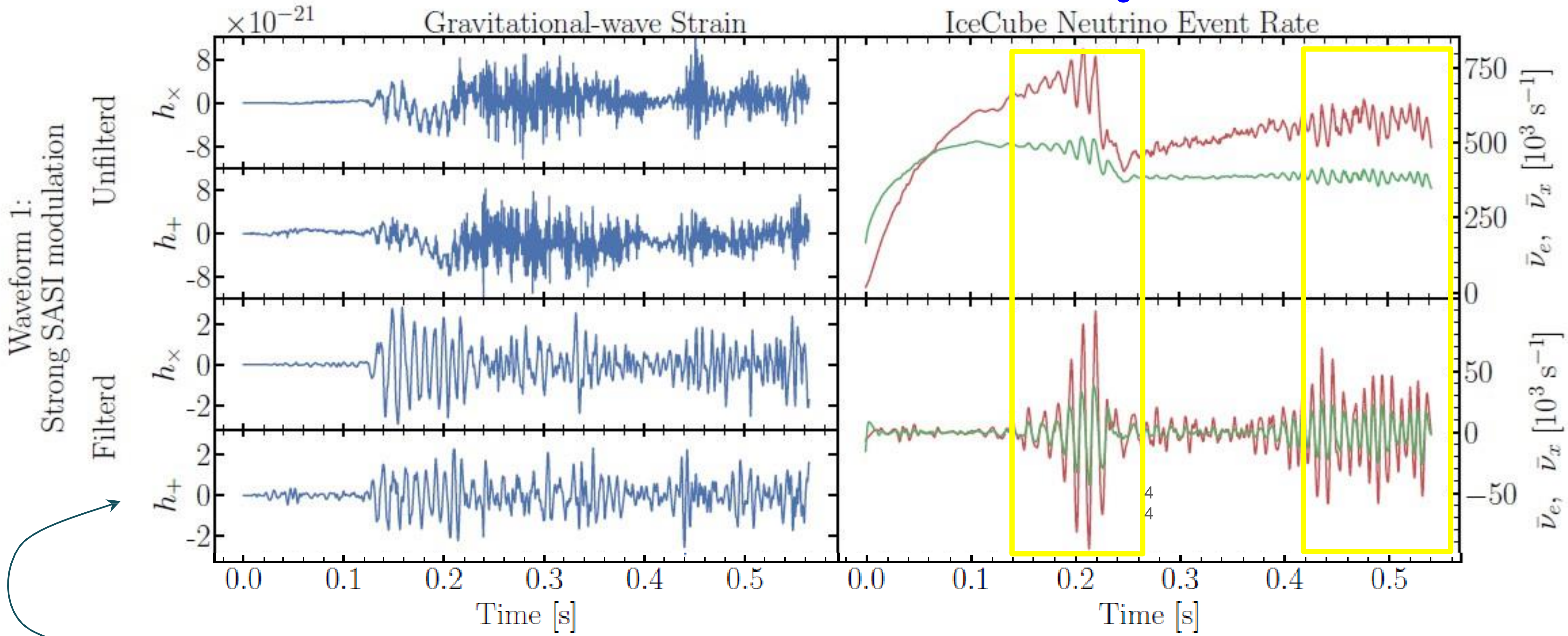

Band pass filter of 50-300 Hz

3 cases explored changing observer directionality strong, intermediate and weak SASI modulations

Phys. Rev. D 108, 103036, 2023

Results, benchmark distance: 0.5 kpc, FAR=1/1y

No real GW data used. Considering simulated white noise based on O5 spectral sensitivity (*)

Efficiency: compatible among 5% difference

Using two SASI periods not performing better

- they do not align
- optimal direction for first SASI is not optimal for second SASI

(*) Living Rev Relativ 23, 3 (2020)

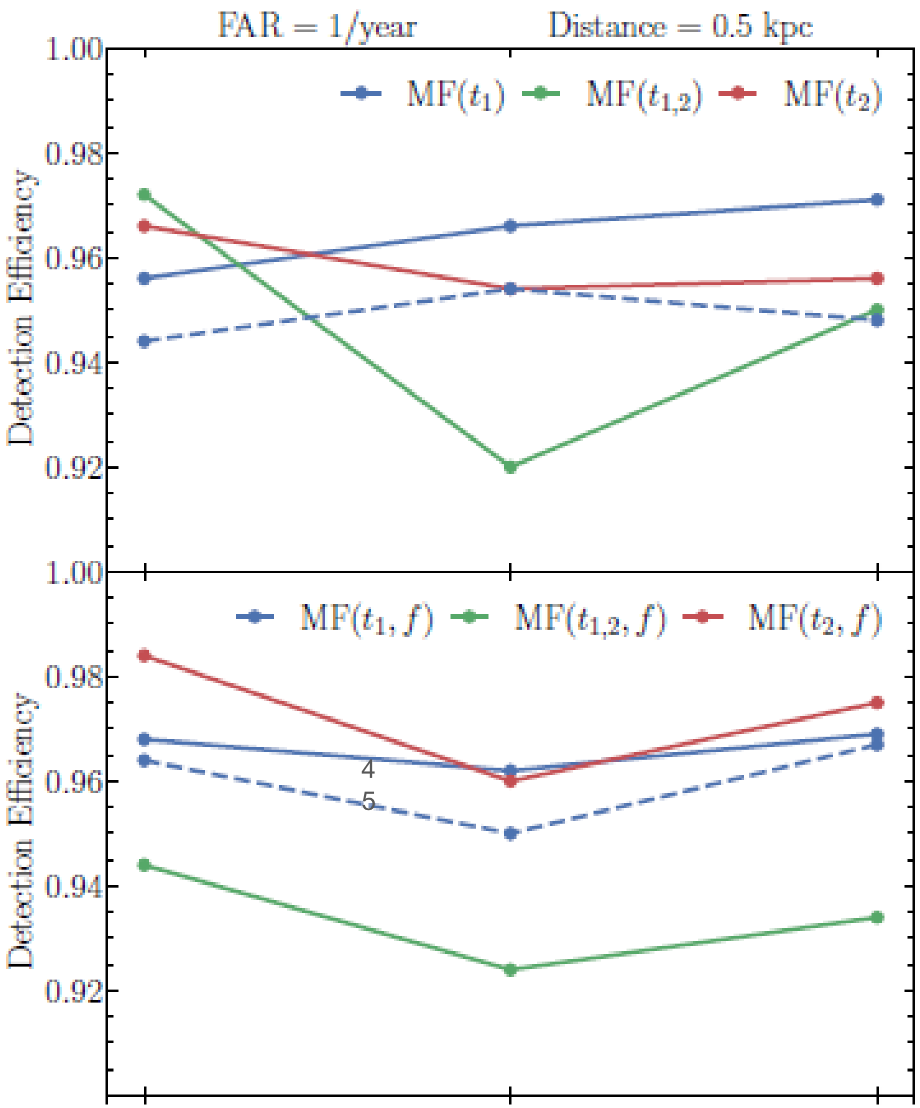

Phys. Rev. D 108, 103036, 2023

Detection Horizon

At low distance (<1.5 kpc) the matched-filter have better efficiency, but soon we arrive at high distance, EP performs better

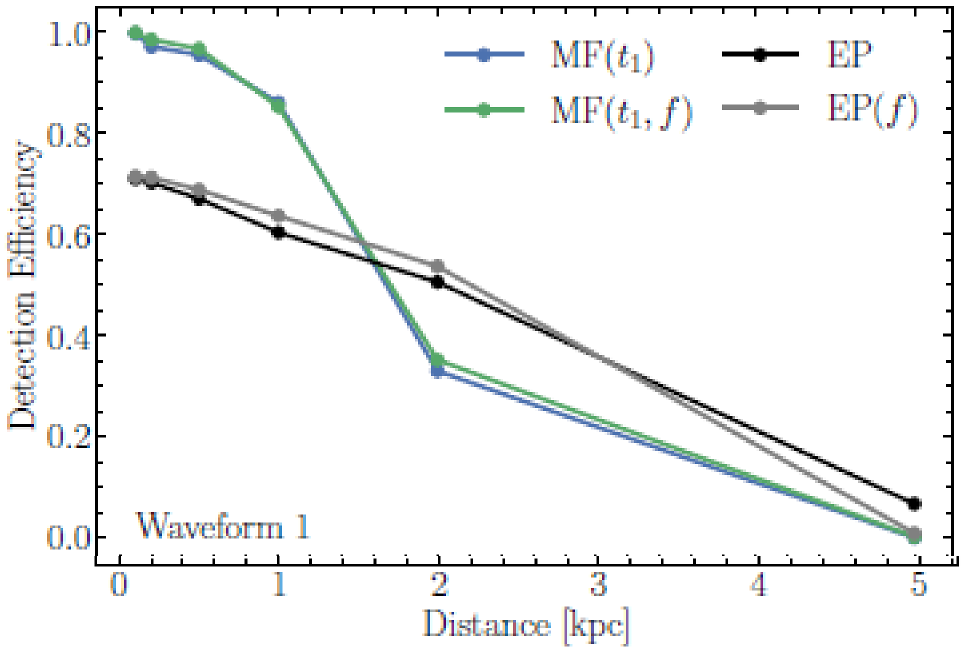

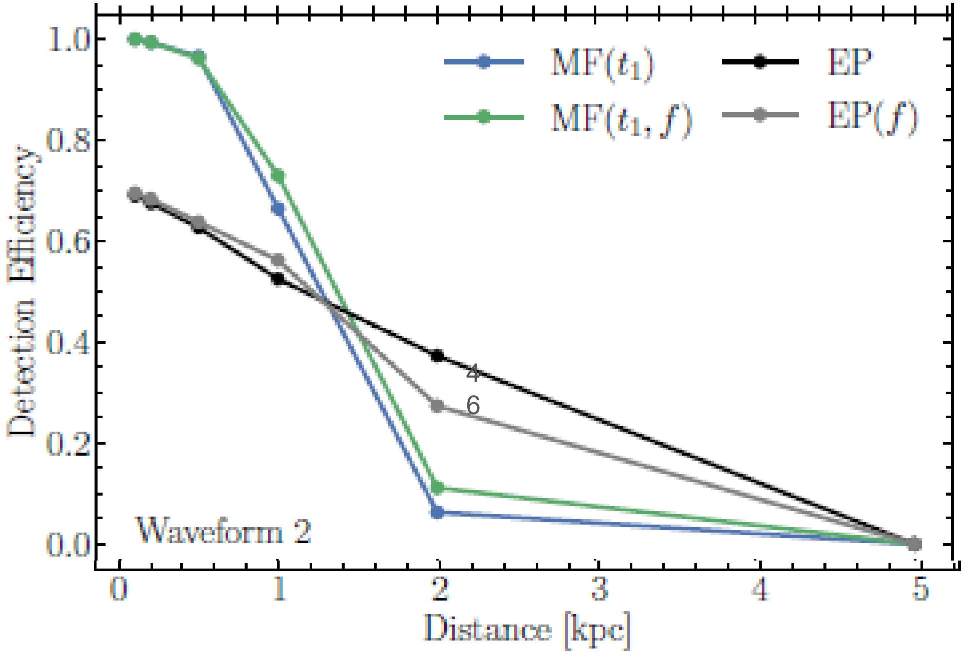

Phys. Rev. D 108, 103036, 2023

Distributional methods

- Investigating the potential of different distributional tests in the detection of Core-Collapse supernova gravitational waves for quiet signals that would have been previously missed.
- We use coherent WaveBurst to look at the loud events in a span of time and form a metric for each event, which we collect to form 'shaped' distributions containing the signal and all the loud noise.
- Our method focuses on applying non-parametric distributional tests to separate noise-only distributions with those containing our injected GW signal.
- With an understanding of the behavior of these tests and tuning parameters, we have a method to search for presence of supernova GW at in groups where the signals may be much quieter (and therefore farther away) than before possible.
- See Kya Schluterman poster

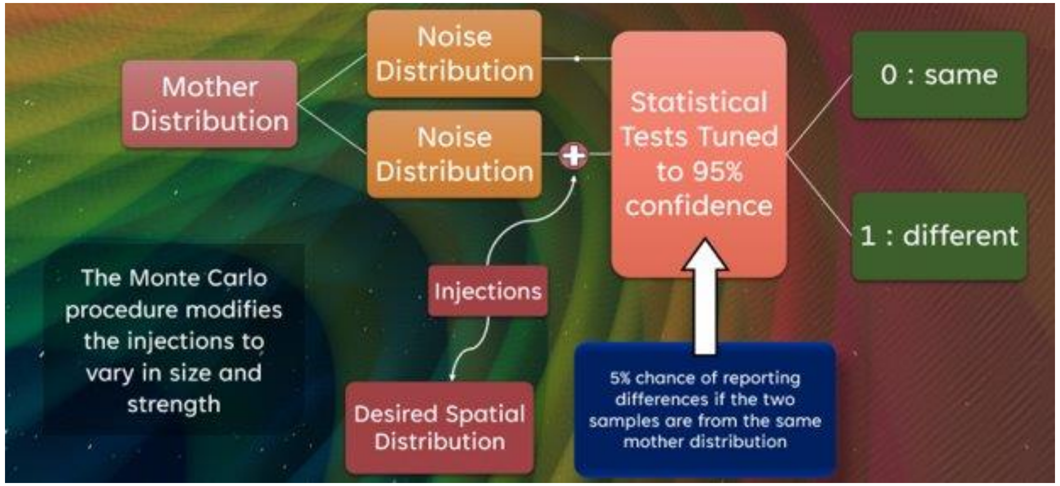

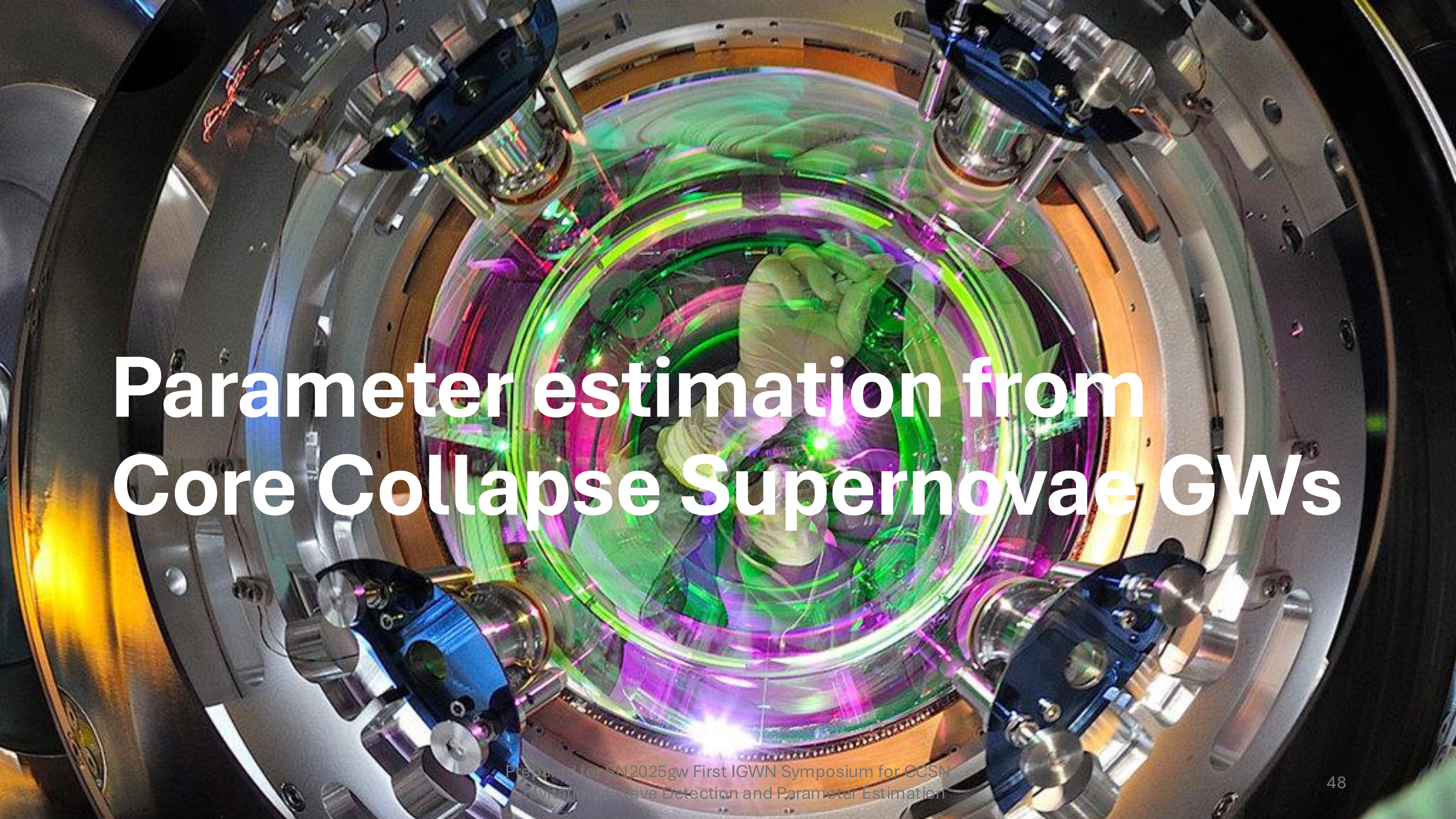

Parameter estimation from Core Collapse Supernovae GWs

Parameter Estimation

For CCSNe, the estimation of physical parameters is performed in two steps:

(1) parameters characterizing deterministic aspects of the GWs from CCSNe are estimated.

(2) these estimates are connected to fundamental physical properties (e.g., the equation of state, PNS radius, PNS mass, EOS, Rotation).

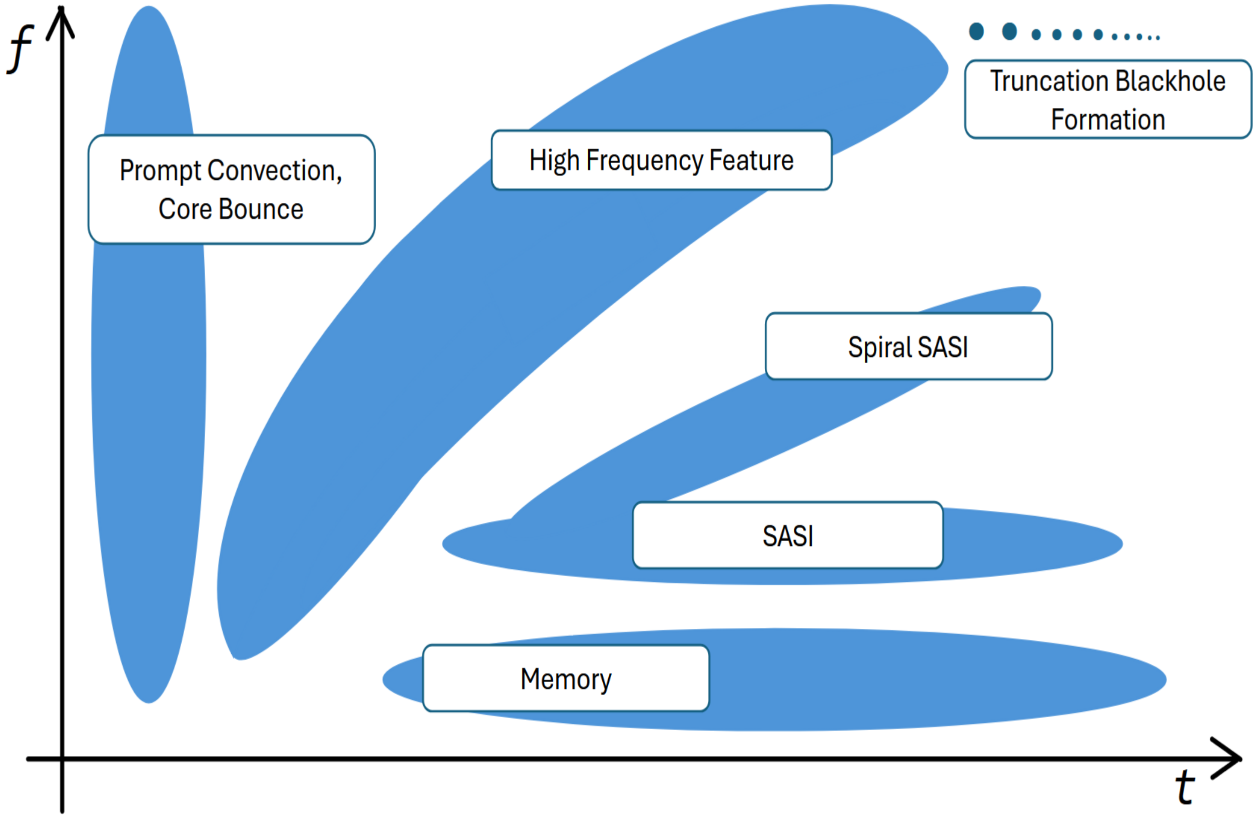

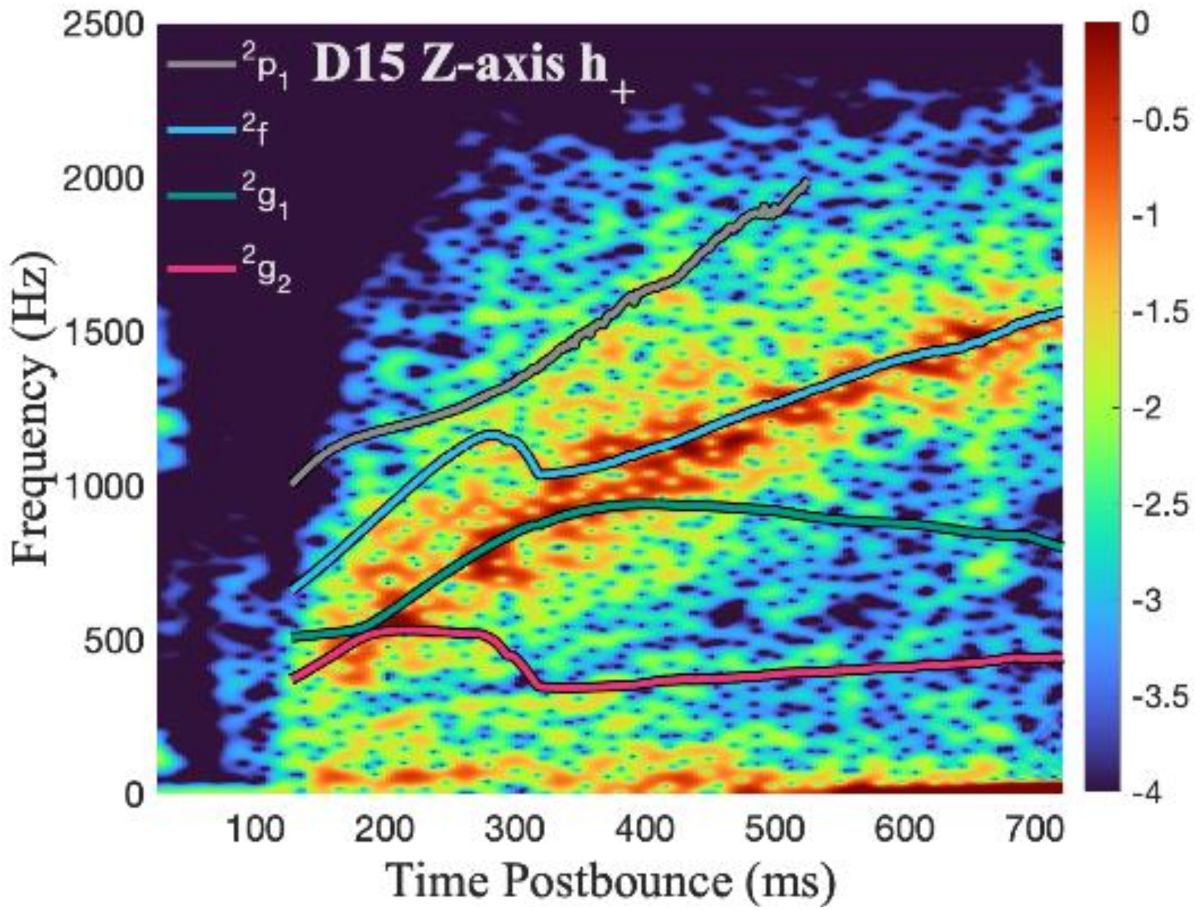

[Murphy et al. Phys. Rev. D (2025) arXiv:2503.06406]

The capability to reconstruct the waveform depends on the frequency content

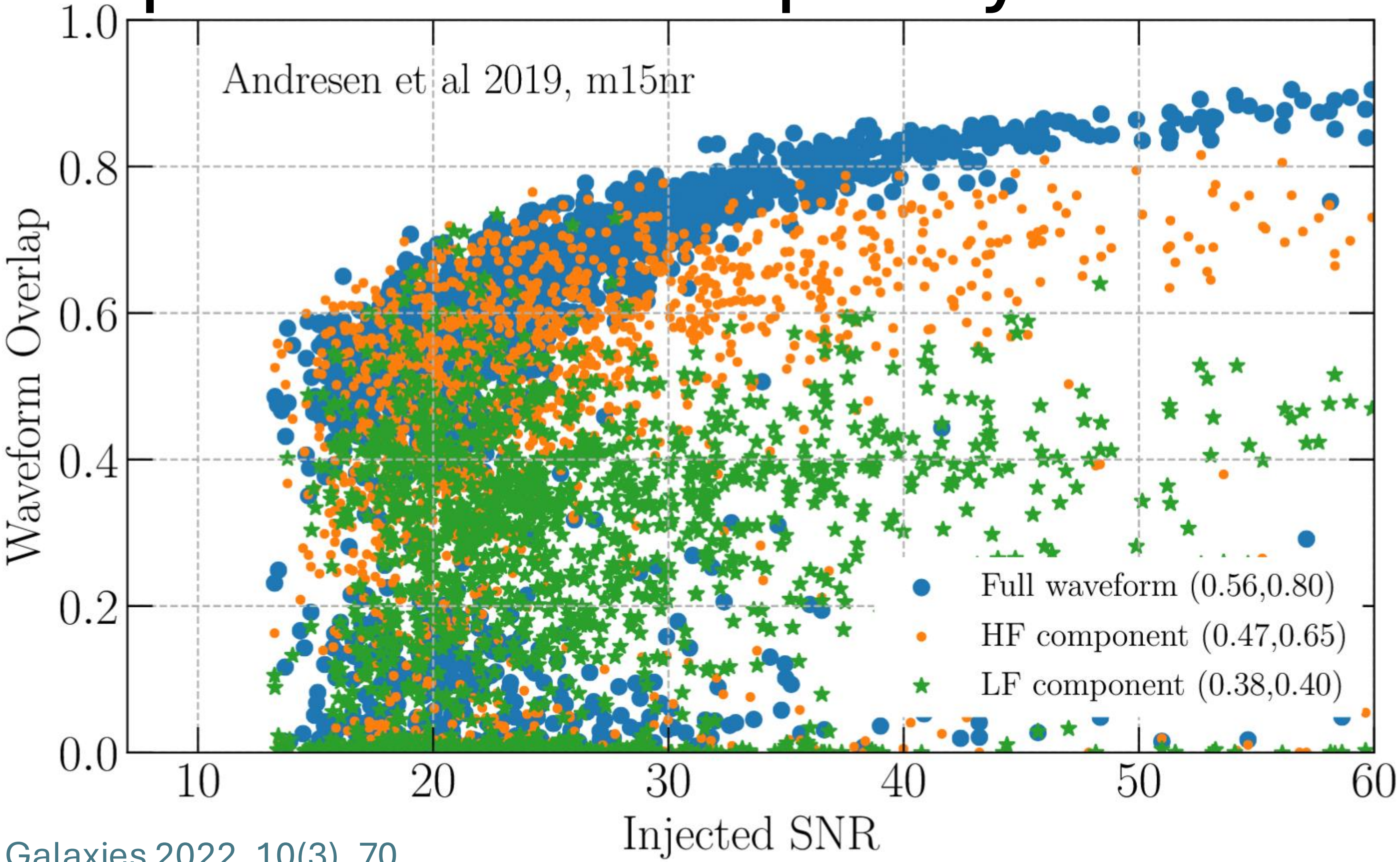

Waveform overlap as a function of injected SNR for m15nr model [30]. The accuracy of the full waveform increases with the SNR. However, in this example, each waveform component is reconstructed less accurately. The numbers in brackets are waveform overlaps at SNR 20 and 40, respectively, (for O > 0.2).

Galaxies 2022, 10(3), 70

High Frequency Feature

Deterministic Properties: Starting frequency, Initial slope, Curvature, Asymptotic frequency, Truncation frequency (BH production ?), abritrary polarization.

Physical Factors: Mass of the PNS, Radius of the PNS, EOS, chemical composition, active mode, degree of rotation (it might be easyer to decouple because of rarity of of rapidly rotating).

What can we learn if we provide the theorists a time frequency profile of it?

See also Alejandro Casallas's Presentation for the estimation of the initial slope.

Results

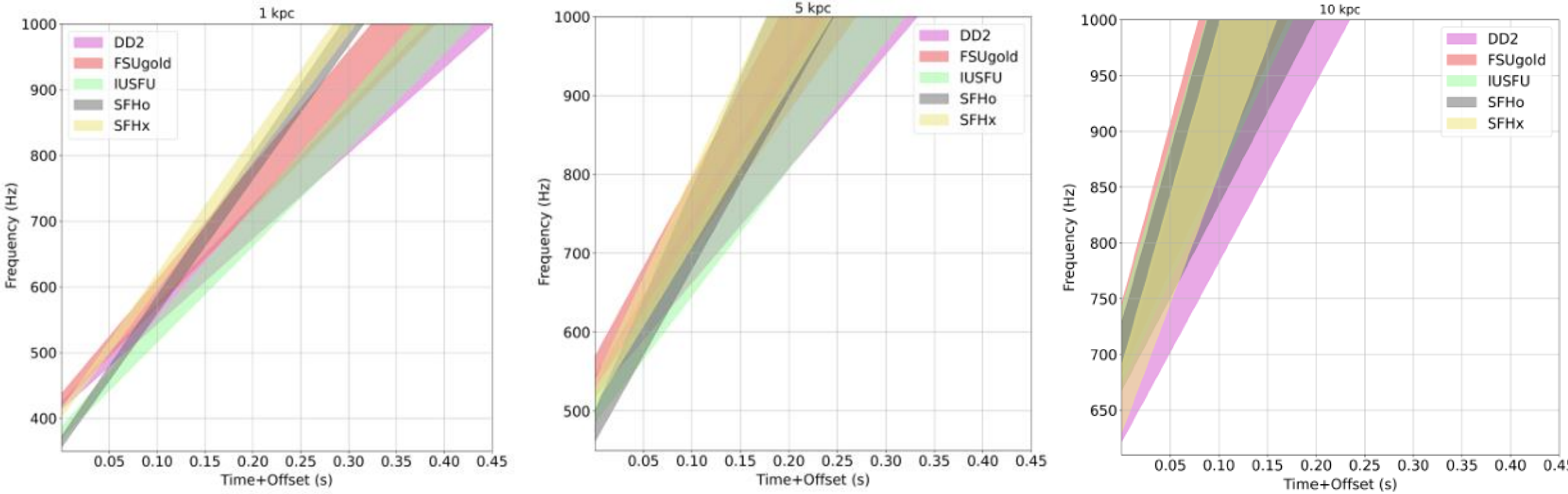

We see the emergence of two groupings: the steep-sloped E-SFHo and E-SFHx models and the more-shallow-sloped E-DD2 and E-IUFSU models.

EOS	s [Hz s^{-1}]	1 kpc $\hat{s}$ [Hz s^{-1}]	1 kpc STD [Hz s^{-1}]	1 kpc RMSE [Hz s^{-1}]	1 kpc MAPE [%]	5 kpc $\hat{s}$ [Hz s^{-1}]	5 kpc STD [Hz s^{-1}]	5 kpc RMSE [Hz s^{-1}]	5 kpc MAPE [%]	10 kpc $\hat{s}$ [Hz s^{-1}]	10 kpc STD [Hz s^{-1}]	10 kpc RMSE [Hz s^{-1}]	10 kpc MAPE [%]
DD2	1398	1402	103.54	301.72	5.6	1742	293.13	223.11	21	2377	765.30	635.93	32
FSUGold	1665	1610	126.93	228.84	1.2	2002	258.56	332.91	15	2544	678.70	468.19	27
IUFSU	1502	1566	100.66	229.11	3.1	1812	201.69	154.25	17	2404	555.41	526.20	24
SFHo	2131	2092	52.63	249.39	0.5	2501	313.45	256.74	18	2670	401.92	486.82	21
SFHx	2000	2003	60.43	159.30	0.6	2311	298.12	106.10	12	2687	368.12	416.60	20

EOS	1 kpc $\bar{\beta}$ [Hz]	1 kpc STD [Hz]	1 kpc RMSE [Hz]	1 kpc MAPE [%]	5 kpc $\bar{\beta}$ [Hz]	5 kpc STD [Hz]	5 kpc RMSE [Hz]	5 kpc MAPE [%]	10 kpc $\bar{\beta}$ [Hz]	10 kpc STD [Hz]	10 kpc RMSE [Hz]	10 kpc MAPE [%]
DD2	419	5.21	11.23	4.32	531	12.94	13.54	10.18	649	27.39	31.30	23.62
FSUGold	429	8.51	13.47	6.05	550	18.92	27.14	15.73	714	31.32	34.01	30.98
IUFSU	378	9.01	14.04	6.67	505	20.04	29.37	16.34	708	33.51	36.37	33.75
SFHo	364	8.39	12.57	6.01	481	19.49	27.01	15.24	698	30.21	33.23	33.13
SFHx	408	5.87	11.74	4.94	523	15.50	25.21	11.36	660	29.94	32.12	26.17

The HFF tests Microphysics

- Gravitational waves and neutrinos provide data on PNS evolution
- PNS properties connected to nuclear equation of state
  - Multi-messenger detections are a window to deep within the PNS

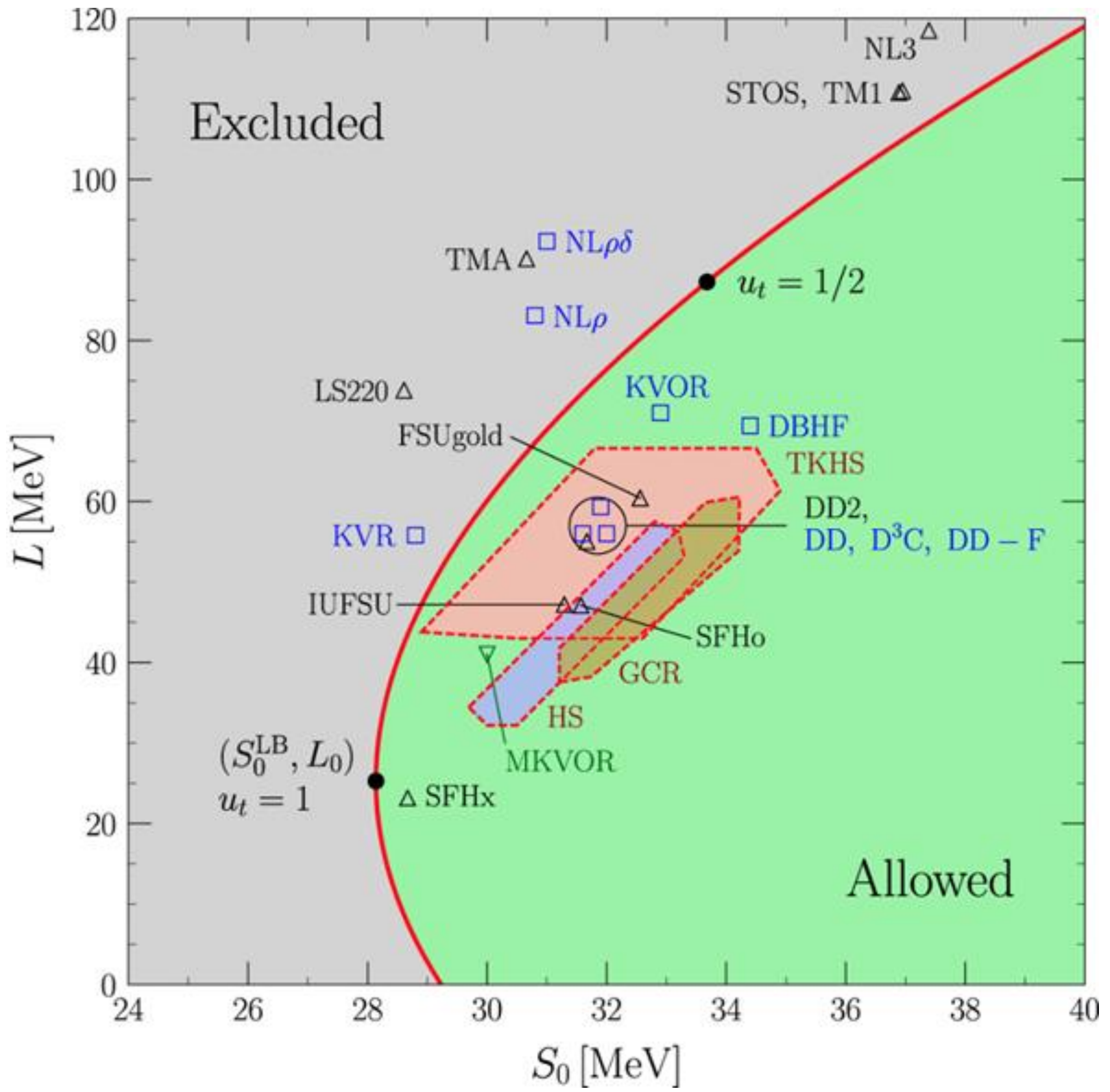

Tews et al. Astrophys. J. 848:105 (2017)

Standing Accretion Shock Instability

(SASI)

Parameters: frequency in both channels, duration, polarization.

See also Vicente Sierra and Zidu Lin presentations

https://journals.aps.org/prd/abstract/10.1103/PhysRevD.107.083017

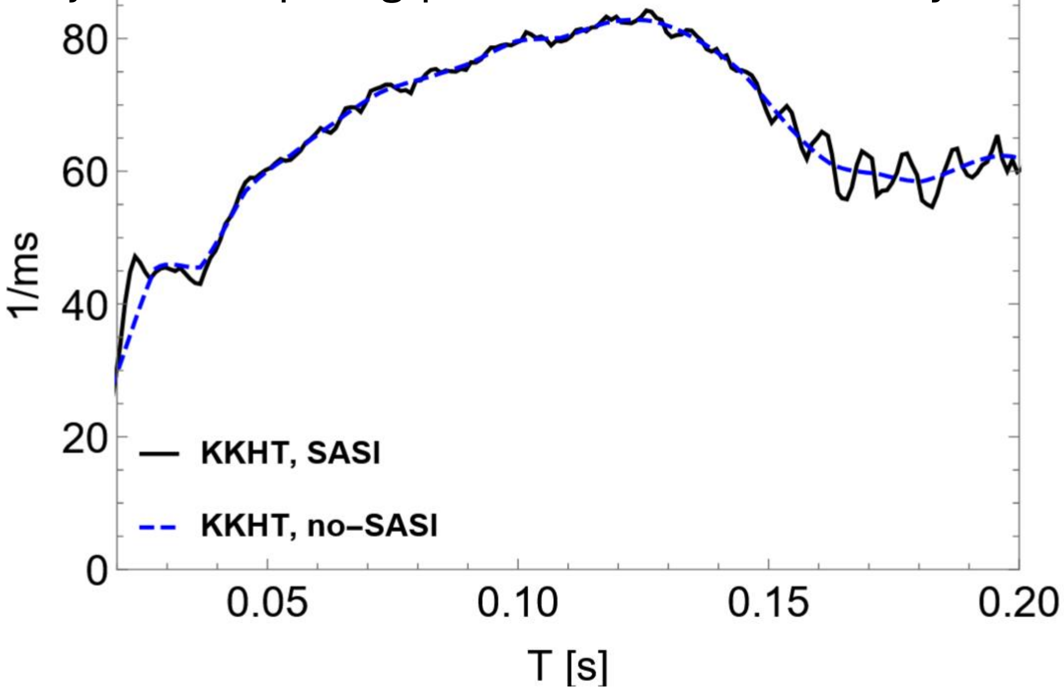

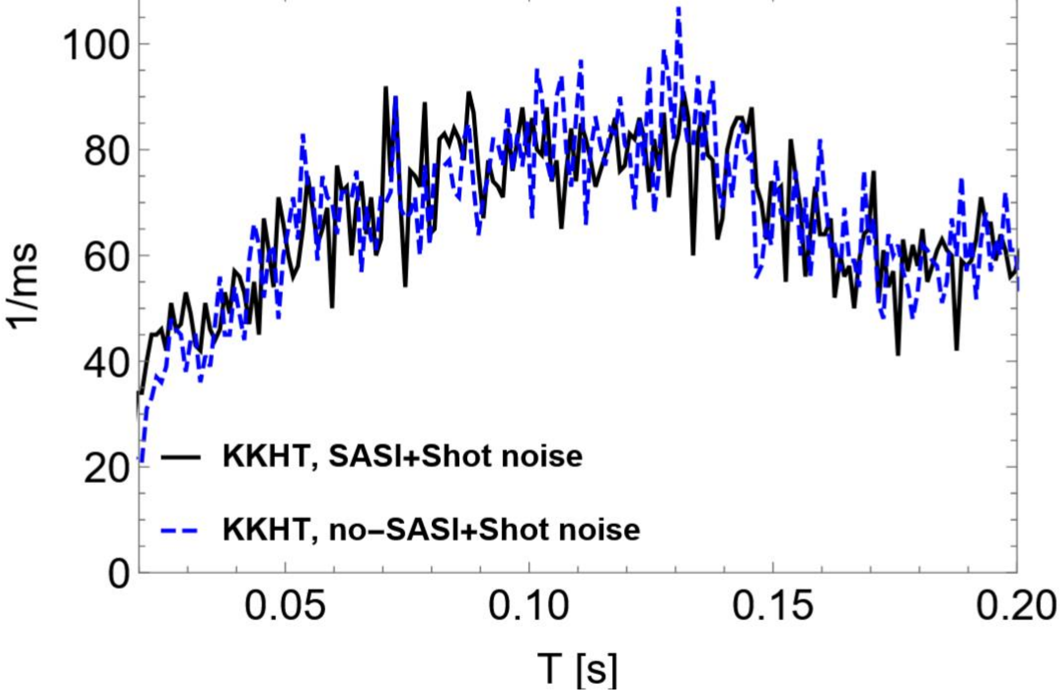

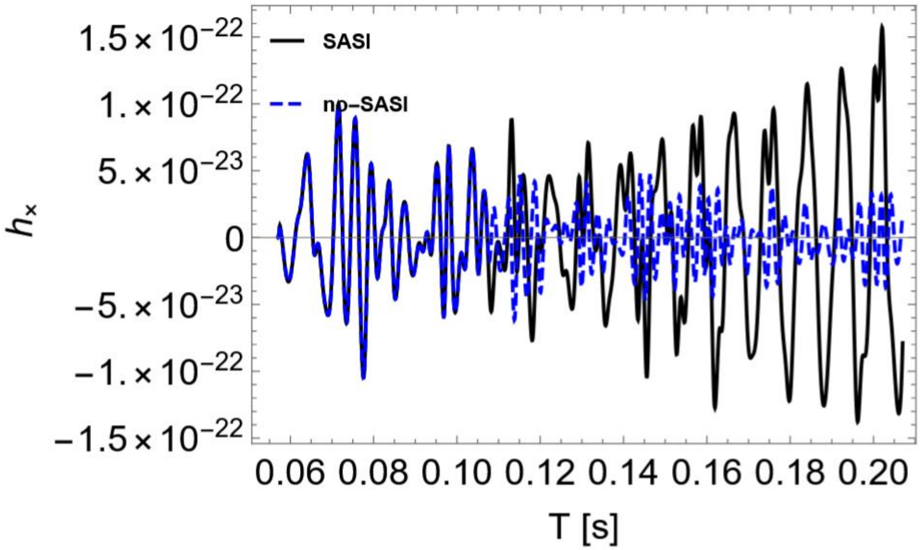

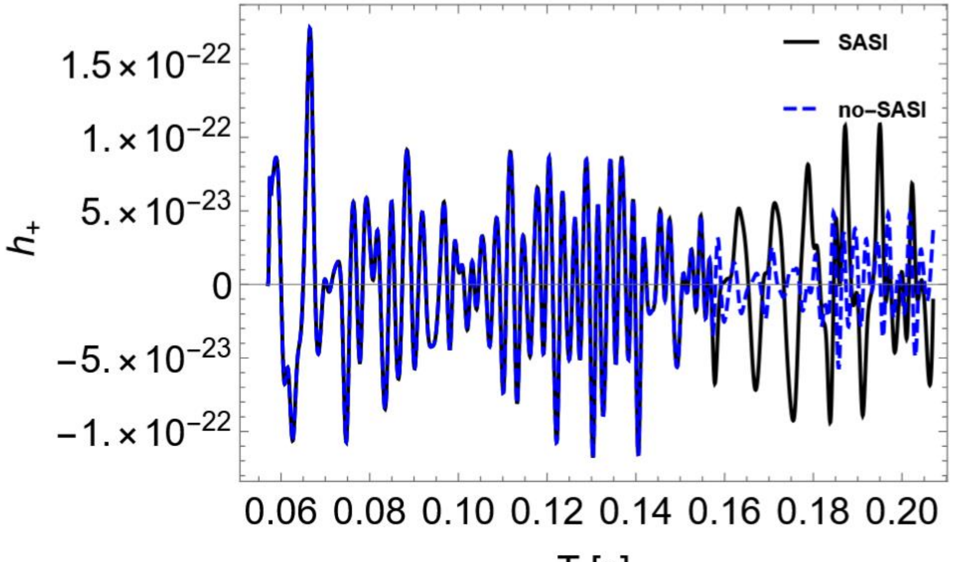

$$T_{SASI} = \int_{r_\nabla}^{r_{sh}} \frac{dr}{|V_r|} + \int_{r_\nabla}^{r_{sh}} \frac{dr}{c_s - |V_r|}. \qquad (1)$$

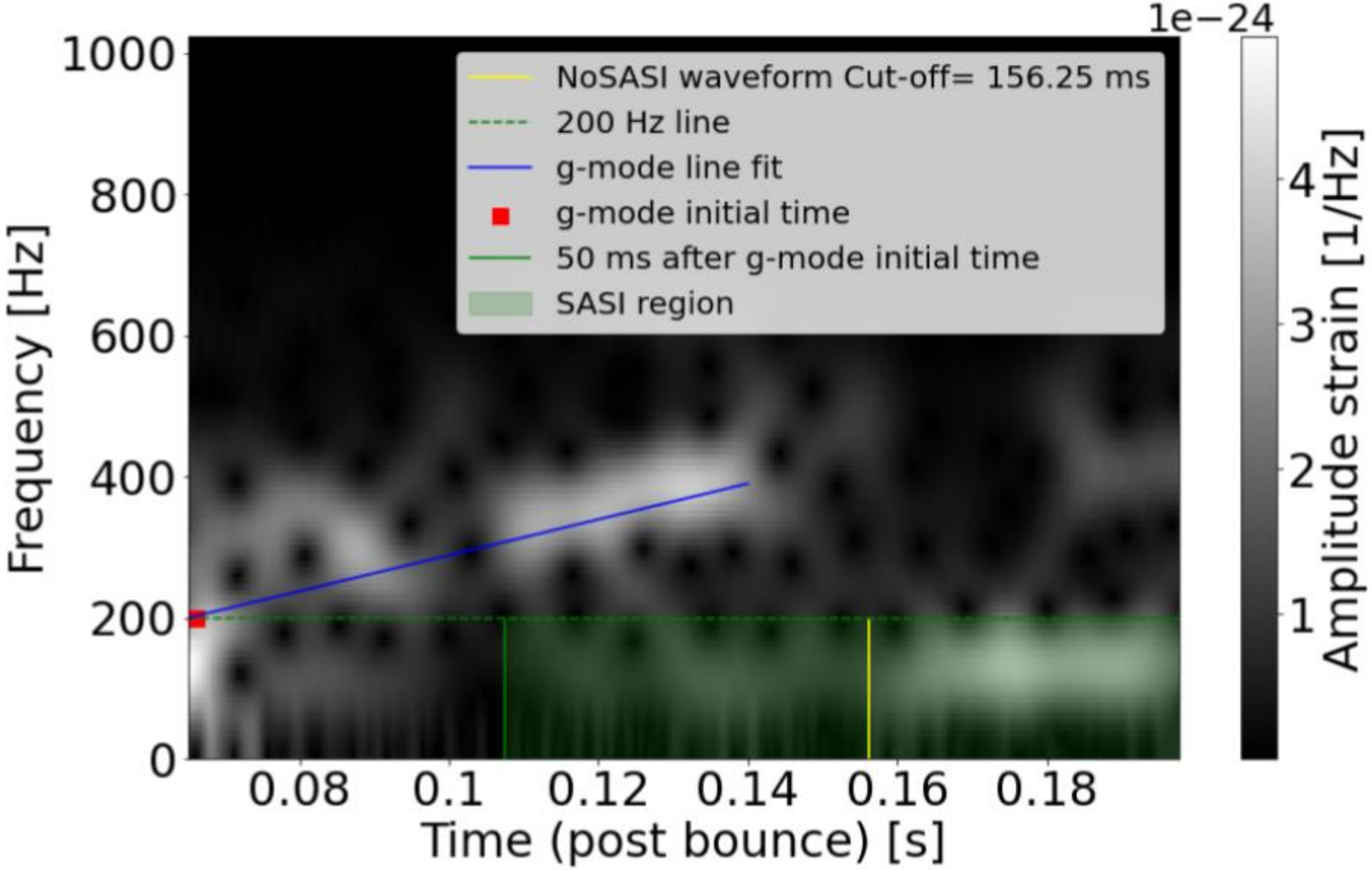

https://journals.aps.org/prd/abstract/10.1103/PhysRevD.107.083017

$$f_{\mathrm{GW}} = \frac{\sum_{i \in SASI} \rho^i f_c^i}{\sum_{i \in SASI} \rho^i} , \tag{19}$$

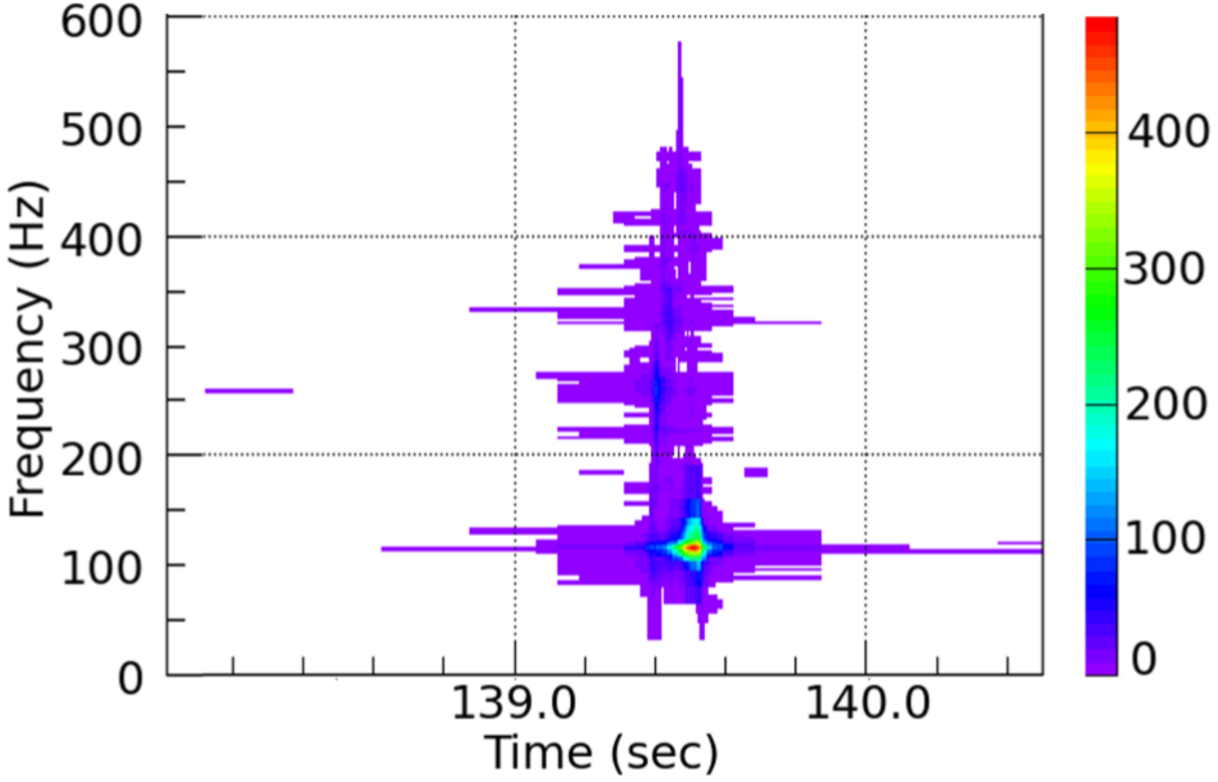

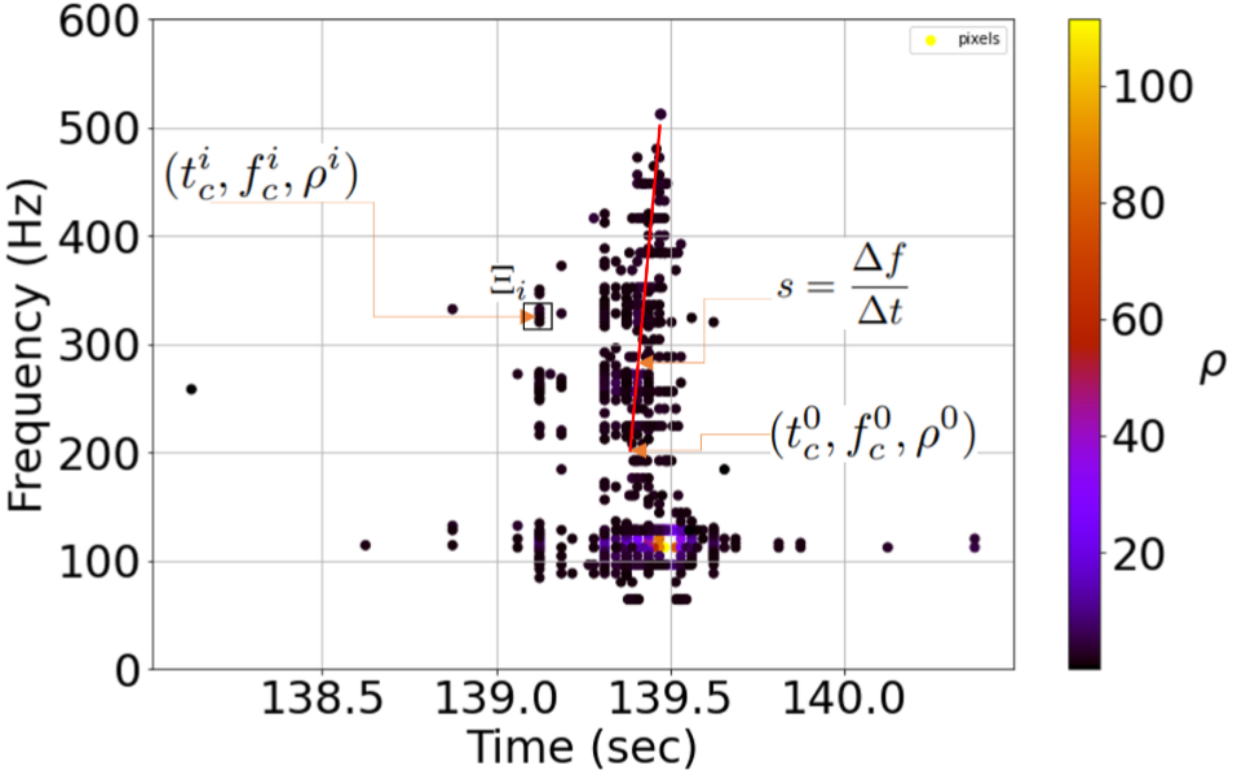

https://journals.aps.org/prd/abstract/10.1103/PhysRevD.107.083017

$$f_{\rm GW} = \frac{\sum_{i\in SASI}\rho^i f_c^i}{\sum_{i\in SASI}\rho^i} \;, \qquad (19)$$

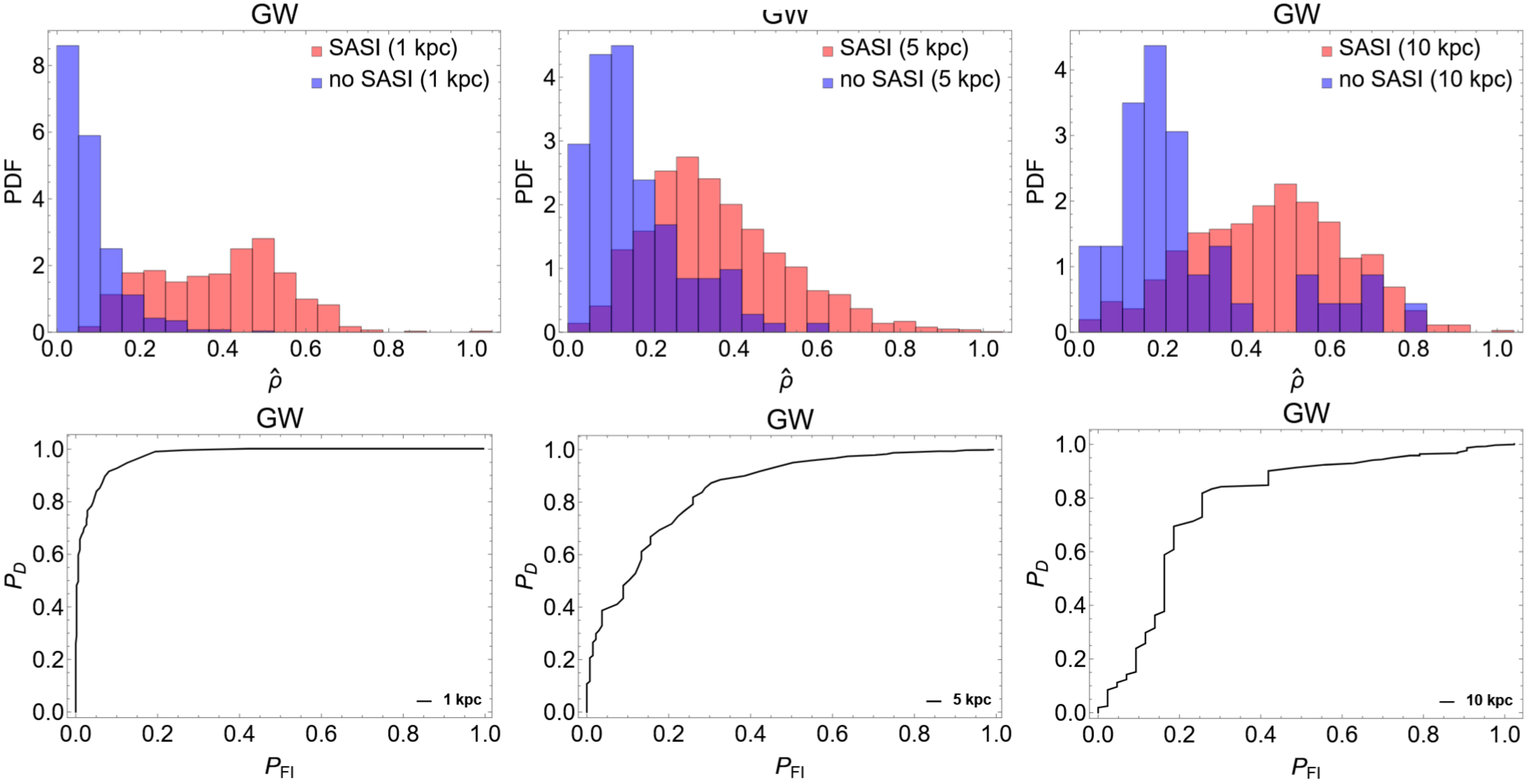

$$f_{GW}^{SASI} = 2 \times 10^2\ \mathrm{Hz}\sqrt{\frac{m_{sh}}{r_{sh}^3}} - 8.5\ \mathrm{Hz}\left(\frac{m_{sh}}{r_{sh}^3}\right). \qquad (2)$$

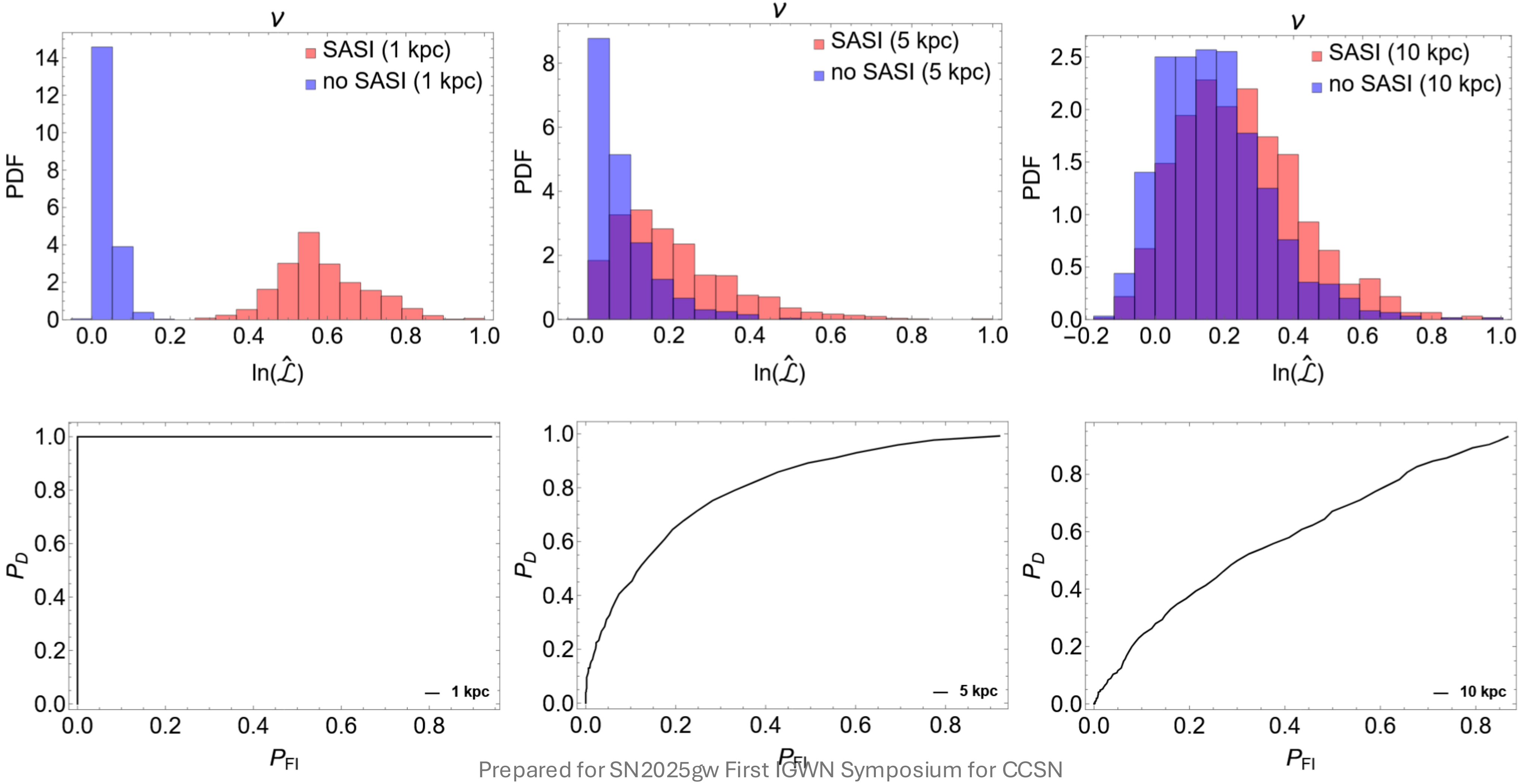

https://journals.aps.org/prd/abstract/10.1103/PhysRevD.107.083017

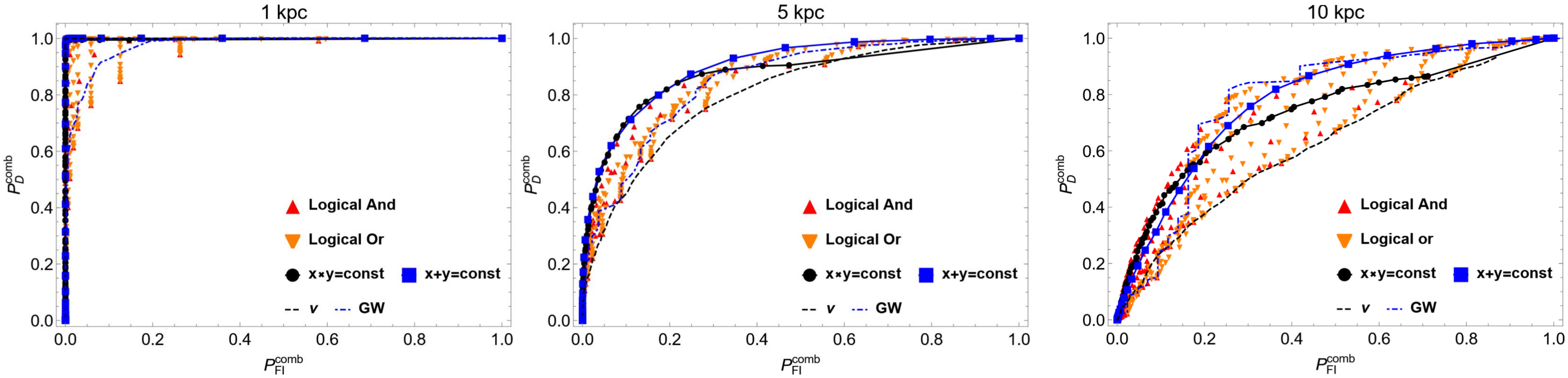

https://journals.aps.org/prd/abstract/10.1103/PhysRevD.107.083017

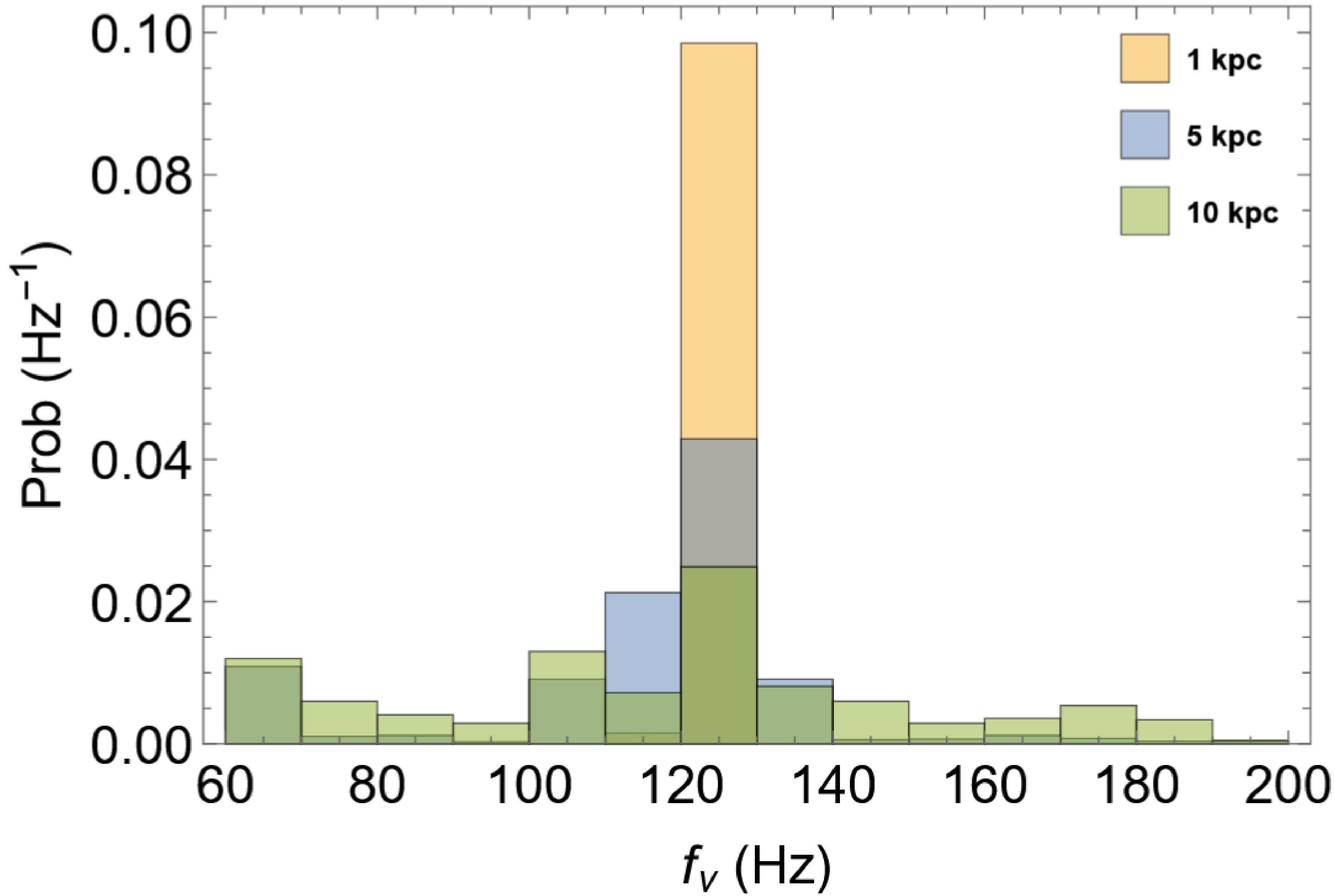

https://journals.aps.org/prd/abstract/10.1103/PhysRevD.107.083017

Parameter Estimation for Rapidly Rotating Core Collapse Supernovae

$$h(t) = h_1(\beta)\exp^{\left[-\frac{(t-\tau)^2}{2\eta^2}\right]} + h_2(\beta)\exp^{\left[-\frac{(t-\tau_a)^2}{2\eta^2}\right]} + h_3(\alpha,\beta)\exp^{\left[-\frac{(t-\tau_b)^2}{2\eta^2}\right]}, \quad (1)$$

$$\begin{aligned} h_1(\beta) &= -13.2 + 2.89\times10^3\beta - 1.31\times10^4\beta^2\,, \quad (2)\\ h_2(\beta) &= -1.03 - 5.52\times10^3\beta + 9.43\times10^3\beta^2\,. \end{aligned}$$

$$h_3(\alpha,\beta) = 17.20 + \alpha\left(\frac{\beta}{0.06}\right)^2, \quad (3)$$

$$\mathrm{FF} = \frac{\langle h_s(f), h_m(f)\rangle}{\sqrt{\langle h_s(f), h_s(f)\rangle\langle h_m(f), h_m(f)\rangle}}, \quad (4)$$

$$\langle \mathrm{u}(f), \mathrm{v}(f)\rangle \equiv 4\,\mathrm{Re}\int_{f_{\mathrm{low}}}^{f_{\mathrm{cut}}} df\,\frac{\mathrm{u}(f)\mathrm{v}(f)^*}{S_h(f)}, \quad (5)$$

$$\frac{\sigma^2}{\beta} = \frac{\sqrt{\sigma_1^2+\sigma_2^2}}{\beta}. \quad (14)$$

https://iopscience.iop.org/article/10.1088/1361-6382/add235

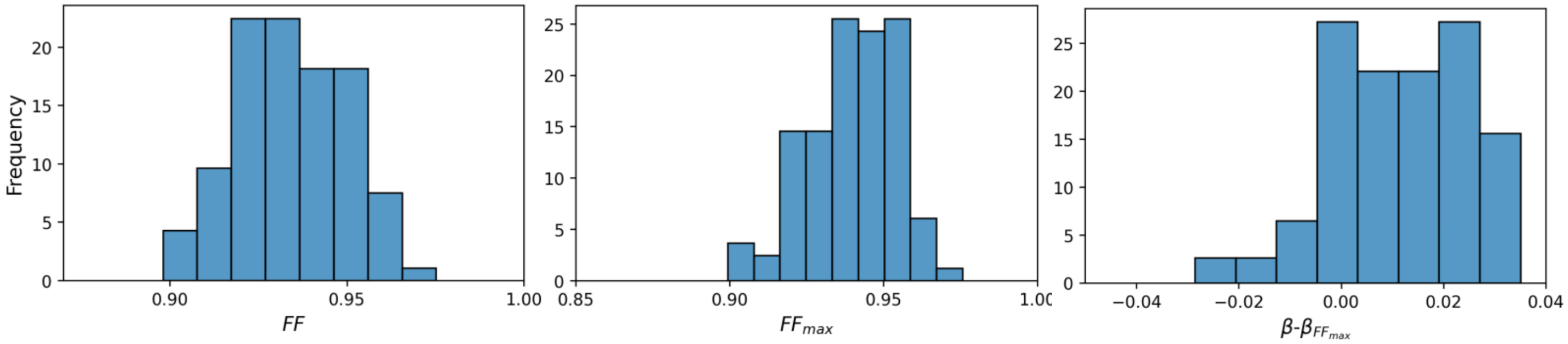

(a) (b) (c)

https://iopscience.iop.org/article/10.1088/1361-6382/add235

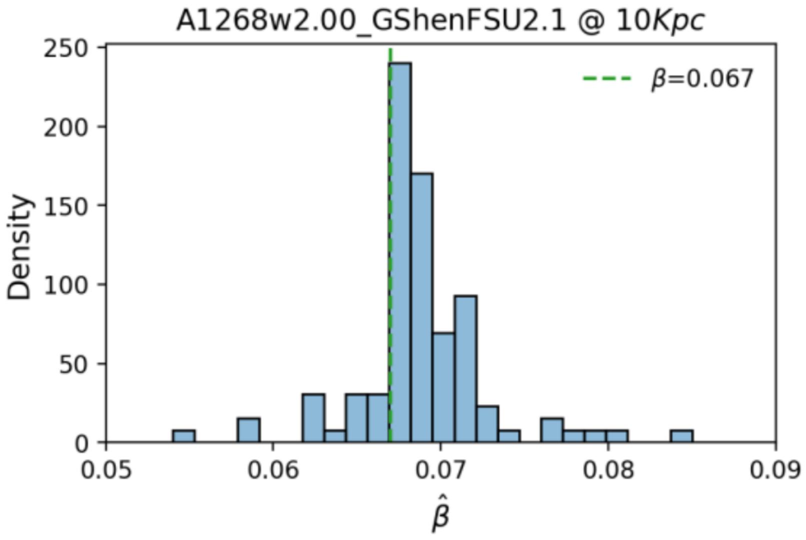

(a)

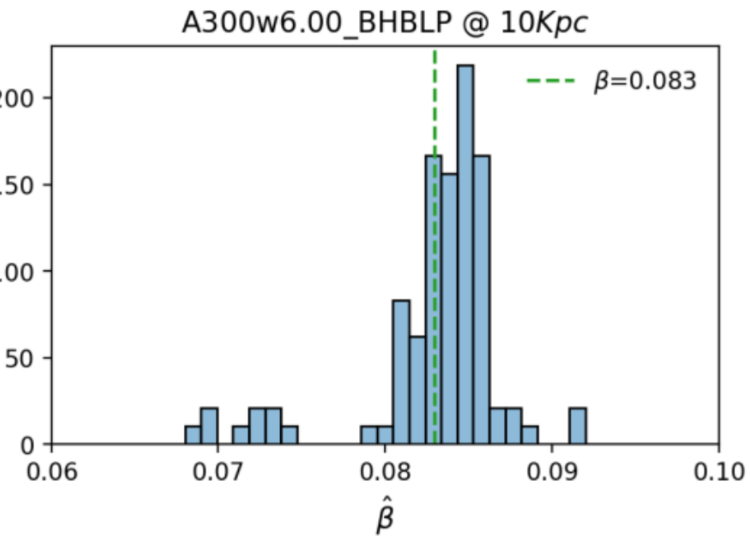

(b)

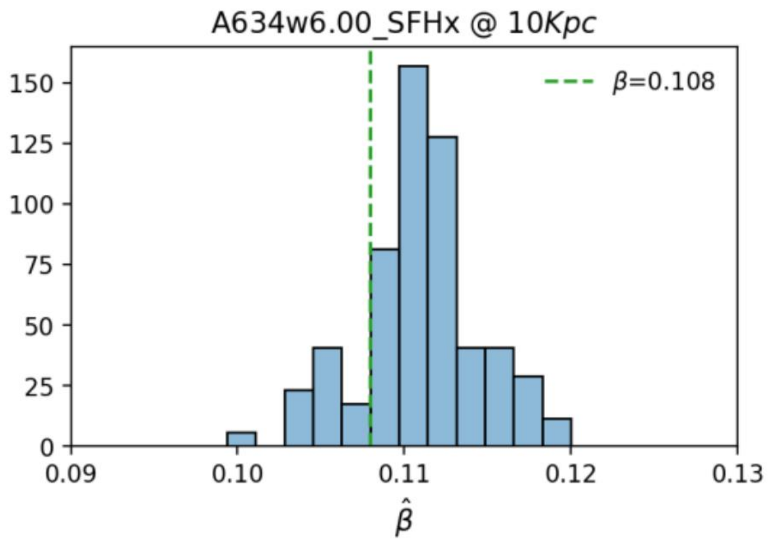

(c)

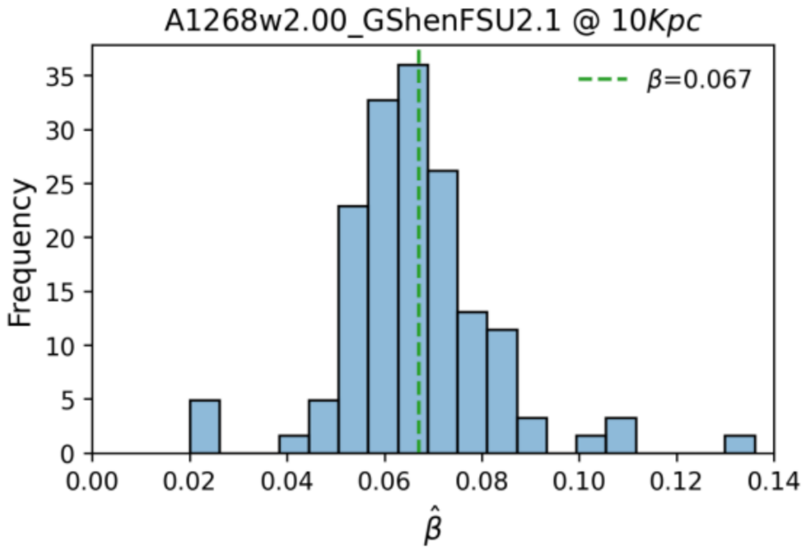

(a)

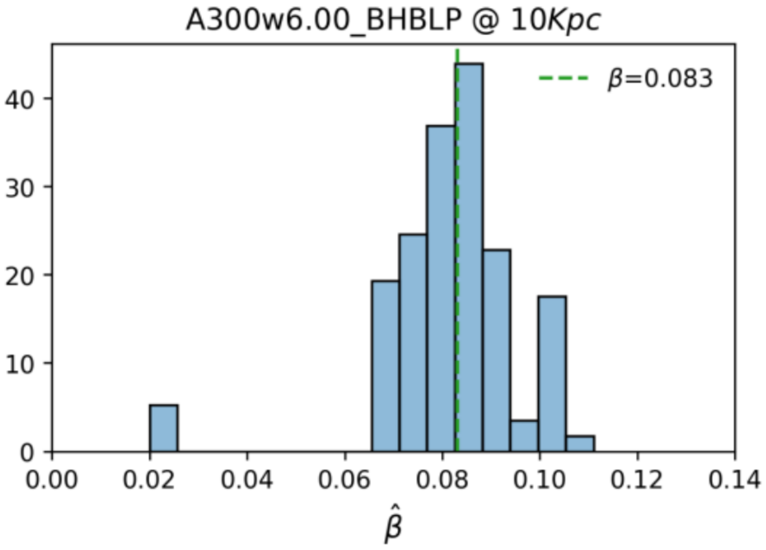

(b)

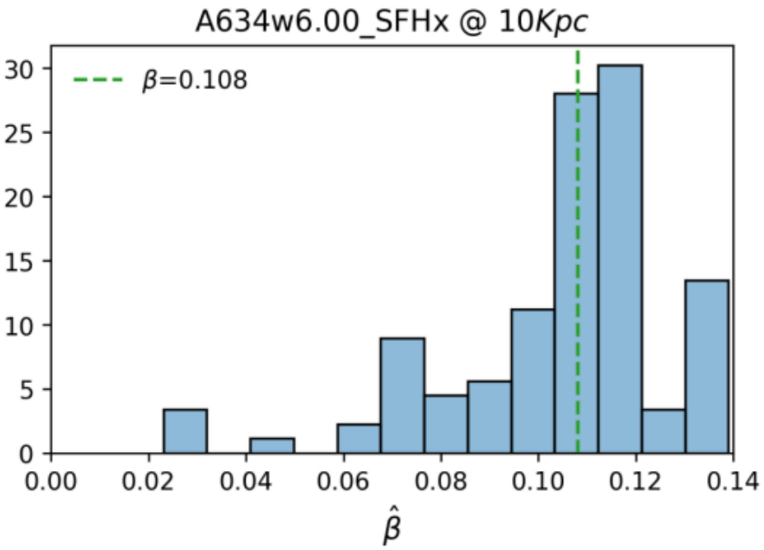

(c)

https://iopscience.iop.org/article/10.1088/1361-6382/add235

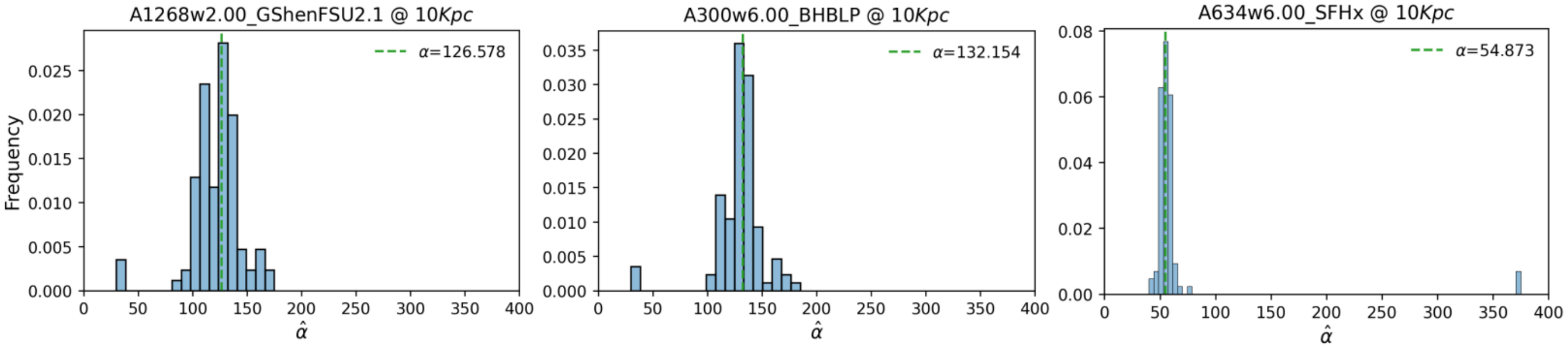

(a) (b) (c)

https://iopscience.iop.org/article/10.1088/1361-6382/add235

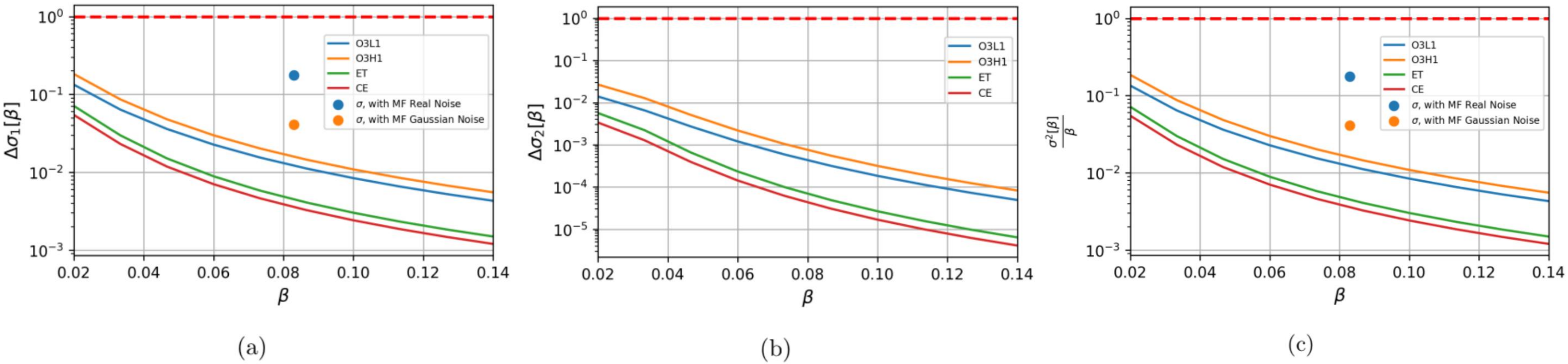

https://iopscience.iop.org/article/10.1088/1361-6382/add235

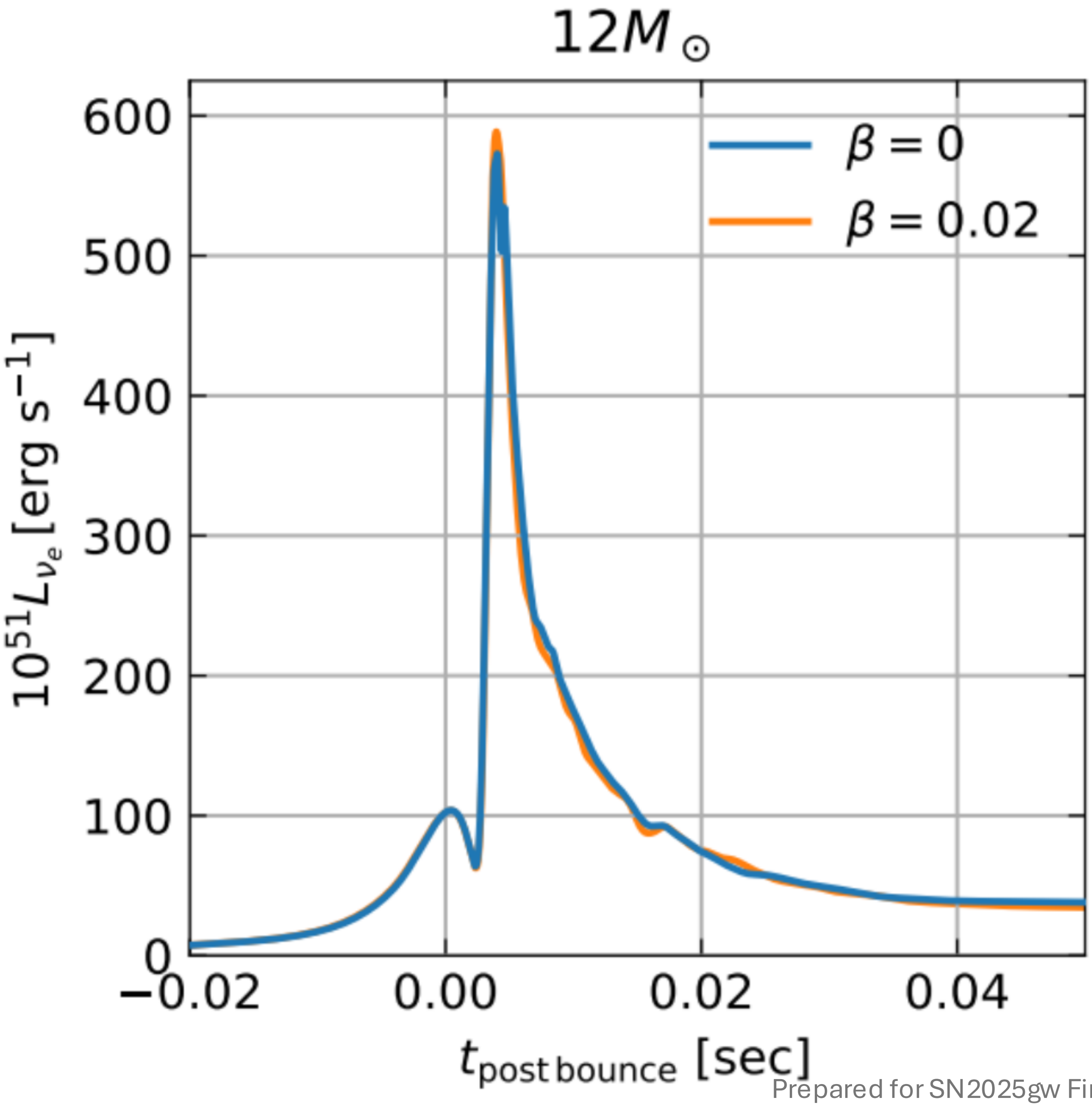

Electron type neutrino luminosity (in the fluid frame) versus time for a nonrotating and rotating axisymmetric model from a 12M⊙ progenitor [117]. These results are from models used in [118], which utilize a robust neutrino treatment—the so called 'M1 scheme' [21]—and a general relativistic effective potential (GREP) [119]. Similar to other models in [118], there is slight dependence of Lve on rotation during the bounce, supported by previous work using a different neutrino treatment [120]. Later in the CCSNe, however, rapid rotation can lower neutrino luminosities.

https://iopscience.iop.org/article/10.1088/1361-6382/add235

Memory

See also Colter Richardson's presentation

Monday 21/07 at 15:00

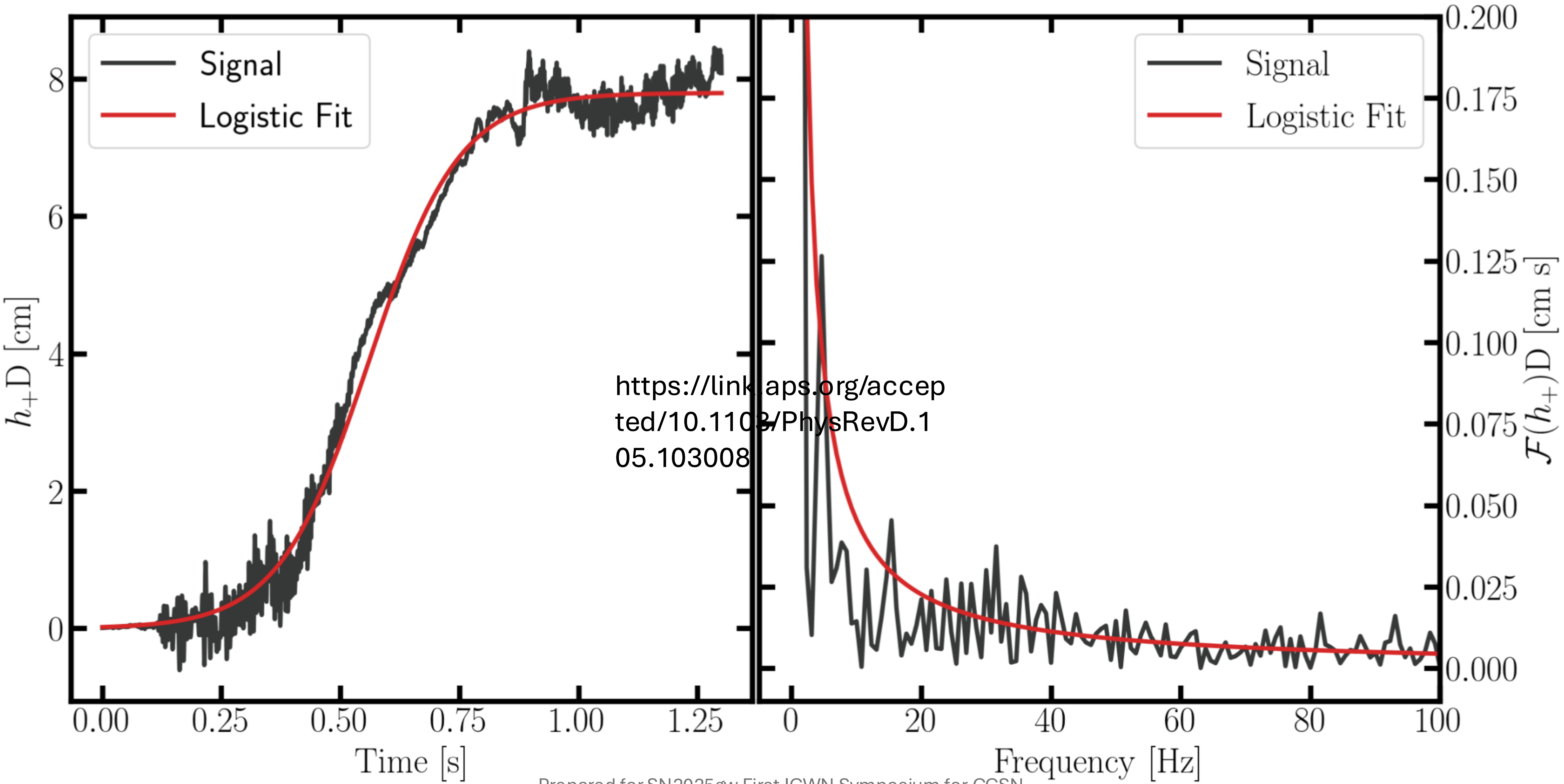

https://link.aps.org/accepted/10.1103/PhysRevD.105.103008

https://link.aps.org/accepted/10.1103/PhysRevD.105.103008

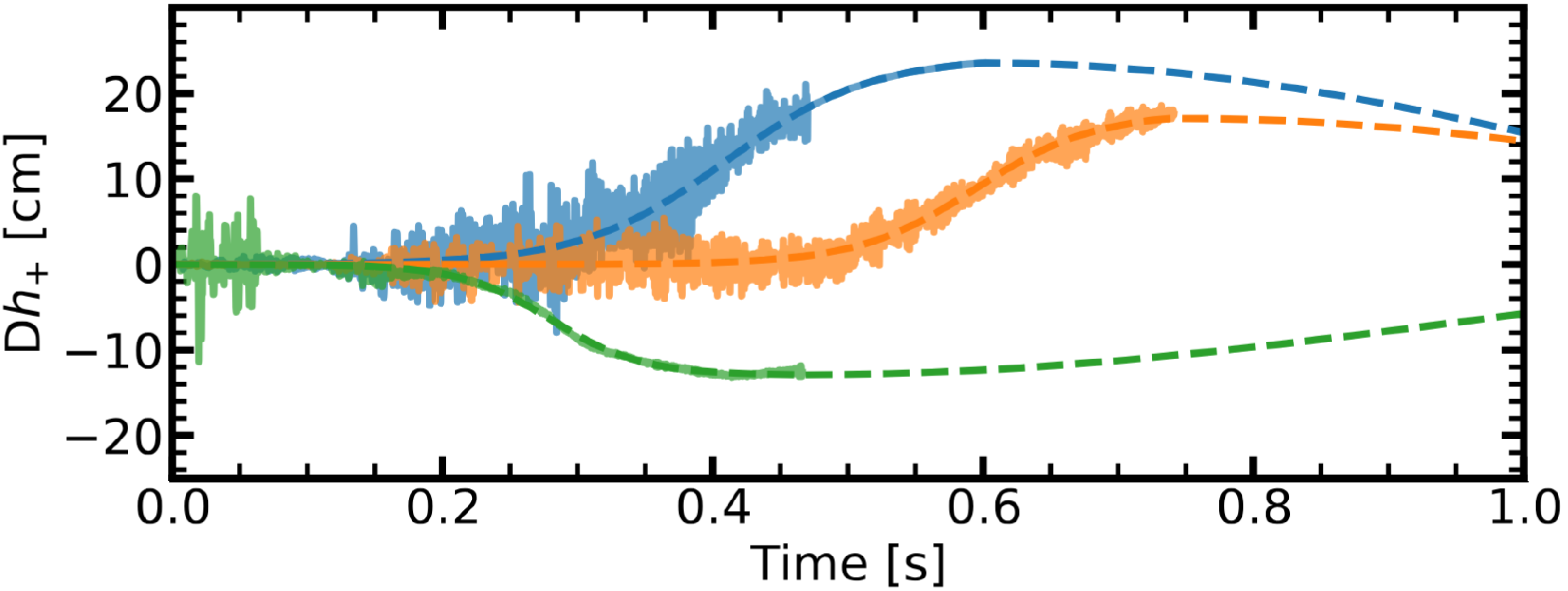

https://arxiv.org/abs/2404.02131

Detection Prospects

- We also investigate how the LPF affects the signal.
- Notice that the signal in the bottom panel is altered slightly at ~10 Hz, but this is not to the same degree as the noise and does not affect our detection results.

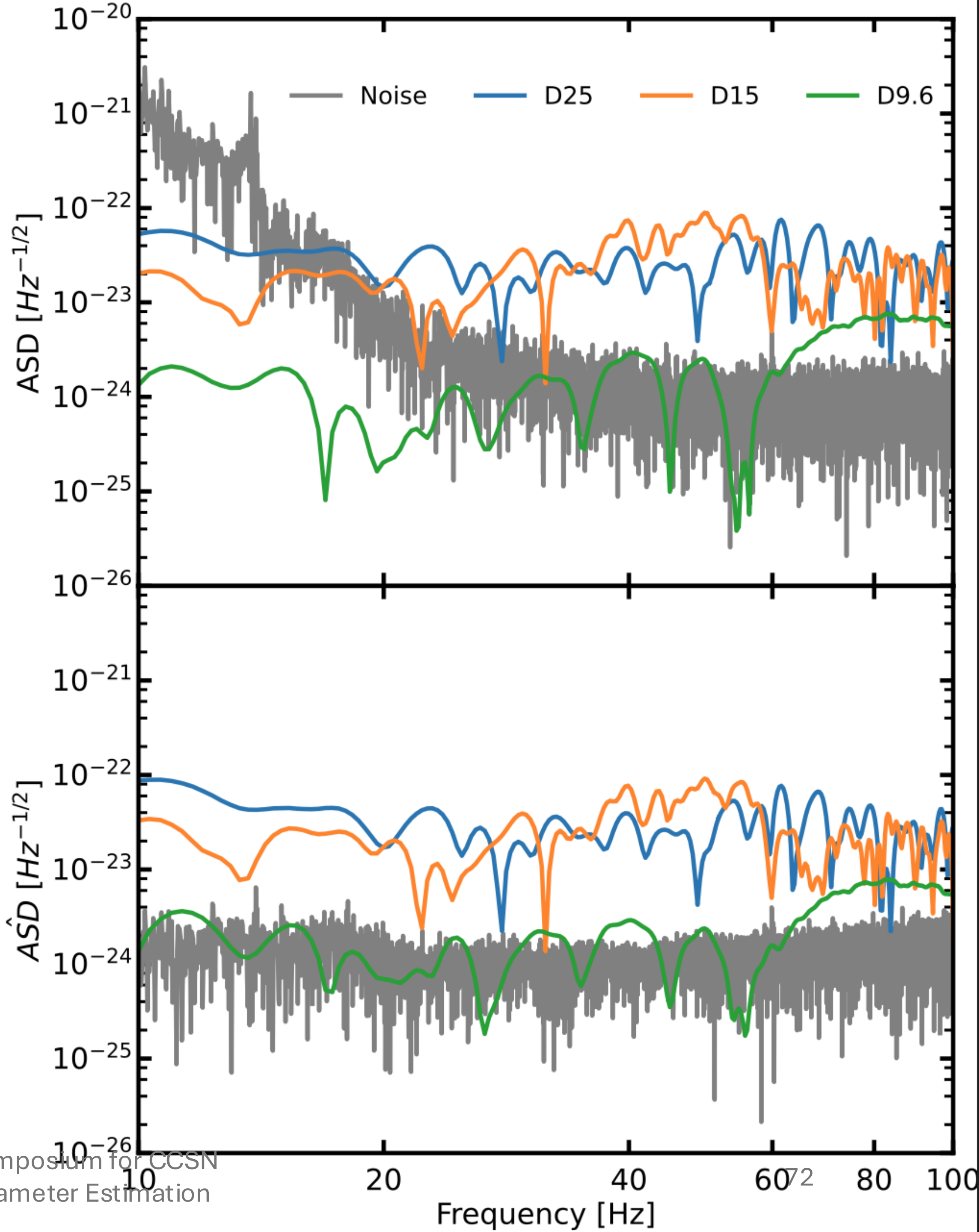

Detection

- We present the correlations for two different noise segments and two different distances.
- For 1 kpc, the D15 and D25 signals are always identifiable, and the D9.6 signal is only identifiable in one segment.
- For 10 kpc the D15 and D25 models are always identifiable (with a glitch present in the D15 case for one segment), and the D9.6 signal is unidentifiable.

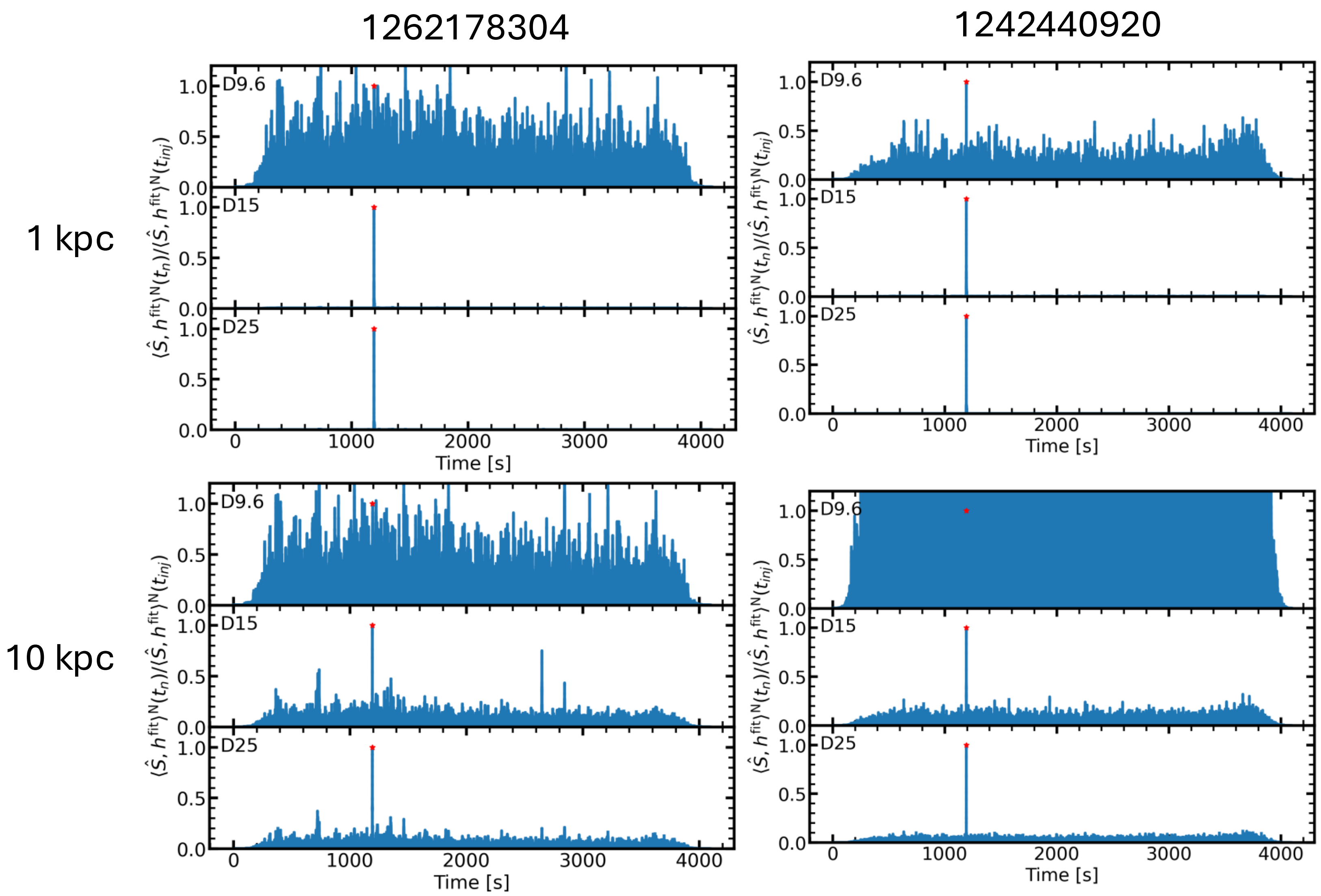

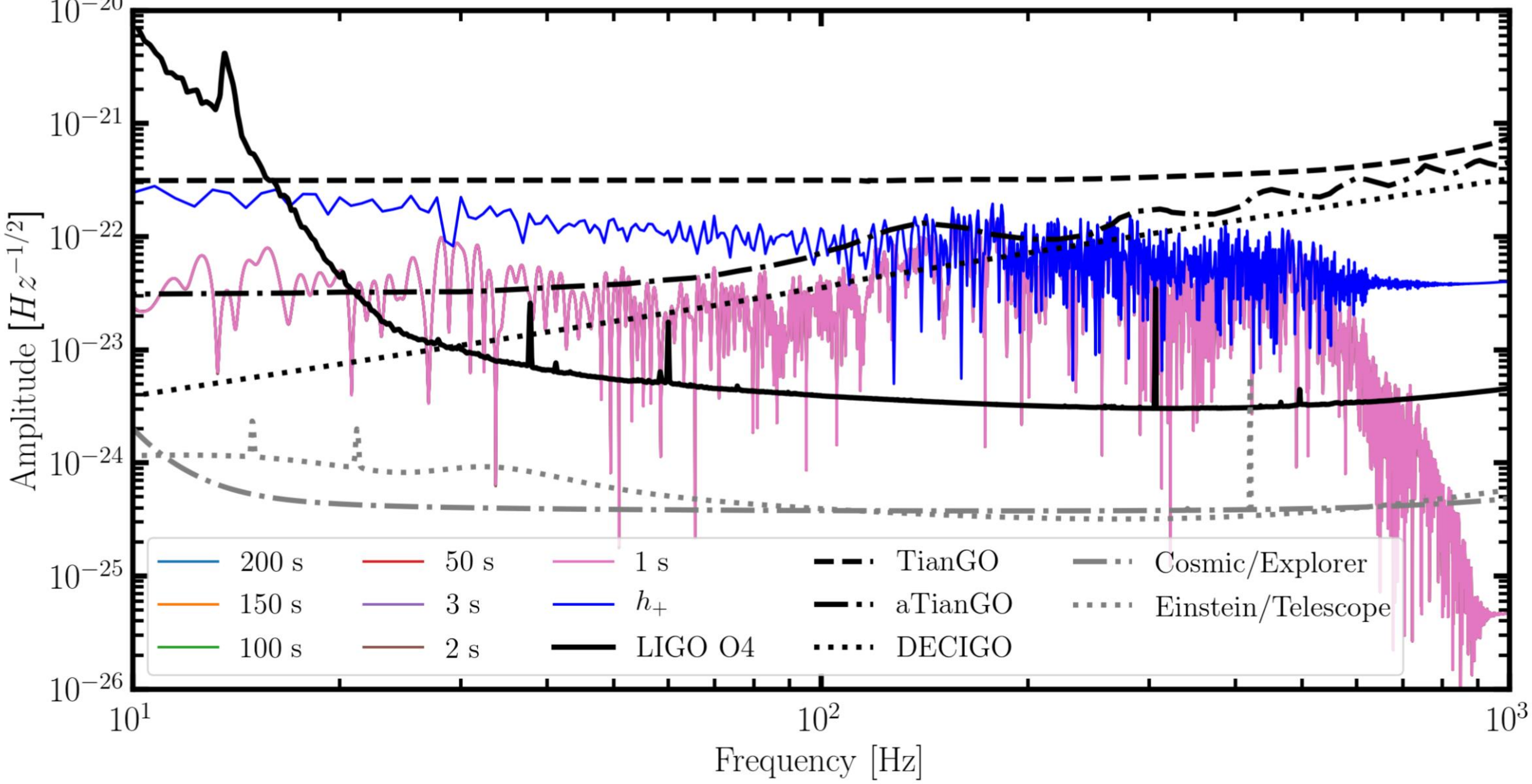

Blue line: the spectral energy density of the plus polarization mode of the GW emission emitted in the direction defined by (θ, φ) = (0o, −180o) without tapering. The black and gray curves show the sensitivity curves of various detectors (as indicated by the label). The source is assumed to be at a distance of 1 kpc. The curves labeled by a specific amount of seconds show the spectral energy density of the signal after a tapering of the specified time duration has been added. This figure shows the curves between 10 and 1000 Hz. Notice that for frequencies > 10 Hz, the signals with the addition of the tails are indistinguishable.

https://link.aps.org/accepted/10.1103/PhysRevD.105.103008

Linear Predictive Filtering

- We train a Linear Predictor Filter on segments of GWOSC noise and then remove the predicted signal.
- This process highlights signals that do not follow the general trends of the trained data.
  - Signals like glitches and our memory signal.
- The filter was trained in both MATLAB (using the lpc function) and in Python (using the *librosa* package) with little to no difference.
- The results presented were trained in MATLAB.

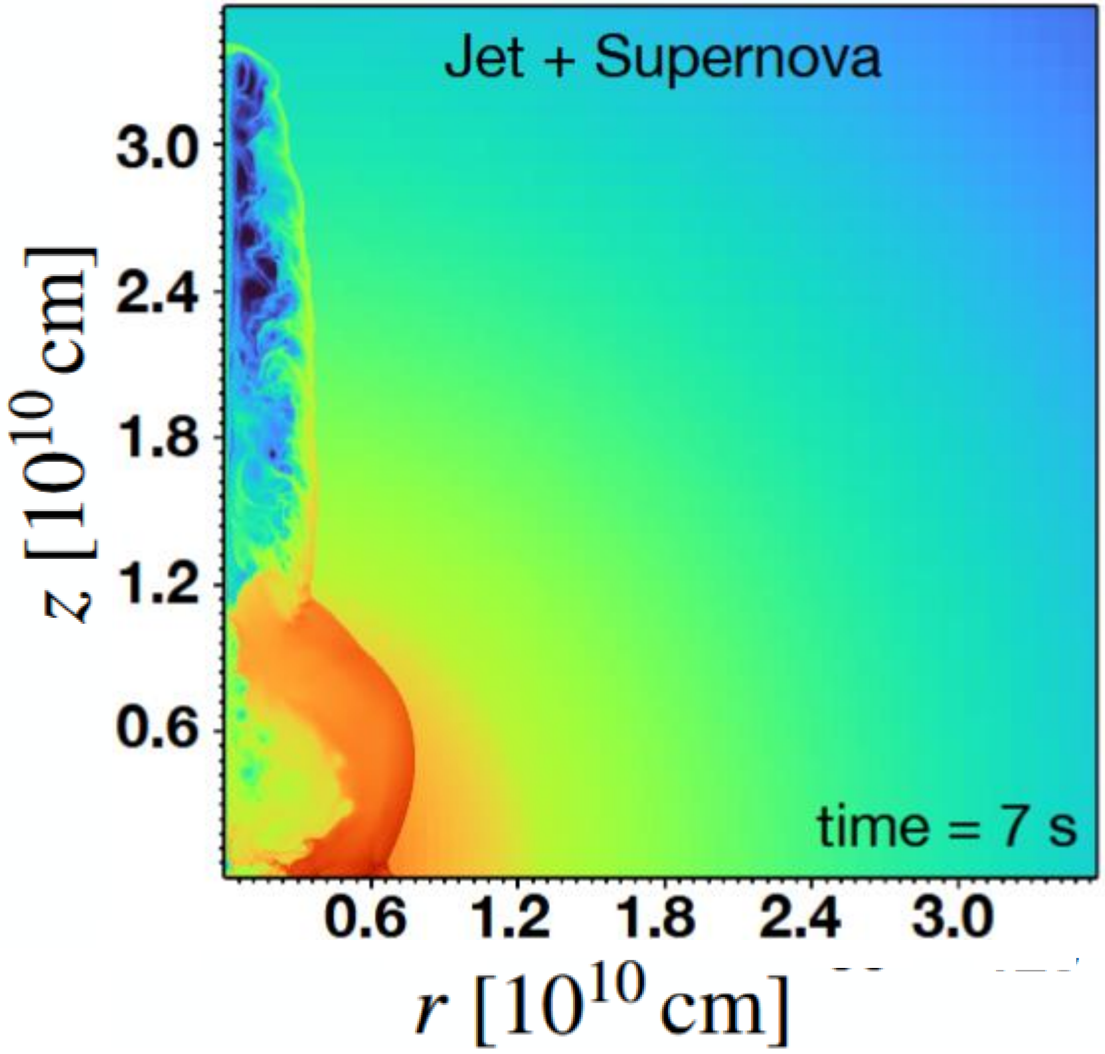

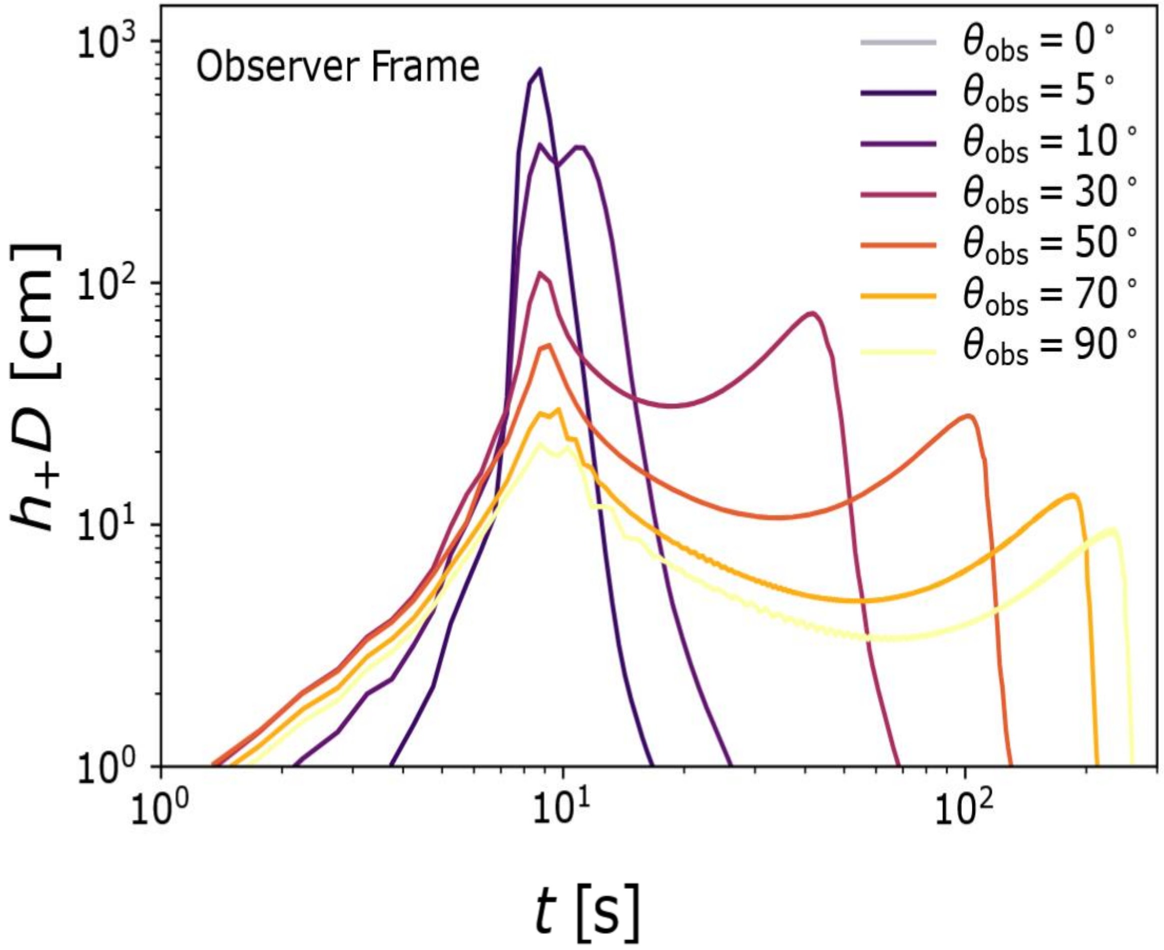

https://academic.oup.com/mnras/article/518/4/5242/6847744

Model Selection

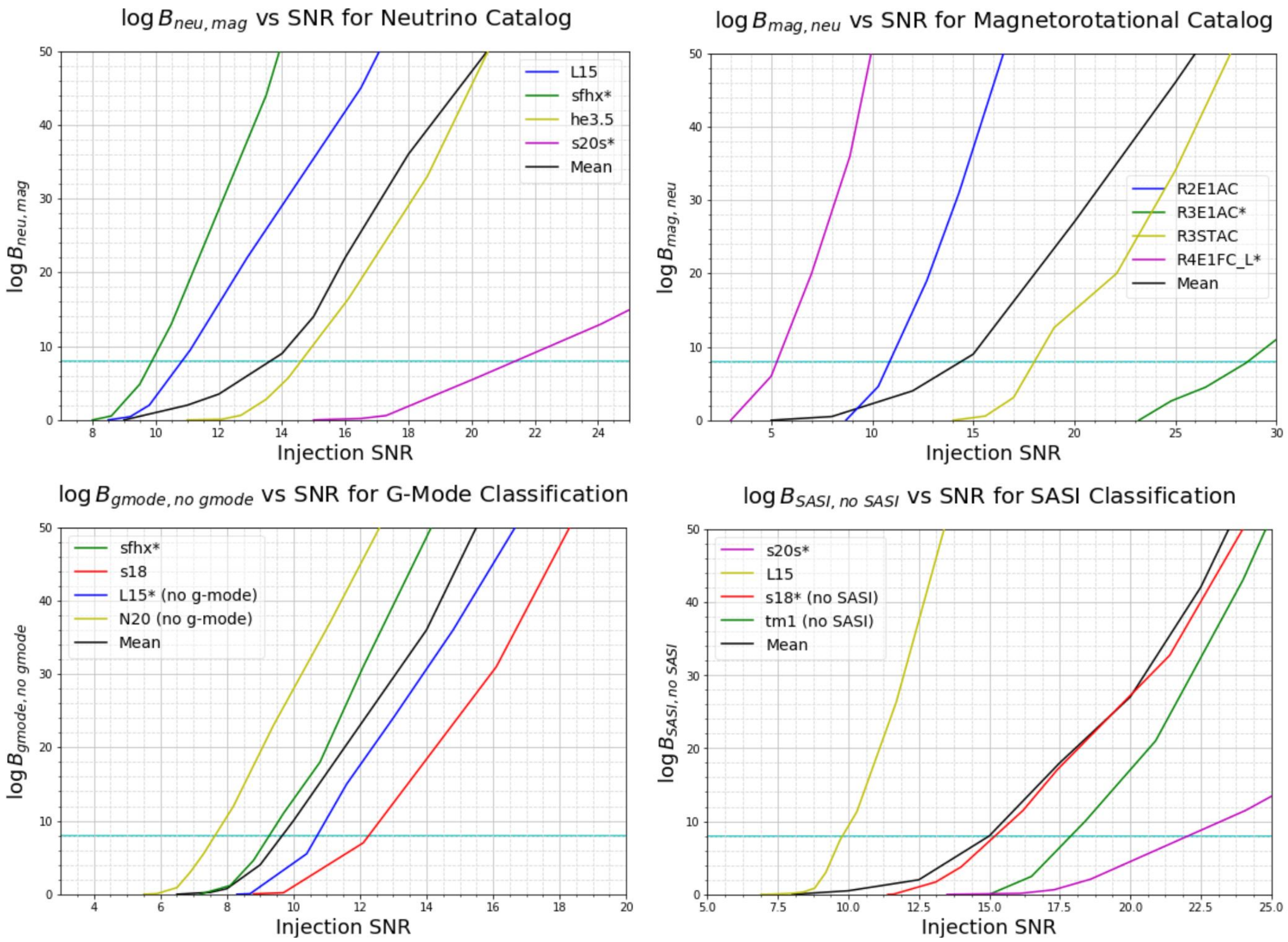

Minimum detectable SNR for each classification statement. All injections performed in a simulated A+ configuration that included AdVirgo and Kagra. The top two plots both pertain to mechanism classification, and the bottom two are for g-modes and SASI. All results are organized such that positive Bayes values correspond to correct classifications regardless of whether the feature is present or not.

https://journals.aps.org/prd/abstract/10.1103/PhysRevD.99.063018

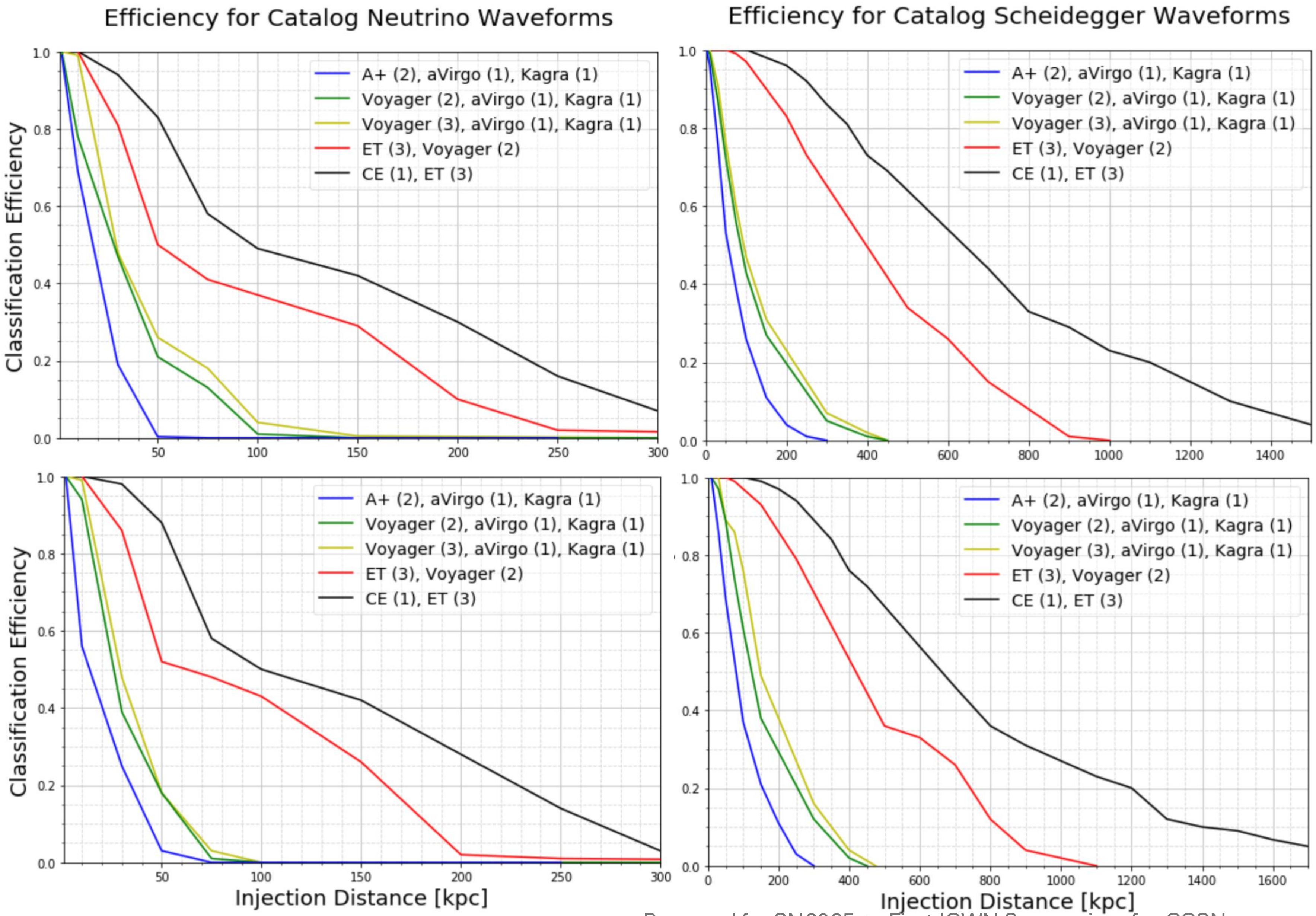

Mechanism classification efficiency. Top plots show results for catalog waveform injections, bottom plots show results for non-catalog injections. Non-catalog injections are considered to be the most realistic test case for a genuine gravitional wave signal from an arbitrary source.

https://journals.aps.org/prd/abstract/10.1103/PhysRevD.99.063018

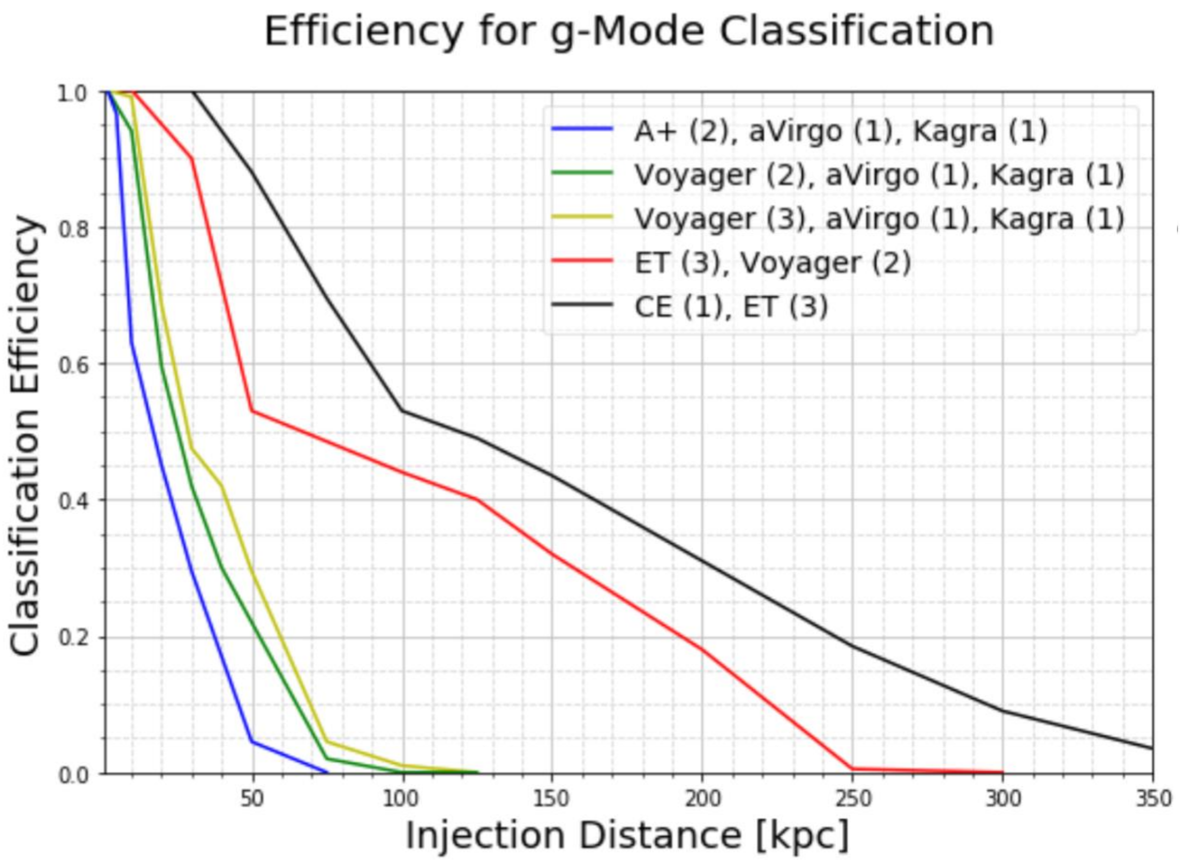

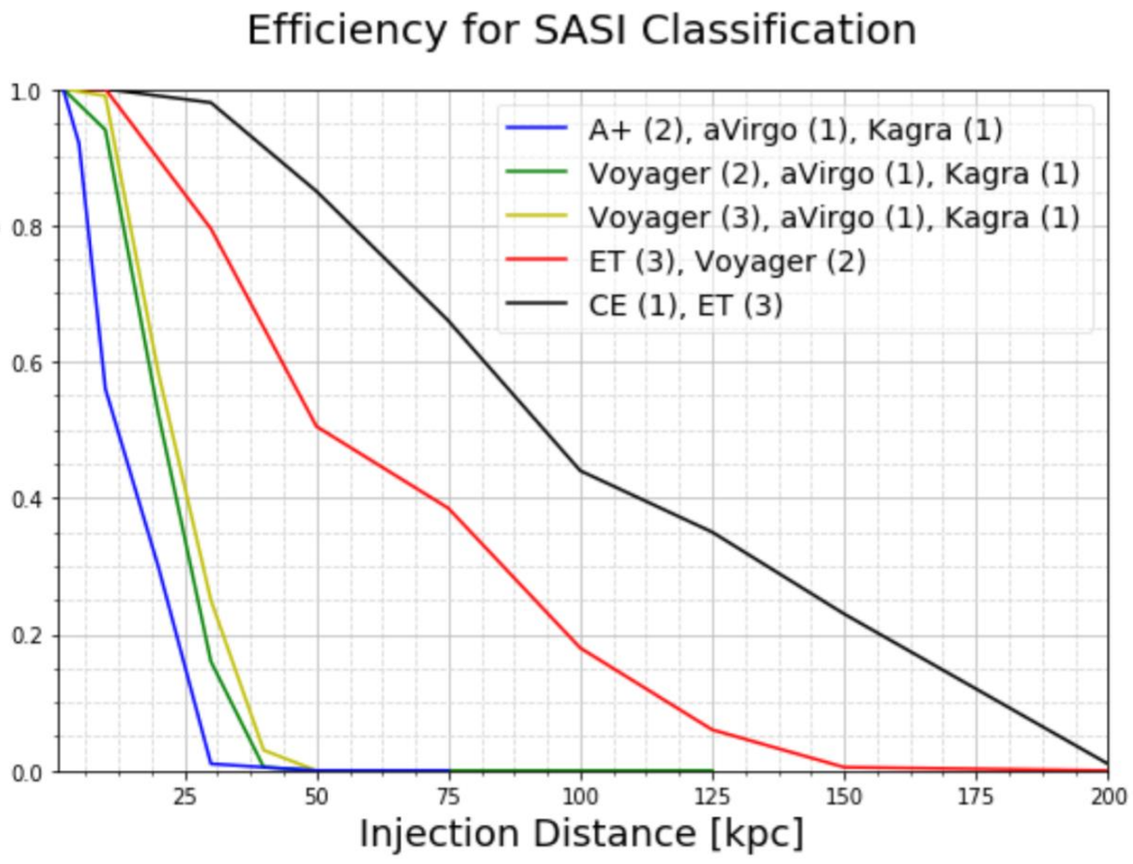

Classification efficiency for g-mode (left) and SASI (right) waveform features. Performance was better for g-mode classification in our tests, but this is also heavily dependent on the energy of the specific waveform. Overall performance was similar to that of neutrino model mechanism classification.

https://journals.aps.org/prd/abstract/10.1103/PhysRevD.99.063018

END

G-mode slope	SASI	10 kpc	5 kpc	1 kpc
	f_ν(Hz)	113.38	111.03	119.85
	δf_ν(Hz)	32.9	22.6	1.22
	a_ν	0.063	0.047	0.044
	δa_ν	0.022	0.013	0.005
	f_{GW}(Hz)	120.08	120.42	122.36
	δf_{GW}(Hz)	18.65	13.80	5.48
	t_0^ν(ms)	N/A (Due to large δf_ν)	> 150	> 150
	τ^ν(ms)	N/A (Due to large δf_ν)	> 50	> 50
	τ^{GW}(ms)	259	494	166
	$\delta\tau^{\mathrm{GW}}$(ms)	347	552	261
$m_{opt}^{GW}(s^{-2})$		2564.84	2645.02	3190.68
$\delta m_{opt}^{GW}(s^{-2})$		1301.08	1132.72	929.62

https://journals.aps.org/prd/abstract/10.1103/PhysRevD.107.083017

$$h_0 = \frac{2}{D}\frac{G}{c^4}\frac{I_{xx} - I_{yy}}{2}(2\pi f_0)^2. \qquad (9)$$

$$h_+(t) = h_0 \frac{1+\cos^2\iota}{2} e^{-t^2/\tau^2} \cos(2\pi f_0 t), \qquad (3)$$

$$h_\times(t) = h_0 \cos\iota \, e^{-t^2/\tau^2} \sin(2\pi f_0 t), \qquad (4)$$

$$h_{ij}^{TT}(t, \mathbf{x}) = \frac{2}{D}\frac{G}{c^4} P_{ij}^{kl} \ddot{I}_{kl}(t - D/c, \mathbf{x}), \qquad (5)$$

$$I_{ij}(t, \mathbf{x}) = \int d^3x \rho \left[x_i x_j - \frac{1}{3}\delta_{ij}(x_1^2 + x_2^2 + x_3^2) \right], \qquad (6)$$

$$h_+ = \frac{1}{2} h_0 (1 + \cos^2\iota) \cos(2\pi f_0 t), \qquad (7)$$

$$h_\times = h_0 \cos\iota \sin(2\pi f_0 t), \qquad (8)$$

$$h_0 = \frac{2}{D}\frac{G}{c^4}\frac{I_{zz}\epsilon}{2}(2\pi f_0)^2, \qquad (10)$$

$$\epsilon \equiv \frac{I_{xx} - I_{yy}}{I_{zz}}. \qquad (11)$$

$$E_{\mathrm{GW}} = \frac{2}{5}\frac{\pi^2 c^3}{G} D^2 f_0^2 h_{\mathrm{rss50}}^2, \qquad (13)$$

https://journals.aps.org/prd/abstract/10.1103/PhysRevD.110.042007

$$I_{zz}\epsilon = \frac{Dc^4}{G(2\pi f_0)^2}\left(\frac{2}{\pi\tau_{\mathrm{rec}}^2}\right)^{1/4} h_{\mathrm{r}ss50}\,, \qquad (15)$$

https://journals.aps.org/prd/abstract/10.1103/PhysRevD.110.042007

Supernova	Type	Host Galaxy	Distance [Mpc]	t_1 [UTC]	t_2 [UTC]	Δt [days]	OSW Method	T_{coinc} [days]
SN 2019ehk	IIb	NGC 4321	16.1	2019 Apr 23.10	2019 Apr 24.50	1.40	2	0.41 (29%)
SN 2019ejj	II	ESO 430-G20	15.7	2019 Apr 23.28	2019 Apr 30.86	7.58	3	1.25 (16%)
SN 2019fcn	II	ESO 430-G20	15.7	2019 May 03.02	2019 May 07.56	4.54	3	2.51 (55%)
SN 2019hsw	II	NGC 2805	28.2	2019 Jun 05.14	2019 Jun 13.14	8.00	1	5.08 (64%)
SN 2020oi	Ic	NGC 4321	16.1	2020 Jan 02.48	2020 Jan 06.18	3.70	2	2.56 (69%)
SN 2020cxd	IIP	NGC 6395	20.9	2020 Feb 16.53	2020 Feb 22.53	6.00	1	4.58 (76%)
SN 2020dpw	IIP	NGC 6952	22.3	2020 Feb 21.08	2020 Feb 25.08	4.00	1	3.06 (77%)
SN 2020fqv	IIb	NGC 4568	17.3	2020 Mar 22.00	2020 Mar 28.00	6.00	1	4.06 (68%)

https://journals.aps.org/prd/abstract/10.1103/PhysRevD.110.042007

Supernova	Class	η_c	FAR [Hz]	FAP
SN 2019ehk	$C2$	5.9	1.4e-5	0.39 (0.86σ)
SN 2019ejj	$C2$	6.7	1.1e-5	0.45 (0.76σ)
SN 2019fcn	$C2$	6.7	1.4e-5	0.95 (0.06σ)
SN 2019hsw	$C1$	5.6	4.5e-6	0.86 (0.17σ)
SN 2020oi	$C1$	5.8	2.0e-6	0.35 (0.93σ)
SN 2020cxd	$C1$	6.7	3.3e-6	0.73 (0.34σ)
SN 2020dpw	$C2$	6.2	6.3e-6	0.81 (0.23σ)
SN 2020fqv	$C1$	7.6	1.5e-8	0.005 (2.78σ)

https://journals.aps.org/prd/abstract/10.1103/PhysRevD.110.042007

Waveform Models		Distance [kpc]
Non-rotating models	Kur+16 s15	**6.9**
	Mez+23 D15	2.9
	Oco+18 m20p	1.0
	Pow+19 s18	5.5
	Pow+19 he3.5	2.8
	Rad+19 s13	0.6
	Rad+19 s25	5.8
	Pan+21 NR	6.6
Rotating models	And+19 s15fr	1.8
	Obe+20 Signal_O	13.4
	Pan+21 SR	18.2
	Pow+20 m39	19.6
	Pow+23 B12	**29.9**
Phase transition model	Kur+22 s50	8.9*

Distance of the 90% detection efficiency reached with CCSN waveform models for a FAR of 1 event in 10 years. Values in bold represent the farthest distance reached for each family of models. For the 2D Kur+22 s50 model, detection efficiency remains lower than 90% whatever the distance because there is only one polarization. We report the 50% detection efficiency instead that is marked with *.

https://iopscience.iop.org/article/10.3847/1538-4357/adc681

Waveform	Network	Area at 0.1/0.5/0.9 (deg^2)
m15nr	LHVK	0.6/29.6/2050.7
SFHx	LHVK	2.0/97.9/1289.3
C15-3D	LHVK	0.5/43.4/23727.8
mesa20	LHVK	0.7/33.8/8294.6
SR	LHVK	4.1/100.5/2582.5
s13	LHVKAN	0.2/1.0/22.5
s13	LHVKA	0.4/6.0/209.0
s13	LHVK	0.8/27.8/348.4
s13	LHV	1.1/39.8/338.1
s13	LHV	10.5/81.6/445.0
s13	VKA	0.8/31.2/1827.9
A467w0.50_SFHx	LHVK	1.3/50.9/477.7

Detector	SNR		Distance [Mpc]		Rate [yr^{-1}]		
	$5°$	$70°$	$5°$	$70°$	$0° - 10°$	$10° - 40°$	$40° - 90°$
LIGO O4	3.8×10^{-3}	1.3×10^{-2}	1.5×10^{-2}	5.1×10^{-2}	1.5×10^{-12}	1.9×10^{-10}	4.2×10^{-10}
VIRGO O4	2.0×10^{-3}	5.5×10^{-3}	2.2×10^{-2}	2.2×10^{-2}	7.3×10^{-13}	1.8×10^{-11}	3.6×10^{-11}
KAGRA	8.9×10^{-3}	2.8×10^{-3}	7.3×10^{-3}	2.3×10^{-2}	1.6×10^{-14}	2.1×10^{-12}	5.0×10^{-12}
Einstein Telescope	4.4×10^{-2}	6.2×10^{-2}	3.5×10^{-1}	5.0×10^{-1}	3.9×10^{-10}	2.3×10^{-8}	5.3×10^{-8}
Cosmic Explorer	3.8×10^{-2}	6.7×10^{-2}	3.0×10^{-1}	5.3×10^{-1}	3.4×10^{-10}	2.8×10^{-8}	6.4×10^{-8}
eLISA	2.1×10^{-2}	3.9×10^{-3}	8.5×10^{-2}	1.5×10^{-2}	5.5×10^{-11}	3.7×10^{-10}	4.0×10^{-11}
ALIA	1.6	9.3×10^{-2}	6.4	3.7×10^{-1}	1.3×10^{-5}	1.2×10^{-5}	4.5×10^{-7}
DECIGO	1.5×10^{2}	4.7	6.0×10^{2}	1.8×10^{1}	7.5	2.2	1.0×10^{-1}
BBO	1.5×10^{2}	5.4	6.0×10^{2}	2.1×10^{1}	7.9	2.5	1.2×10^{-1}

https://academic.oup.com/mnras/article/518/4/5242/6847744

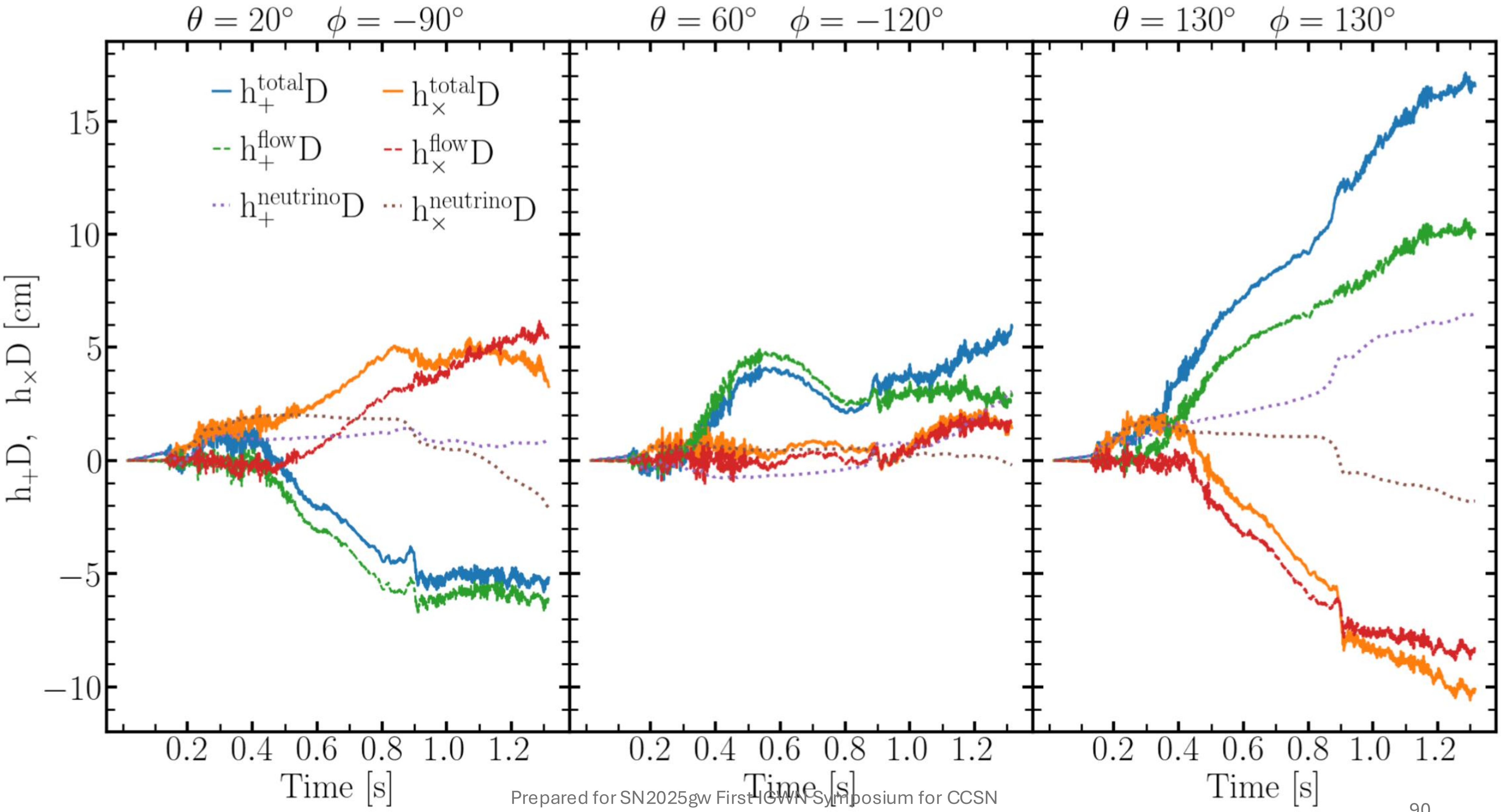

https://link.aps.org/accepted/10.1103/PhysRevD.105.103008

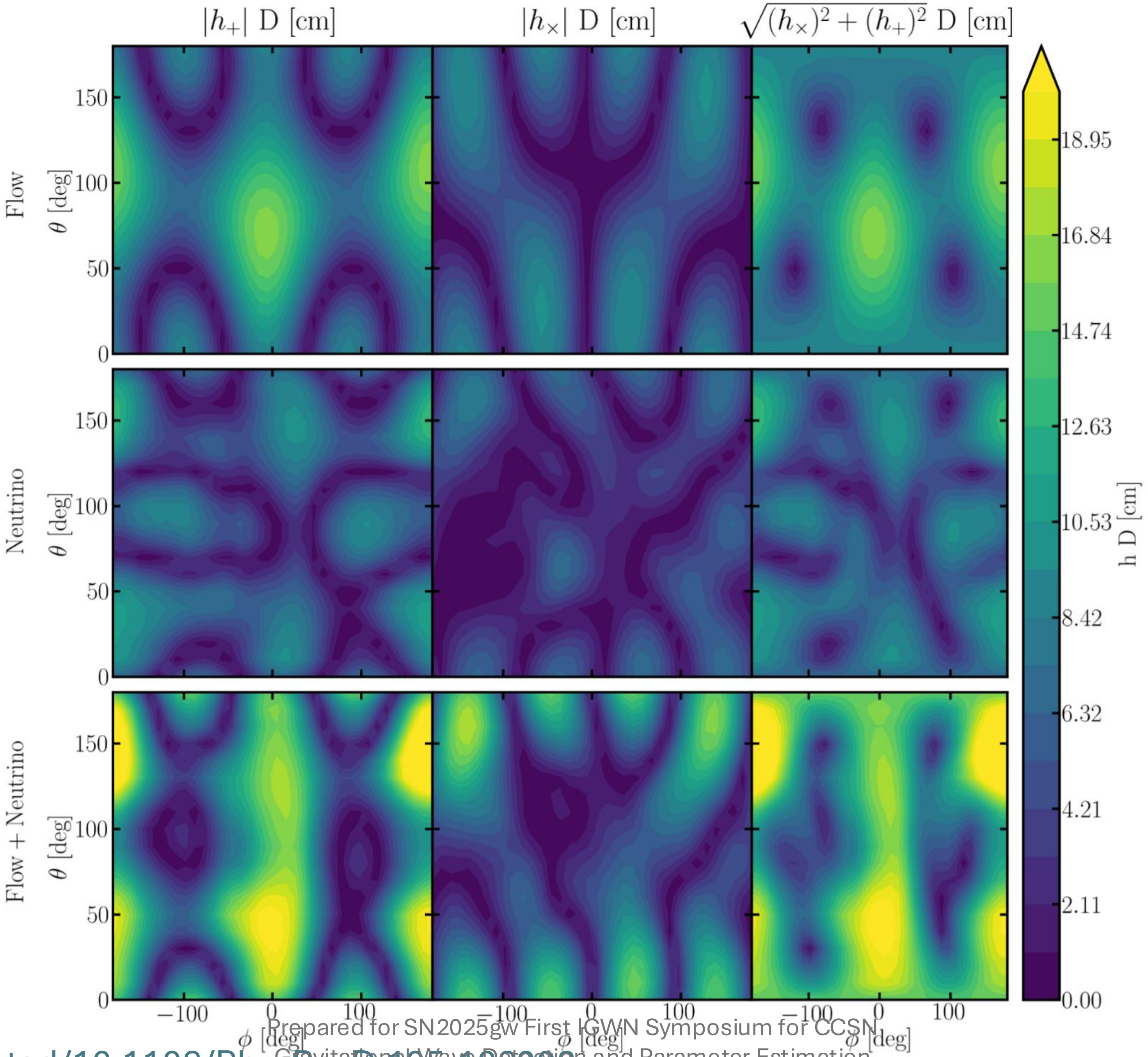

https://link.aps.org/accepted/10.1103/PhysRevD.105.103008

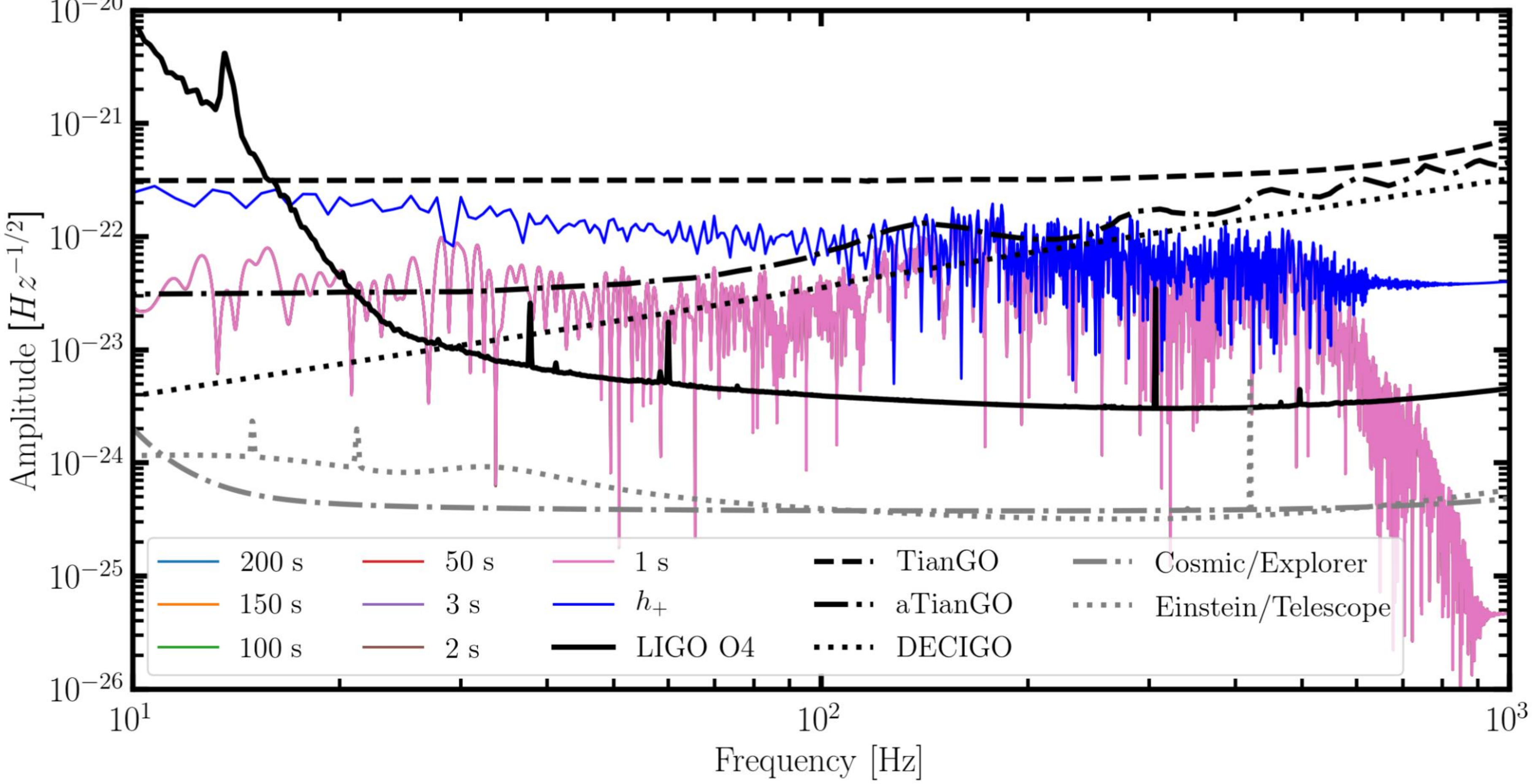

Blue line: the spectral energy density of the plus polarization mode of the GW emission emitted in the direction defined by (θ, φ) = (0o, −180o) without tapering. The black and gray curves show the sensitivity curves of various detectors (as indicated by the label). The source is assumed to be at a distance of 1 kpc. The curves labeled by a specific amount of seconds show the spectral energy density of the signal after a tapering of the specified time duration has been added. This figure shows the curves between 10 and 1000 Hz. Notice that for frequencies > 10 Hz, the signals with the addition of the tails are indistinguishable.

https://link.aps.org/accepted/10.1103/PhysRevD.105.103008

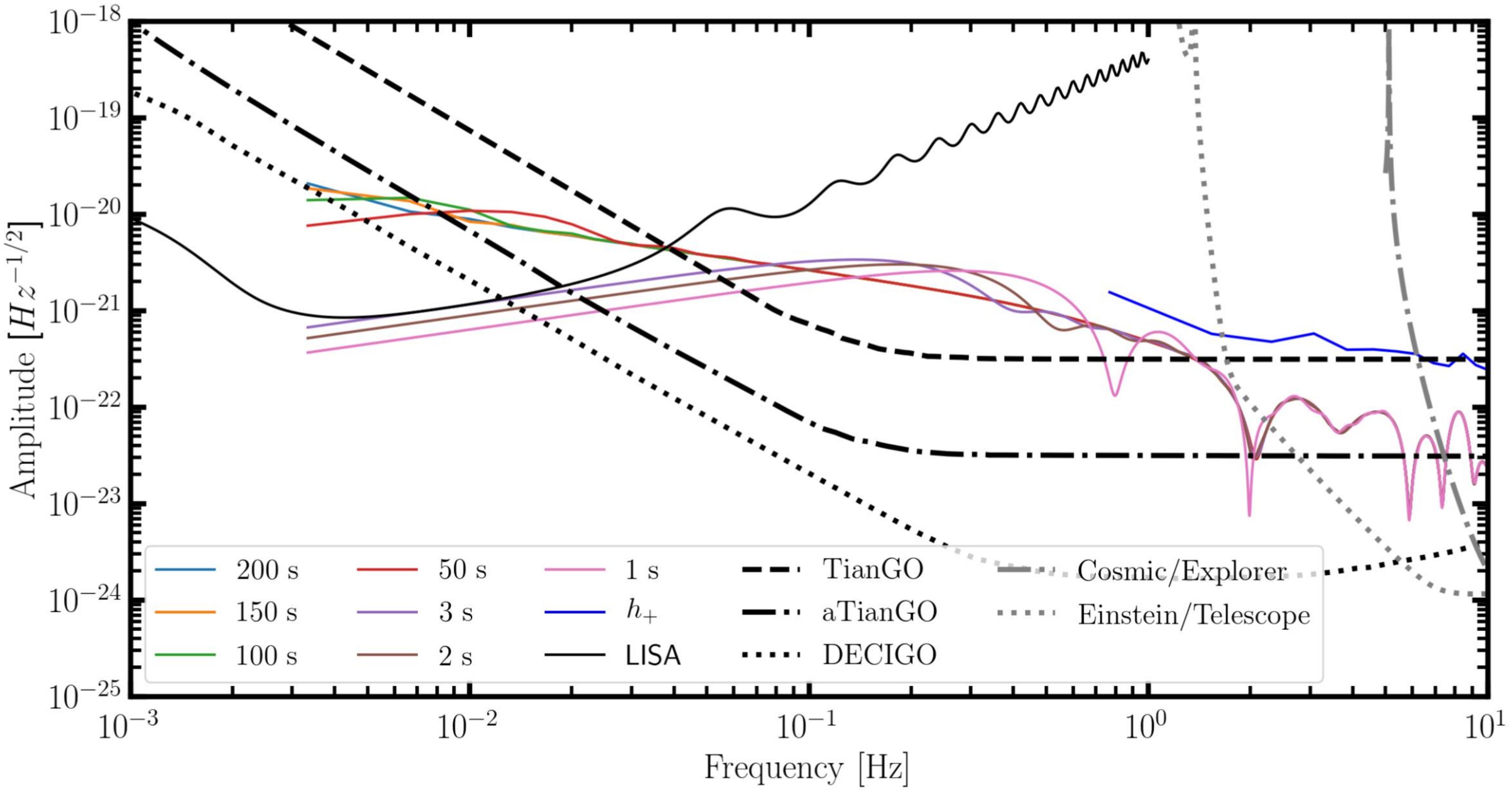

Blue line: the spectral energy density of the plus polarization mode of the GW emission emitted in the direction defined by (θ, φ) = (0o, −180o) without tapering. The black and gray curves show the sensitivity curves of various detectors (as indicated by the label). The source is assumed to be at a distance of 1 kpc. The curves labeled by a specific amount of seconds show the spectral energy density of the signal after a tapering of the specified time duration has been added. This figure shows the curves below 10 Hz.

https://link.aps.org/accepted/10.1103/PhysRevD.105.103008

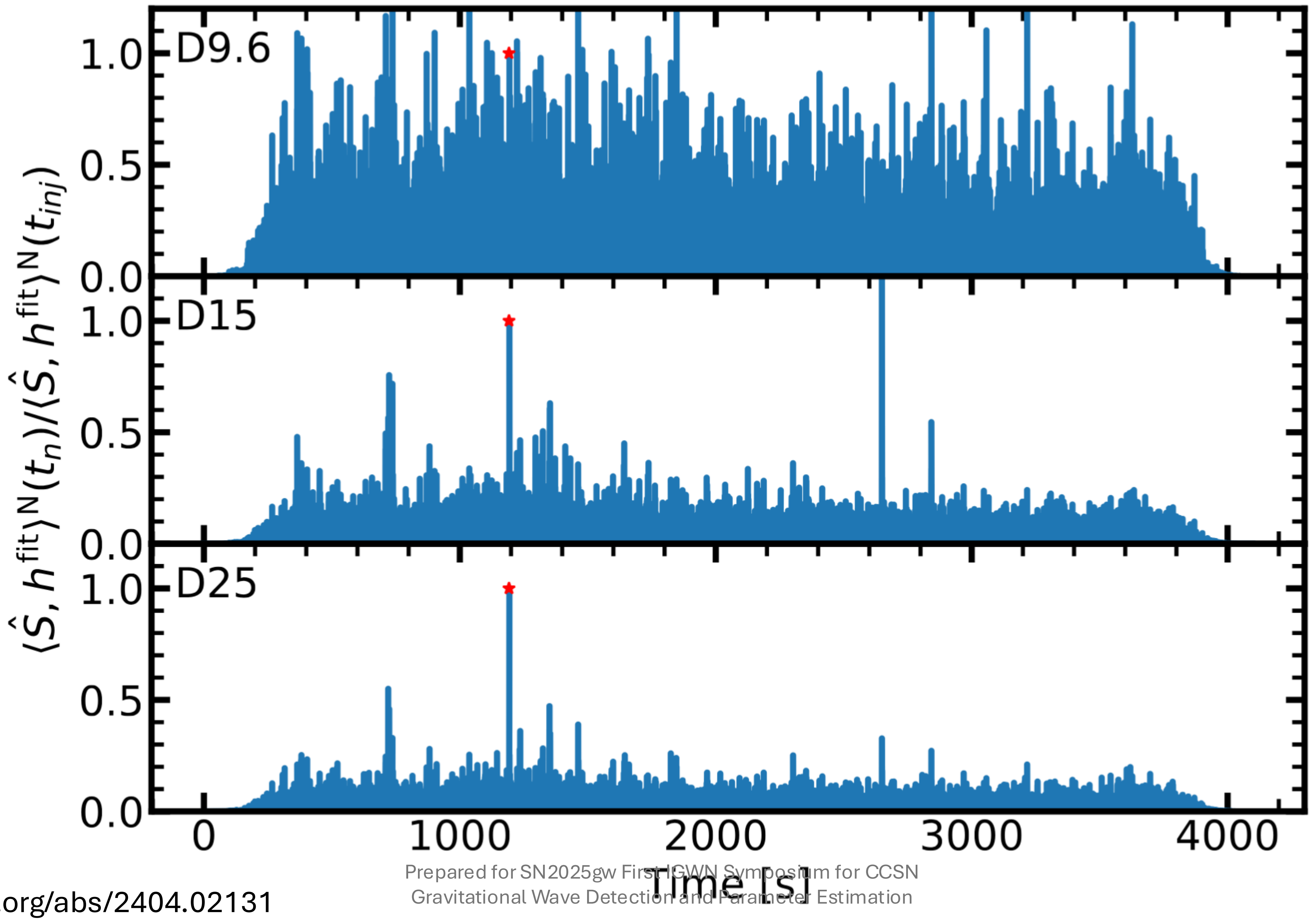

https://arxiv.org/abs/2404.02131

LPF Continued

- We train 16384 parameters for this study (to better predict the noise to $\mathcal{O}(1)$ seconds).
- However, a more complete study of the LPF with different parameter choices is necessary.
- Notice that in the 16384 trained parameter case, the 500 Hz Peak disappears, but in the 8 trained parameter case, the noise floor drops across the CCSN frequency band.

16384 Trained Parameters

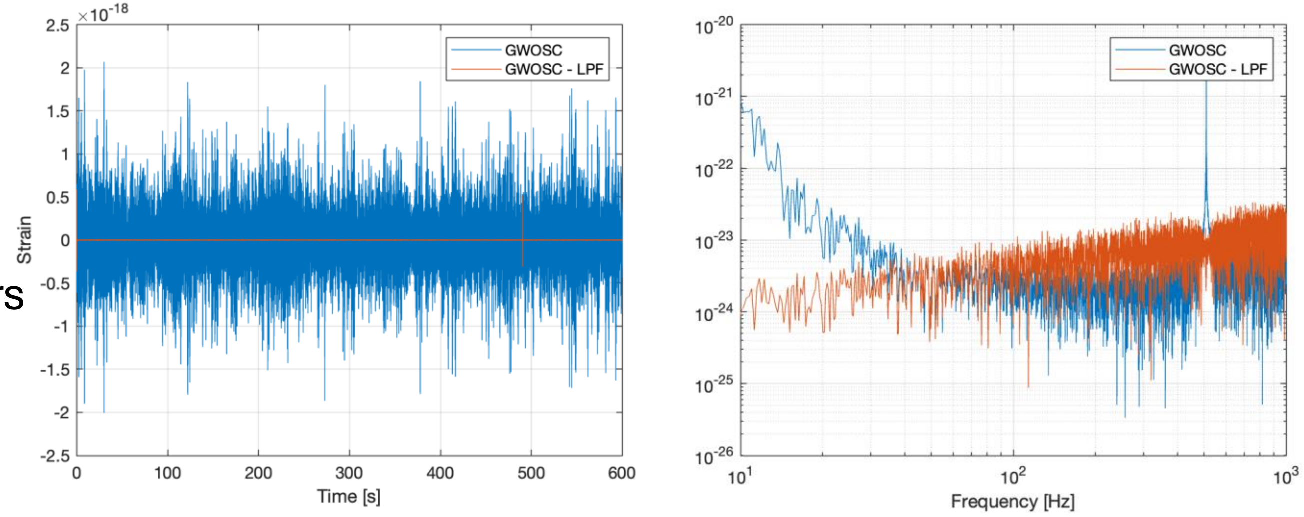

8 Trained Parameters

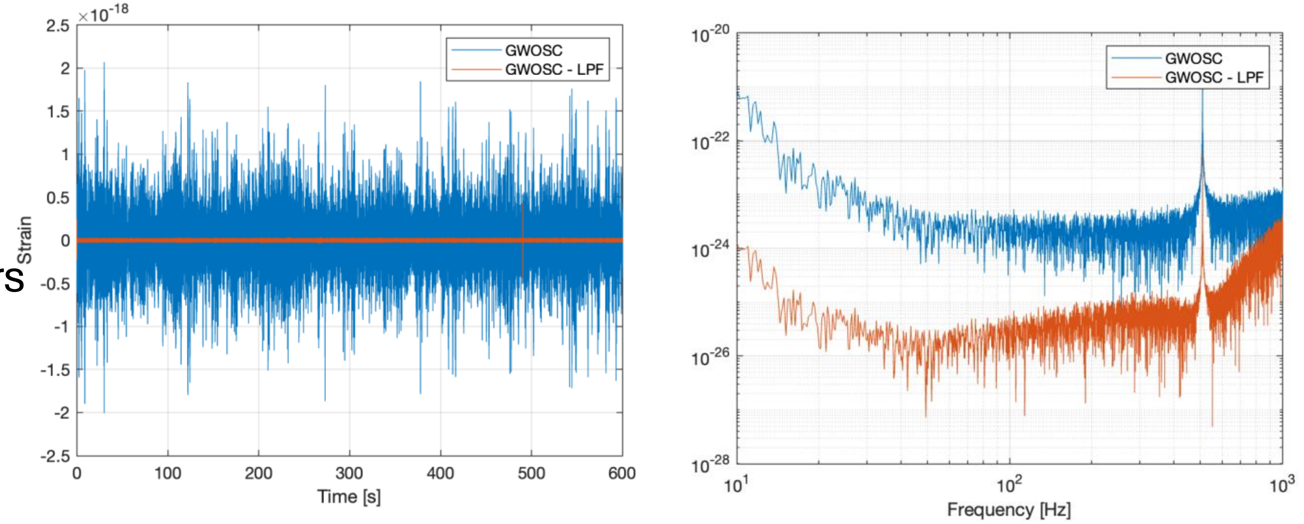

Detection Procedure

- We start with *Noise* from *GWOSC* and a *Signal* from *Simulation*.
- We then train the *LPF* coefficients on the *Noise* sample and *Fit* our *Signal* to our template.
  - In a true parameter search the parameters of the template are determined after the detection is made, but to simplify this proof of concept, we perform the correlation with the exact fit.
  - However, we have checked that for the parameter space near the “true” values, the parameters pertaining to the “true” fit are the maximum.
- Then the *Signal* is injected into the *Noise* to form the *Data*.
- The *LPF* is then removed from the *Data*.
- A high pass filter is applied to the *Data*.
- The *Fit* is correlated with the *Data* to pick out our *Signal*.

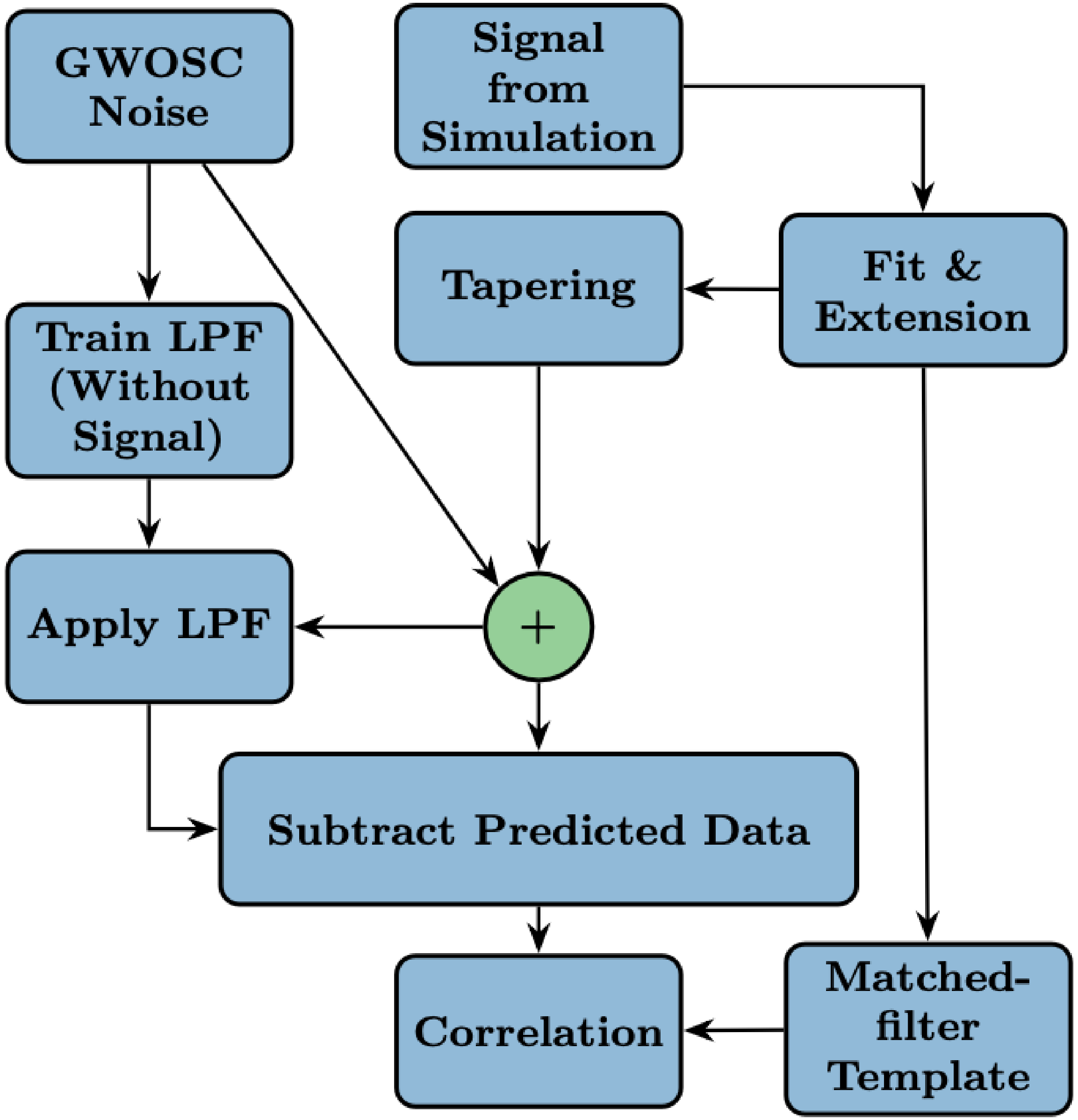

Detection Prospects

- We also investigate how the LPF affects the signal.
- Notice that the signal in the bottom panel is altered slightly at ~10 Hz, but this is not to the same degree as the noise and does not affect our detection results.

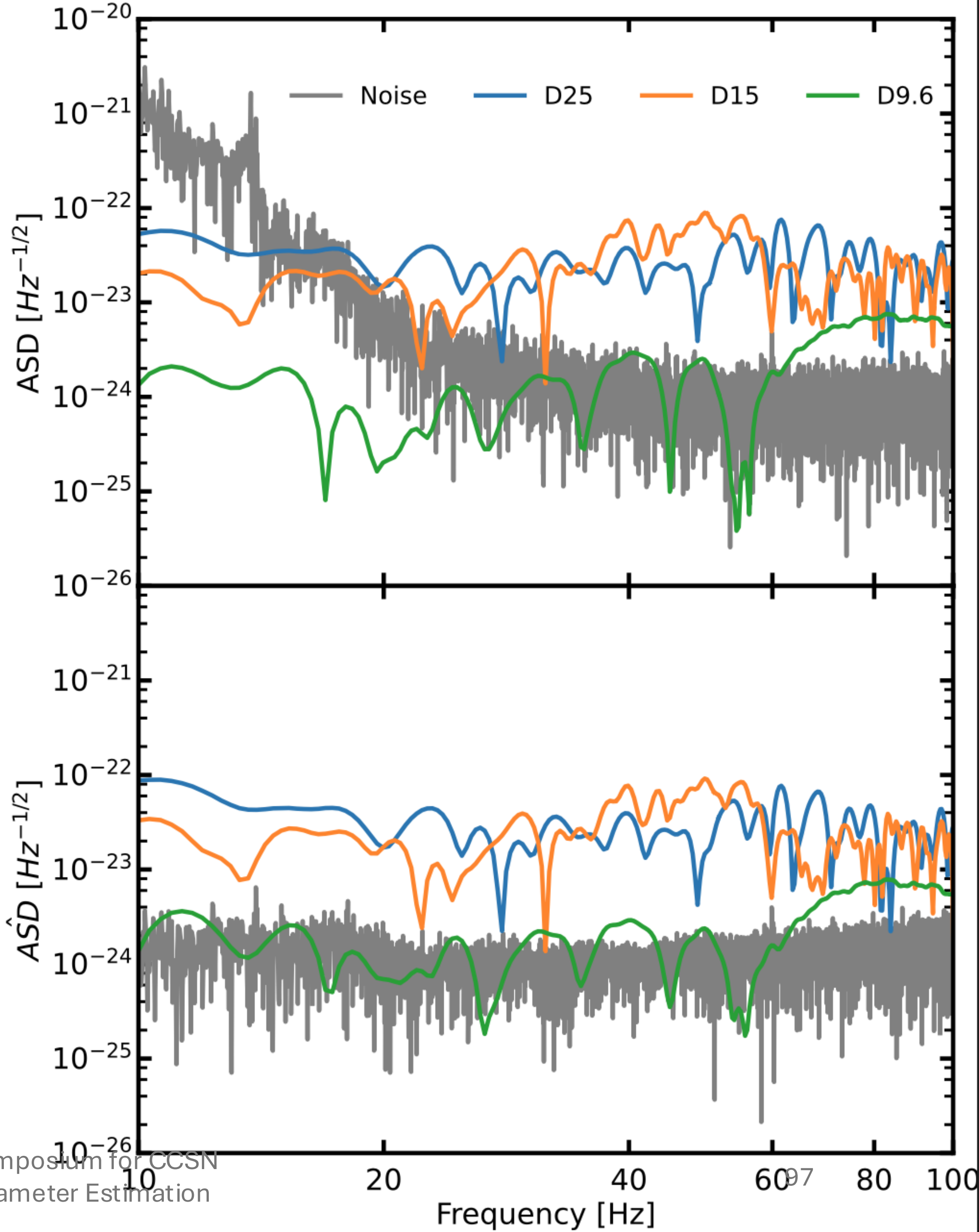

Detection

- We present the correlations for two different noise segments and two different distances.
- For 1 kpc, the D15 and D25 signals are always identifiable, and the D9.6 signal is only identifiable in one segment.
- For 10 kpc the D15 and D25 models are always identifiable (with a glitch present in the D15 case for one segment), and the D9.6 signal is unidentifiable.

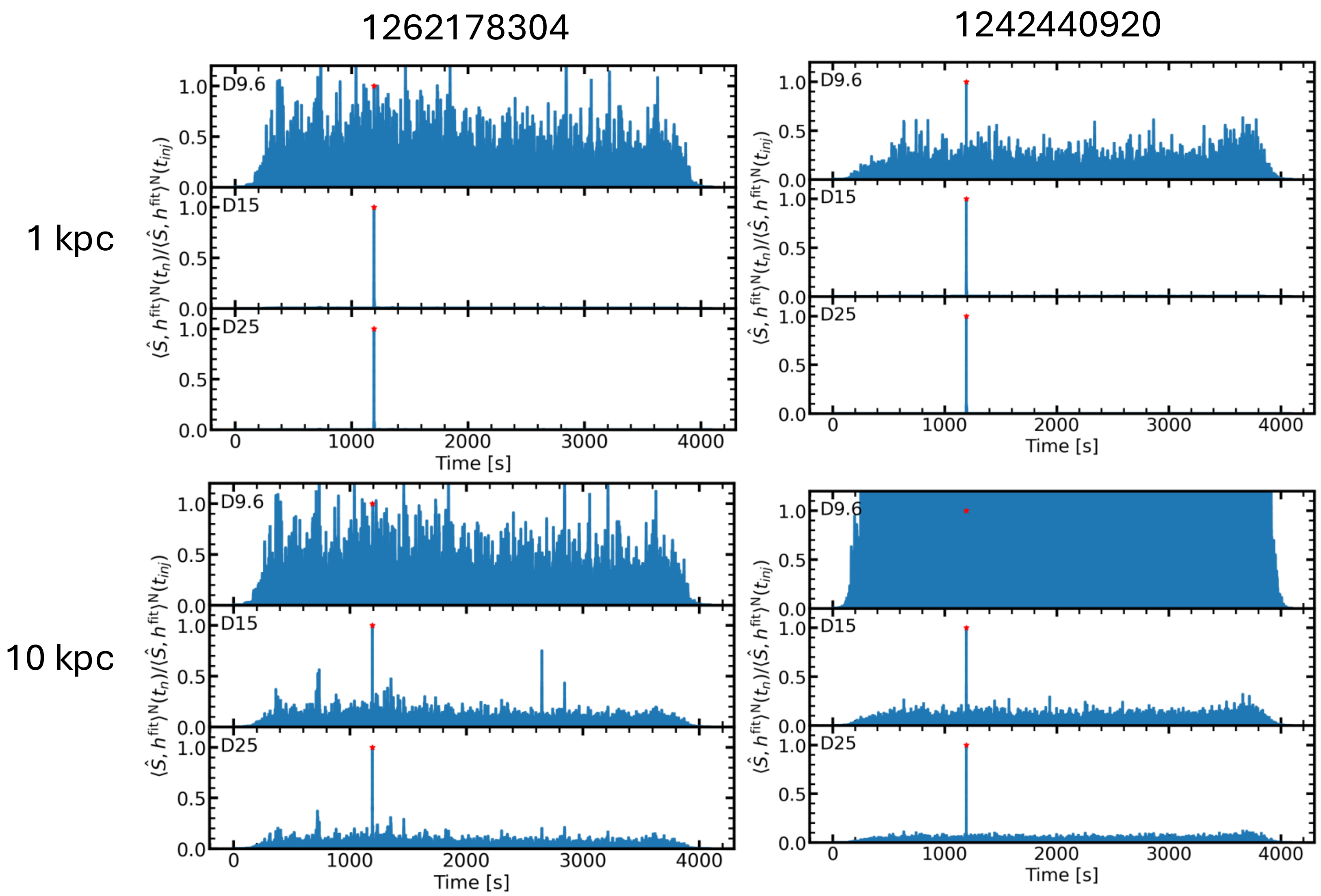

Detection Continued

- We also break our analysis into two seconds windows. To mimic a joint neutrino detection on-source-window.
- Here we see the False Alarm Probability for each of the noise segments.
- As 100 kpc is at the edge of our joint neutrino detection range and the edge of detectability in general for all models, we note the affect on detection of the noise around the signals injected time.

1262178304

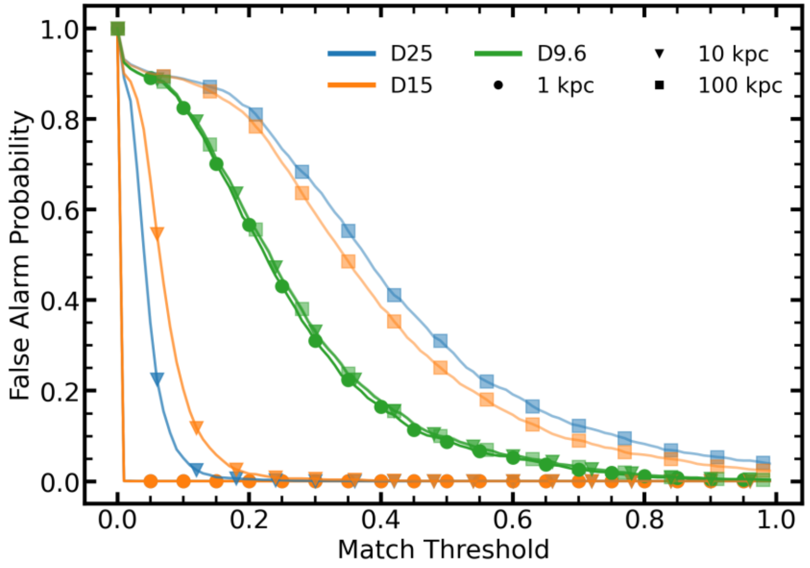

1242440920

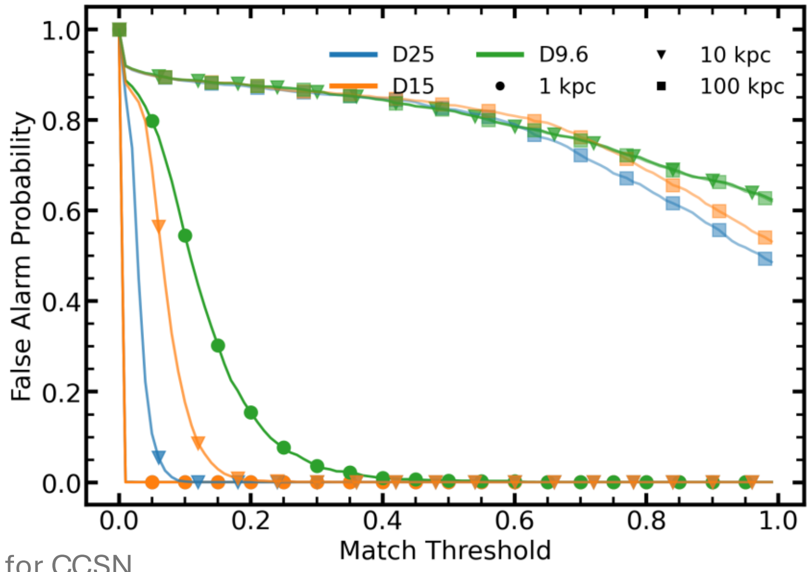

- Eimate and standard error of the coefficients of the best fit model describing the ratio r = M_{PNS}/R^2_{PNS} as function of the frequency of the $^2g_2$ mode.

Coefficient	Estimate	Standard error
β_1	2.00×10^{-06}	4.23×10^{-08}
β_2	-1.64×10^{-9}	9.99×10^{-11}
β_3	2.03×10^{-12}	5.41×10^{-14}
α_0	$-9.54 \times 10^{+00}$	6.80×10^{-02}
α_1	7.24×10^{-04}	1.56×10^{-04}
α_2	6.23×10^{-07}	8.15×10^{-08}

M. Obergaulinger, P. Cerdá-Durán, N. Christensen, J. A. Font, and R. Meyer (2021), Phys. Rev. D 103 (6), 10.1103/physrevd.103.063006.

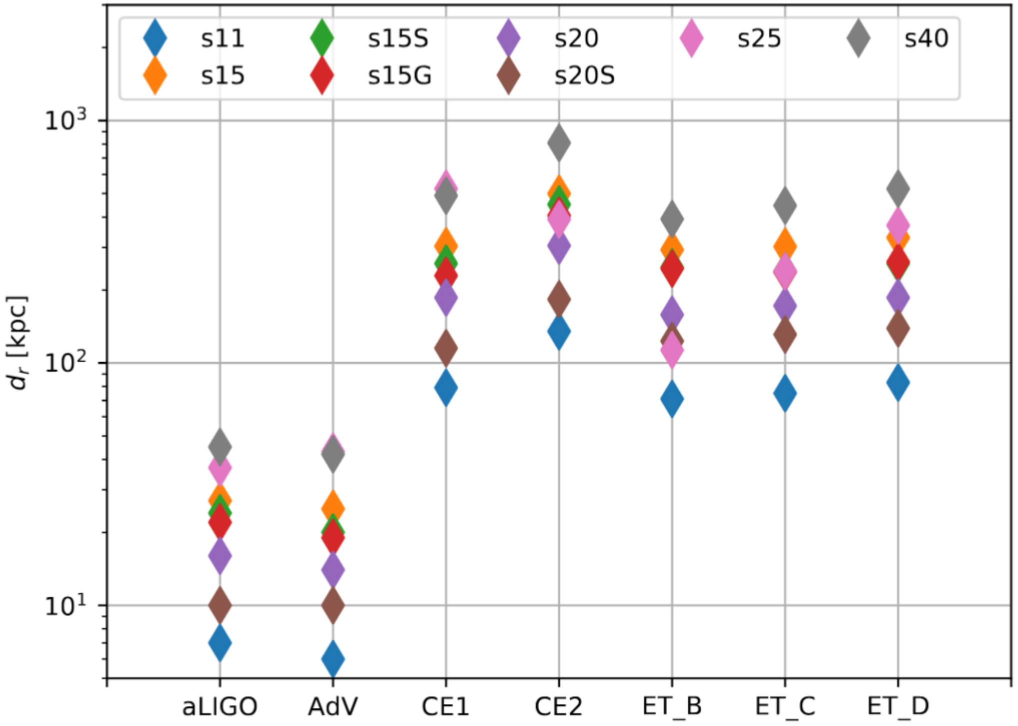

M. Obergaulinger, P. Cerdá-Durán, N. Christensen, J. A. Font, and R. Meyer (2021), Phys. Rev. D 103 (6), 10.1103/physrevd.103.063006.

		s11	s15	s15S	s15G	s20	s20S	s25	s40
aLIGO	d_r	7	28	24	22	16	11	38	46
	d_{det}	11	36	26	27	21	16	74	61
AdV	d_r	7	26	20	19	15	10	43	42
	d_{det}	10	32	22	23	18	13	64	52
CE1	d_r	79	304	258	229	187	115	524	490
	d_{det}	115	377	270	282	217	168	774	633
CE2	d_r	135	499	451	405	305	183	391	898
	d_{det}	197	649	468	489	375	294	1347	1100
ET_B	d_r	71	293	248	245	158	123	113	392
	d_{det}	106	364	274	391	216	200	805	665
ET_C	d_r	75	302	239	237	172	131	239	446
	d_{det}	97	332	246	260	194	164	727	603
ET_D	d_r	83	329	257	261	186	139	369	523
	d_{det}	107	368	271	285	213	174	796	661

Data: from Gaussian noise to real noise

Gaussian noise
(Previous work)

Previous set: 10^4 images for each value of Network SNR $\in$ [8,40]

Phys.Rev. D 98 (2018) 12, 122002

Real noise
(O2 – August 2017)

- **Training set – phenomenological waveforms:** 7 x 10^4 images for each distance $\in$ [0.2, 3] kpc and random sky localisation.
- **Blind set – phenomenological waveforms:** 26 x 10^4 images with distances chosen in a uniform distribution $\in$ [0.2, 15] kpc.
NOT involved in the training or validation procedure.
- **Test set - numerical simulations from the literature:** 6.5 x 10^4 images with distances $\in$ [0.1, 15] kpc

In particular, we chose a stretch of real data even containing glitches, taken during August 2017, when Virgo joined the run. The period includes about 15 days of coincidence time among the three detectors and we used this data set to generate about 2 years of time-shifts data to train and test the neural network as noise class.

Phys.Rev.D 103 (2021) 6, 063011

Previous work

Task: classification problem

Classes: 0 class (noise) and 1 class (event) with different level of noise (SNR)

Learning: curriculum learning

Data: Gaussian noise

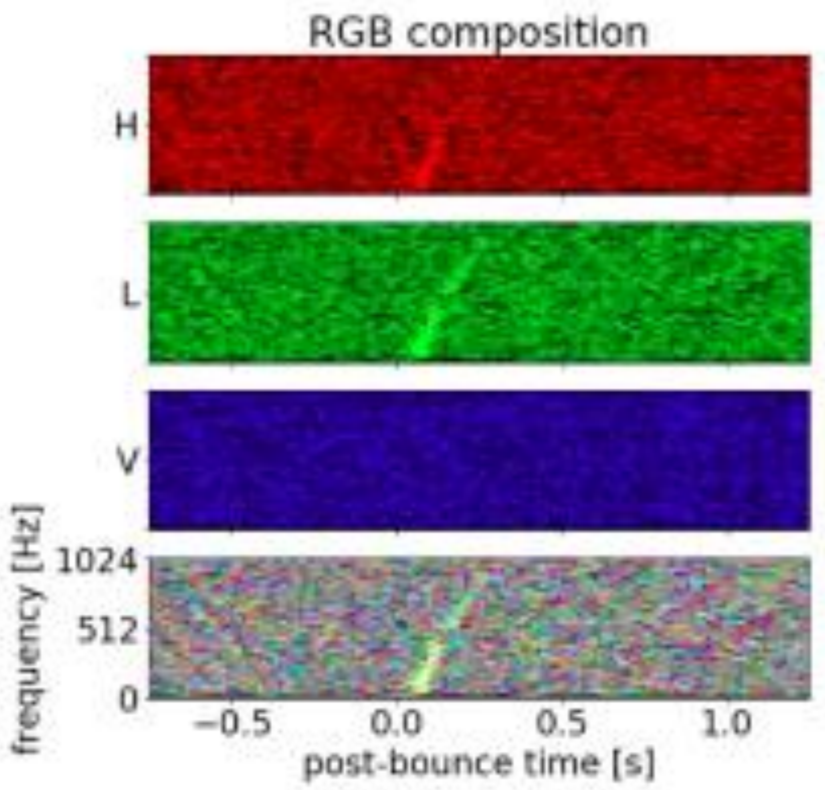

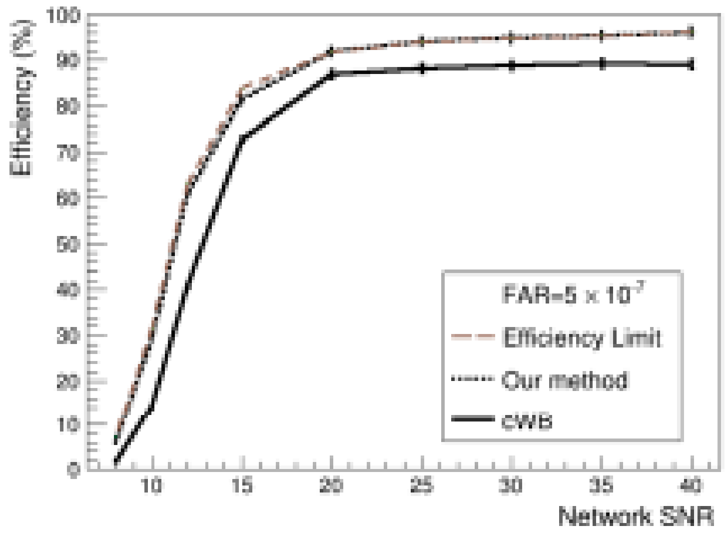

Figure 8: *Efficiency vs SNR in the case of complete cW[…] (continuous) and our method (dashed) for all SNRs. We re[…]port also the curve that shows the ratio between the inpu[…] events of the CNN and the total injected events in function o[…] SNR (brown). This curve sets the maximum efficiency tha[…] our method can achieve*

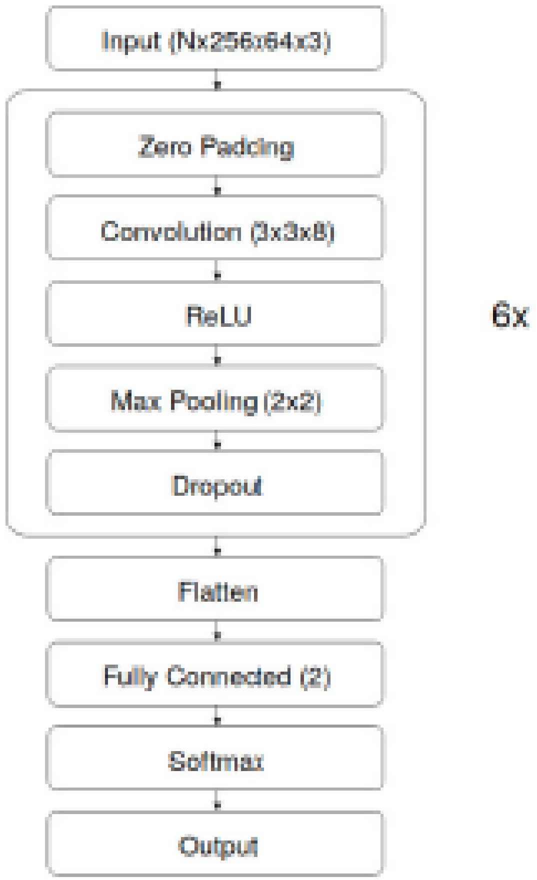

Figure 4: *Sketch of the architecture of our model.*

Phys.Rev. D 98 (2018) 12, 122002

Results in real detector noise

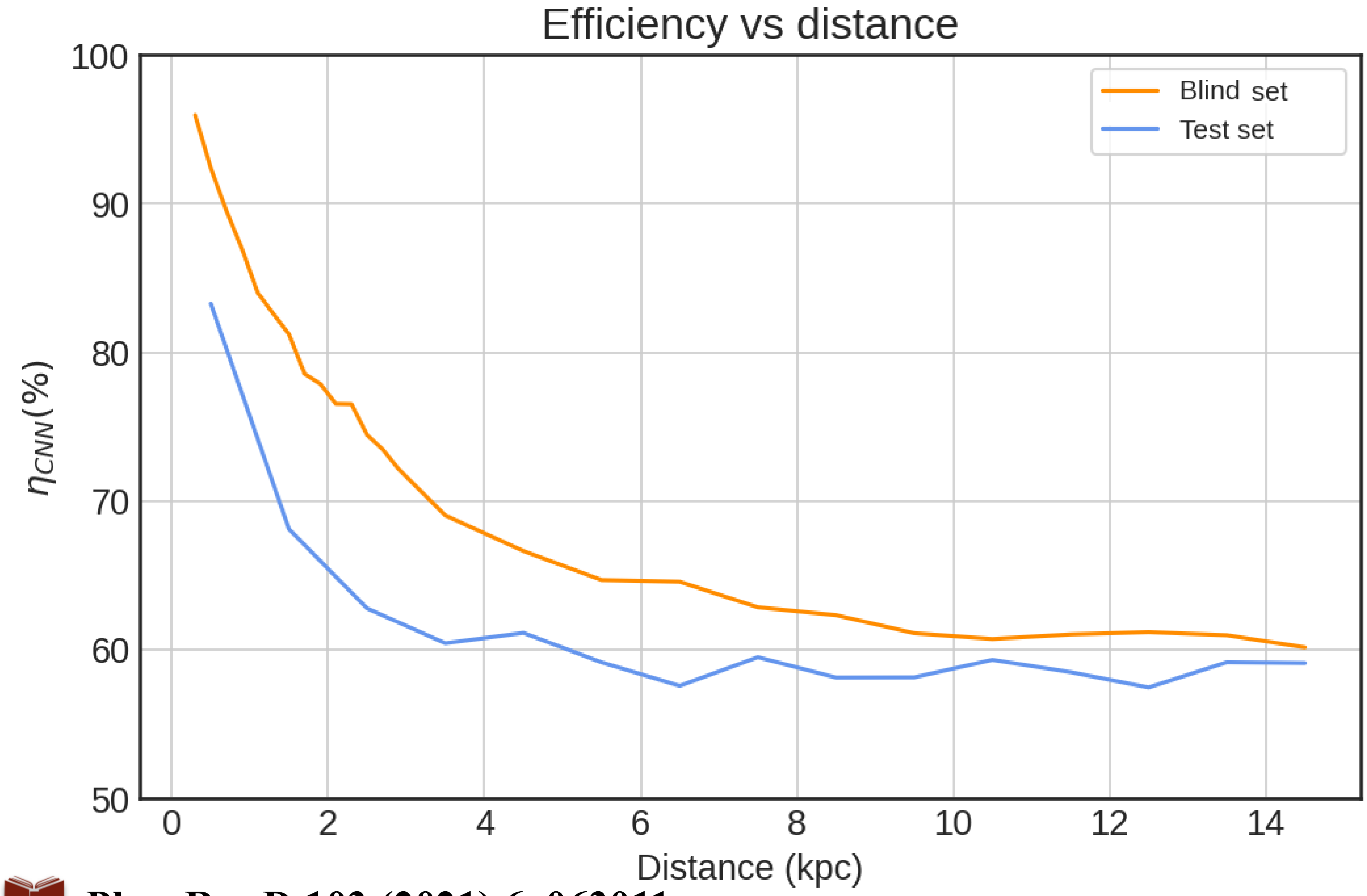

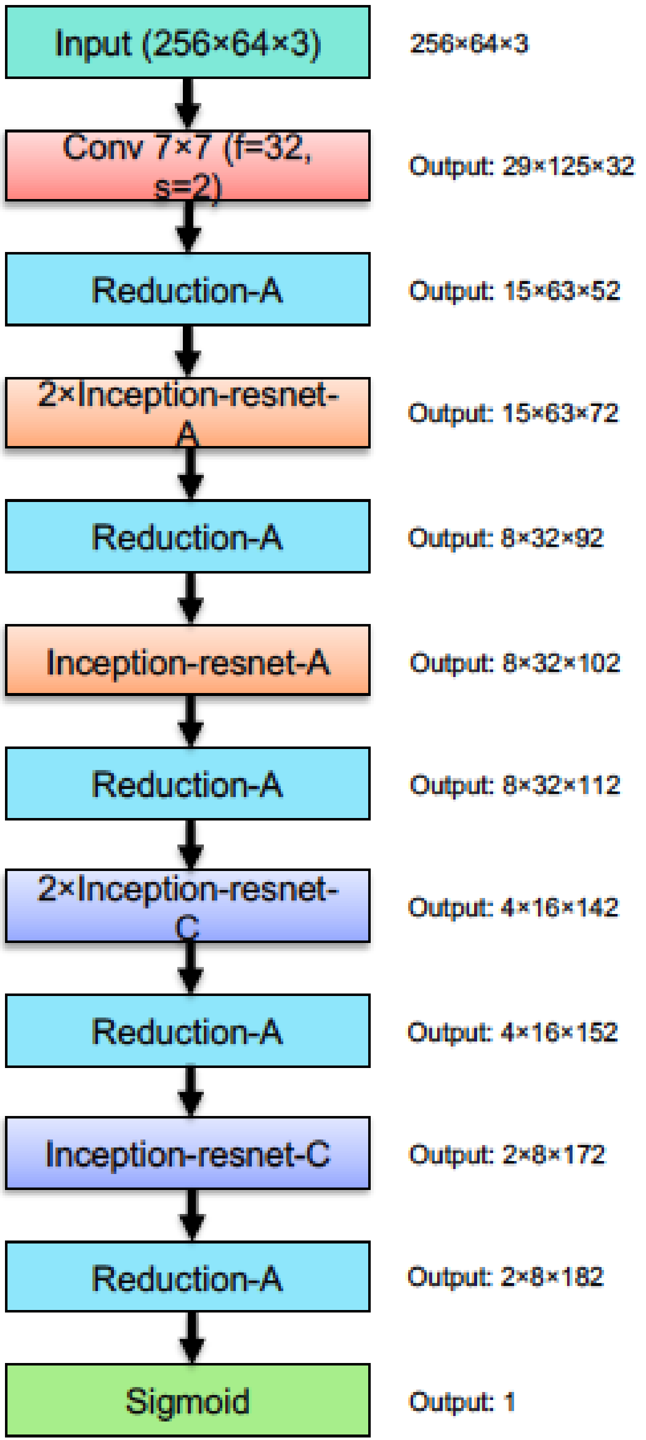

Phys.Rev.D 103 (2021) 6, 063011

Results, benchmark distance: 0.5 kpc, FAR=1/1y

No real GW data used. Considering simulated white noise based on O5 spectral sensitivity (*)

Efficiency: compatible among 5% difference

Using two SASI periods not performing better

- they do not align
- optimal direction for first SASI is not optimal for second SASI

(*) Living Rev Relativ 23, 3 (2020)

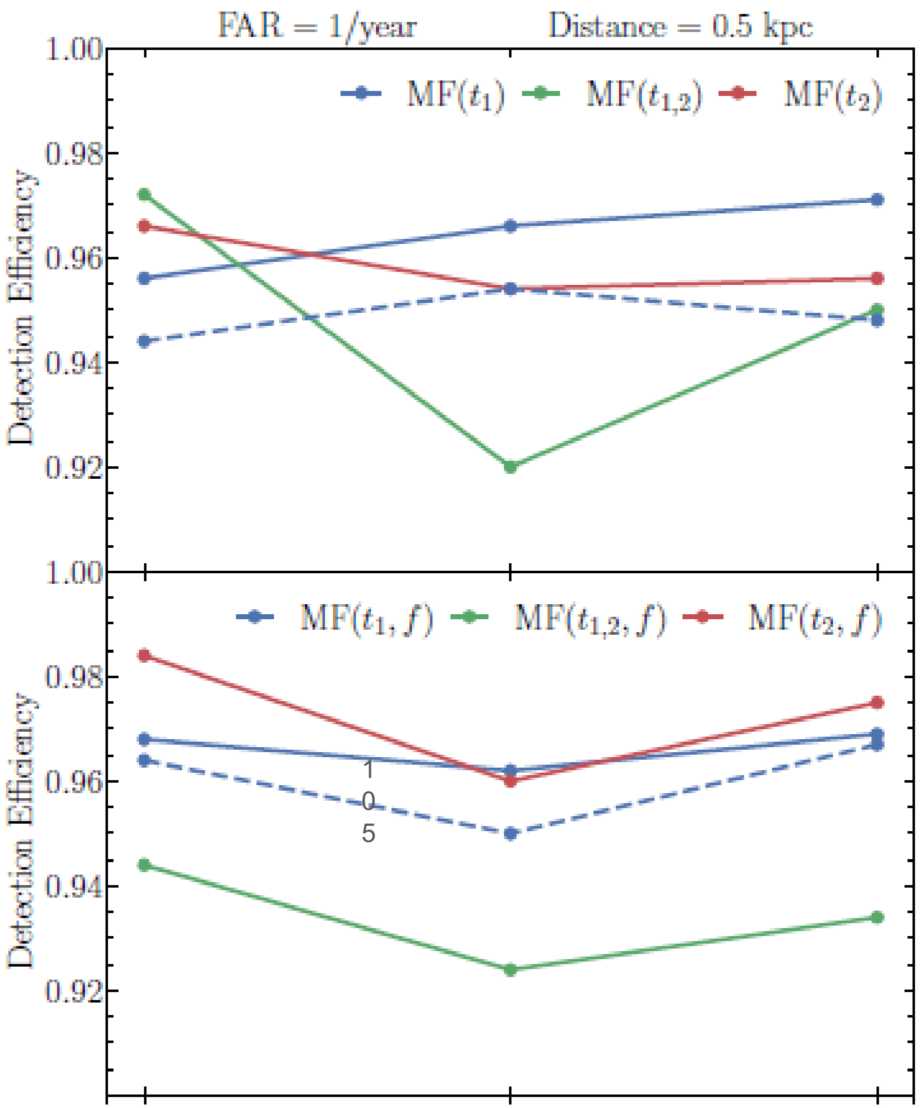

Phys. Rev. D 108, 103036, 2023

Detection Horizon

At low distance (<1.5 kpc) the matched-filter have better efficiency, but soon we arrive at high distance, EP performs better

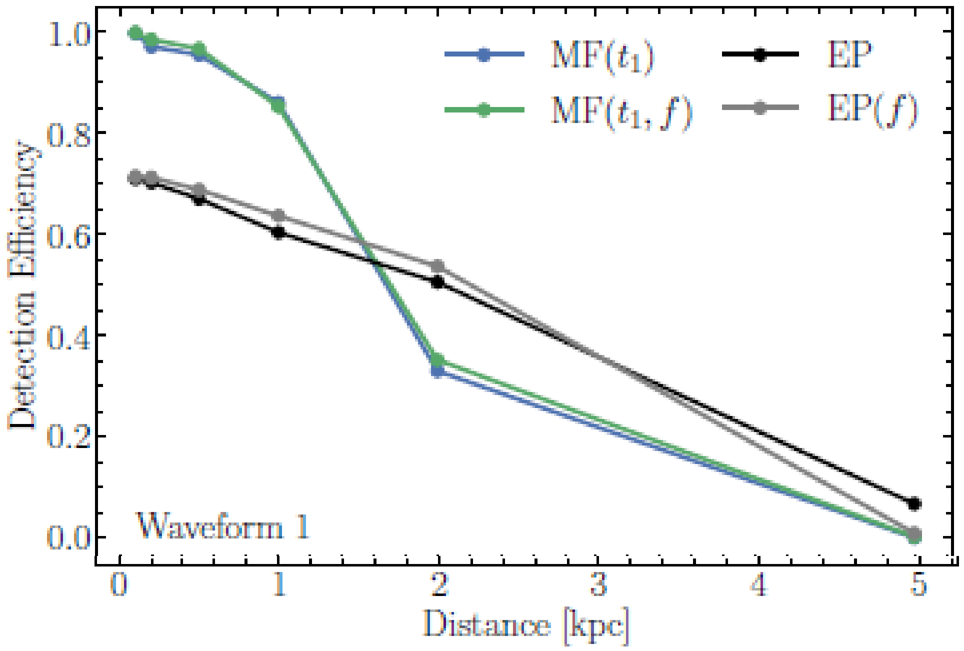

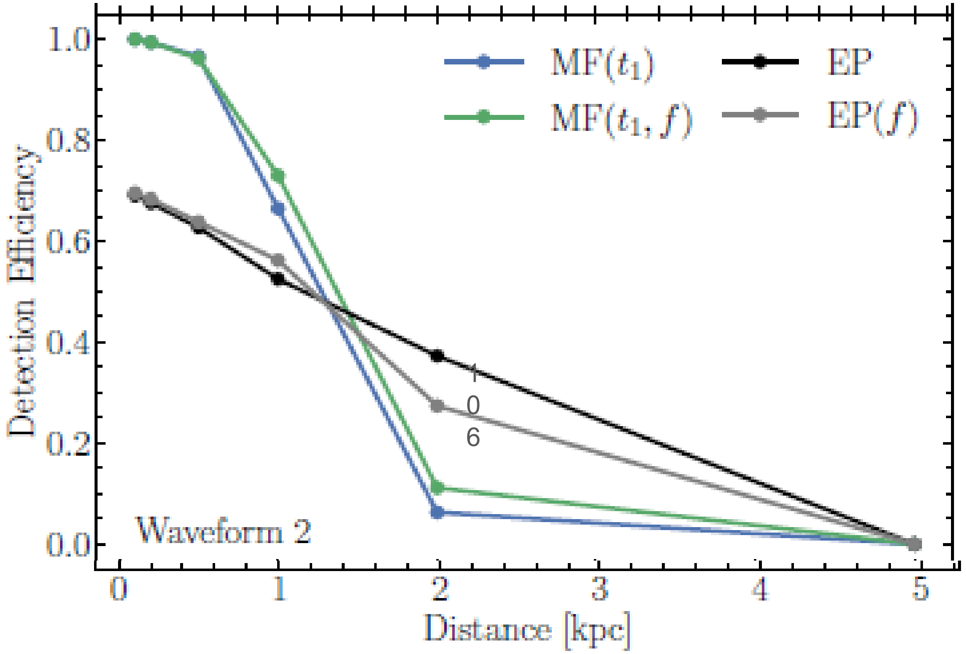

Phys. Rev. D 108, 103036, 2023